Development of flexible 3D printed strain sensors

Amirparsa Salehi

Thesis submitted to the University of Ottawa
in partial Fulfillment of the requirements for the Master of Applied Science degree in Chemical Engineering

Department of Chemical and Biological Engineering Faculty of engineering
University of Ottawa

Abstract

This thesis investigates the development of fully 3D-printed capacitive strain sensors fabricated from flexible, multi-walled carbon nanotube (MWCNT) reinforced hot-melt adhesive composites. These copolyester- and copolyamide-based filaments (5 wt.% and 10 wt.% MWCNT) enable the creation of compliant, conductive architectures not achievable with conventional carbon-filled polylactide materials. The research first examines how key parameters of fused deposition modeling (FDM), including layer height, raster orientation, printing speed, and nozzle temperature, influence electrical resistivity by altering interlayer fusion, filler alignment, and the continuity of percolated CNT networks. Results show that thicker layers and higher extrusion temperatures promote more stable conductive pathways, while orientation strongly dictates anisotropy in both copolyester and copolyamide systems.

Building on these findings, the dielectric response of the composites is characterized under dynamic shear and temperature-dependent conditions using broadband dielectric spectroscopy. Across 10^2–10^5 Hz, both formulations exhibit conduction-dominated behaviour, with loss permittivity exceeding storage permittivity by two to three orders of magnitude. Mechanical deformation reduces permittivity by disrupting MWCNT–MWCNT contacts, and temperature elevation from 125 °C to 200 °C produces a pronounced increase in permittivity attributable to thermally activated charge transport. Classical dipolar relaxation models do not accurately reproduce the measured spectra, indicating that conduction and interfacial processes dominate relaxation behaviour.

Finally, a single step, multi-material capacitive strain sensor was designed and fabricated using co-printed MWCNT electrodes embedded within a flexible non-conductive sensor body. The hexagonal geometry provides stable deformation paths while simplifying electrode separation. A resonance-based readout system built around a commercially available evaluation module enables high-resolution capacitance tracking, supported by a Python acquisition framework for real-time filtering, drift correction, and visualization.

Résumé

Cette thèse étudie le développement de capteurs de déformation capacitifs entièrement imprimés en 3D, fabriqués à partir de composites adhésifs thermofusibles flexibles renforcés par des nanotubes de carbone multiparois (MWCNT). Ces filaments à base de copolyester et de copolyamide (5 % et 10 % en masse de MWCNT) permettent la création d'architectures conductrices et conformables impossibles à obtenir avec les matériaux conventionnels de type polylactide chargé en carbone.

La recherche examine d'abord comment les paramètres clés du procédé de dépôt de filament fondu (FDM), notamment la hauteur de couche, l'orientation des chemins d'impression, la vitesse d'impression et la température de la buse, influencent la résistivité électrique en modifiant la fusion inter-couche, l'alignement des charges et la continuité des réseaux percolés de MWCNT. Les résultats montrent que des couches plus épaisses et des températures d'extrusion plus élevées favorisent des chemins conducteurs plus stables, tandis que l'orientation impose une anisotropie marquée dans les systèmes à base de copolyester comme de copolyamide.

À partir de ces observations, la réponse diélectrique des composites est caractérisée sous cisaillement dynamique et en fonction de la température à l'aide d'une spectroscopie diélectrique large bande. Sur la plage 10^2–10^5 Hz, les deux formulations présentent un comportement dominé par la conduction, avec une permittivité de perte supérieure à la permittivité de stockage de deux à trois ordres de grandeur. La déformation mécanique réduit la permittivité en perturbant les contacts entre MWCNT, tandis qu'une élévation de température de 125 °C à 200 °C entraîne une augmentation marquée de la permittivité due à l'activation thermique du transport de charge. Les modèles classiques de relaxation dipolaire ne reproduisent pas correctement les spectres mesurés, indiquant que la conduction et les processus interfacials dominent le comportement de relaxation.

Enfin, un capteur capacitif de déformation, imprimé en une seule étape et en matériau multimatière, a été conçu et fabriqué en co-imprimant des électrodes MWCNT intégrées dans un corps de capteur flexible et non conducteur. La géométrie hexagonale offre des trajectoires de déformation stables tout en simplifiant la séparation des électrodes. Un système de lecture basé

sur la résonance, construit autour d'un module d'évaluation commercial, permet un suivi haute résolution de la capacitance, soutenu par une plateforme d'acquisition Python assurant le filtrage en temps réel, la correction de dérive et la visualisation.

Acknowledgements

I would first like to thank my supervisor, Prof. Andrew Anstey, whose support and guidance made this project possible. I am deeply grateful for the freedom he gave me to pursue the directions that inspired me, and for his patience and encouragement during the more challenging periods of this work.

I would also like to express my sincere gratitude to Prof. Paulina Latko-Durałek for developing the conductive materials used in this research and for her invaluable collaboration throughout the project. Her preparation and provision of all conductive filaments were essential to the success of this work. I would also like to acknowledge Prof. Natalie Baddour for initiating the smart sensing research and providing the motivation and conceptual framework for this project, which was supported through an NSERC Alliance grant under her leadership.

I am grateful to my lab mates, Claire and Kayla, for their help, support, and collaboration throughout this project.

To Amirom, Bardia, Amirsajjad, and Ali-thank you for all your support; you are more than friends to me. And to Saeed, thank you for being my best friend and a great roommate, and for pushing me forward during difficult times.

I would also like to thank my father, Majid, and my brother, Amirreza, for their constant support in every stage of this journey.

Finally, I wish to dedicate this work to my mother, Mitra, whose memory continues to guide and inspire me. Although she is no longer here, her love and strength have carried me through every step of this journey. Love you, Mom.

Thank you to my thesis committee for your consideration of this report.

Table of contents

Résumé iii

List of figures viii

List of abbreviations x

Greek symbols xii

Chapter 1 – Introduction 1

1.1 Background and motivation 1

1.2 Problem statement 2

1.3 Objectives of the research 2

1.4 Scope of the thesis 3

Chapter 2 - Literature review 6

2.1 Introduction 6

2.2 Fused deposition modeling (FDM) and fused filament fabrication (FFF): Principles, history, and technical insights 7

2.3 Structural design and geometrical structures 10

2.4 Effect of printing parameters on the conductivity of 3D printed conductive composites 14

2.4.1 Layer height 15

2.4.2 Orientation angle (infill angle) 16

2.4.3 Printing nozzle temperature 17

2.4.4 Infill density 19

2.4.5 Post-print annealing 19

2.4.6 Printing speed 20

2.4.7 Nozzle diameter 21

2.5 Dispersion, percolation, and conductivity mechanism 21

2.6 Conductive fillers in composite resins 24

2.6.1 Carbon black 24

2.6.2 Carbon nanotubes 26

2.6.3 Carbon fibers 28

2.7 Current state of the art in 3D printing of conductive filaments 29

2.8 Capacitive sensing 33

2.8.1 Capacitance measurements - time domain measurement 36

2.8.2 Capacitance measurements – resonance/frequency-based measurement 38

2.9 Dielectric relaxation 40

Chapter 3: Investigating the effect of printing parameters on conductivity 46

3.1 Introduction **46**

3.2. Materials and methods **47**

3.3 Results and discussion **52**

3.3.1 Effect of layer height on electrical resistivity 52

3.3.2 Effect of print orientation on electrical resistivity 54

3.3.3 Effect of printing speed on electrical resistivity 55

3.3.4 Effect of nozzle temperature on electrical resistivity 58

Chapter 4: Dielectric behaviour under dynamic shear **61**

4.1 Introduction **61**

4.2 Materials and methods **62**

4.3 Results and discussion **63**

4.3.1 Coupled oscillation and dielectric spectroscopy 63

4.3.2 Dielectric spectroscopic analysis of temperature dependency 70

4.4 Modeling of dielectric relaxation **72**

4.5 Chapter summary and key findings **73**

Chapter 5: Prototyping of flexible strain sensors **75**

5.1 Introduction **75**

5.2 Sensor design and fabrication **75**

5.3 Readout hardware and measurement strategy **77**

5.4 Software architecture and code-level description **79**

5.5 Real-time visualisation **85**

5.6 Limitations and practical constraints **87**

Chapter 6 – Conclusion and future work **89**

6.1 Conclusion **89**

6.2 Future work **90**

References **92**

List of figures

Figure 1: FDM schematic structure 8
Figure 2: (A) Schematic of a bath configuration SLA printer with a direct write curing process. (B)Schematic of a layer configuration SLA printer with a projection-based curing method [20].. 9
Figure 3: Common 2D geometries for printed strain sensors: straight, serpentine, horseshoe, grid, and auxetic patterns.....11
Figure 4: Simulation of mechanical properties of the serpentine-shaped substrate [23]. 12
Figure 5: (a) Fabrication process of the auxetic structure sensor; (b) Section view of the barrel for printing the auxetic structure [24]. 13
Figure 6: Schematic illustration of the electrical conductivity (percolation) behavior of a composite as a function of conductive nanoparticle concentration. 22
Figure 7: Effect of styrene-ethylene/butane-styrene (SEBS) content on the (b) tensile properties (strength and elongation at break) and (c) electrical conductivity of CB/styrene-ethylene/butane-styrene (SEBS)/polystyrene (PS)/polypropylene (PP) composites [42]. 25
Figure 8: (a) Effect of CB content on the conductivity of the composites at 1 kHz (b) Linear fit of conductivity of the composites [43]. 26
Figure 9: The influences of (a) CNT loading contents and (b) melt mixing sequences on the electrical responsiveness property of the composites [46]. 28
Figure 10: Schematic of RC Circuit..... 36
Figure 11: Schematic of LC circuit. 40
Figure 12: 3D printing infill orientation angle..... 47
Figure 13: Flow chart of filament manufacturing process from copolyester adhesive, and MWCNT 49
Figure 14: Two-probe and four-probe method for calculating resistivity. 50
Figure 15: ASTM D638 type IV specimen. 51
Figure 16: Four-probe connection on printed sample. 51
Figure 17: Effect of layer height on electrical resistivity of 3D-printed G2A_10 (copolyamide, 10 wt.% MWCNT) at two nozzle temperatures (200°C, 230°C) and three raster orientations (0°, 45°, 90°). 52
Figure 18: Electrical resistivity of 3D printed ABR as a function of layer height at 230 °C for three raster orientations (0°, 45°, and 90°)..... 53
Figure 19: Effect of print orientation on the electrical resistivity of 3D-printed copolyester/MWCNT samples..... 55
Figure 20: Effect of printing (infill) speed on electrical resistivity of 3D printed G2A_10. 56
Figure 21: Effect of printing (infill) speed on electrical resistivity of 3D printed ABR. 57
Figure 22: Effect of nozzle temperature on electrical resistivity of 3D printed ABR. 58
Figure 23: Effect of nozzle temperature on electrical resistivity of 3D printed G2A_10. 59
Figure 24: (a) Storage permittivity vs. frequency and (b) loss permittivity vs. frequency of copolyester 5% MWCNT at 150°C under varying shear strain at 1 rad/s as oscillation frequency 63

Figure 25: Storage permittivity, and loss permittivity vs frequency of copolyester 10% MWCNT at $150°C$ 67
Figure 26: Storage and loss permittivity of the copolyester composite containing 5 wt.% MWCNT under 10% (left), 50% (middle), and 100% (right) strain amplitude, comparing dielectric response at 10 rad/s and 30 rad/s dynamic shear rate. 69
Figure 27: Storage and loss permittivity of the copolyester composite containing 5 wt.% MWCNT under 10% (left), 50% (middle), and 100% (right) strain amplitude, comparing dielectric response at 10 rad/s and 30 rad/s dynamic shear rate. 69
Figure 28: Storage and loss permittivity of copolyester 5 wt.% MWCNT at different temperatures 71
Figure 29: Cole-Cole fitting of storage and loss permittivity at $175°C$ for ABR 73
Figure 30: 3D modeling of hexagonal sensor design 76
Figure 31: 3D modeling of hexagonal with square extension sensor design 76
Figure 32: FDC2214 Evaluation module (EVM) 78
Figure 33: Schematic of sensor setup. 79
Figure 34: Demonstration of sensor performance (left) undeformed sensor, (right) deformed sensor. 86

List of abbreviations

ABS – Acrylonitrile Butadiene Styrene

AM – Additive Manufacturing

ANOVA – Analysis of Variance

ASTM – American Society for Testing and Materials

AWG – American Wire Gauge

CAM – Computer-Aided Manufacturing

CB – Carbon Black

CF – Carbon Fibers

CH – Channel

CNT – Carbon Nanotube

CRC – Cyclic Redundancy Check

DC – Direct Current

DIW – Direct Ink Writing

DMA – Dynamic Mechanical Analysis

DSC – Differential Scanning Calorimetry

EMI – Electromagnetic Interference

ESR – Equivalent Series Resistance

ETPU – Electrically Conductive Thermoplastic Polyurethane

EVM – Evaluation Module

FCO – Forced Convection Oven

FDM – Fused Deposition Modeling

FEA – Finite Element Analysis

FFF – Fused Filament Fabrication

GE – Graphene

GF – Gauge Factor

GNP – Graphene Nanoplatelets

GNS – Graphene Nanosheets

GUI – Graphical User Interface

HDF5 – Hierarchical Data Format version 5

HMA – Hot-Melt Adhesive

Hz – Hertz (unit of frequency)

IC – Integrated Circuit

I²C – Inter-Integrated Circuit (communication protocol)

L – Inductance

LC – Inductor-Capacitor (resonant circuit)

LCR – Inductance-Capacitance-Resistance (meter)

LDPE – Low-Density Polyethylene

MMU – Multi-Material Unit (Prusa printer accessory)

MWCNT – Multi-Walled Carbon Nanotube

MWS – Maxwell-Wagner-Sillars (polarization mechanism)

Ni-Cr – Nickel-Chromium (wire alloy)

PCB – Printed Circuit Board

PEEK – Polyether Ether Ketone

PLA – Polylactic Acid

PP – Polypropylene

PS – Polystyrene

RC – Resistor-Capacitor (circuit)

SD – Standard Deviation

SEBS – Styrene-Ethylene/Butane-Styrene (copolymer)

SEM – Scanning Electron Microscopy

SI – International System of Units (Système International)

SLA – Stereolithography (3D printing method)

SLS – Selective Laser Sintering

SWCNT – Single-Walled Carbon Nanotube

TGA – Thermogravimetric Analysis

TPI – Thermoplastic Polyimide

TPE – Thermoplastic Elastomer

TPS – Thermoplastic Starch

TPU – Thermoplastic Polyurethane

USB – Universal Serial Bus

UV – Ultraviolet

Wt.% – Weight Percent

Greek symbols

α – Cole-Cole broadening parameter; absorption coefficient

β – Cole-Cole asymmetry parameter

ε – Permittivity (dielectric constant)

ε_0 – Vacuum permittivity (8.854×10^{-12} F/m)

ε' – Storage permittivity (real component)

ε'' – Loss permittivity (imaginary component)

ε_r – Relative permittivity

ε_s – Static (low-frequency) permittivity

ε_∞ – High-frequency permittivity

ρ – Electrical resistivity

σ – Electrical conductivity

τ – Relaxation time

φ – Volume fraction; phase angle

φ_c – Percolation threshold (critical volume fraction)

ω – Angular frequency (rad/s), where $\omega = 2\pi f$

Chapter 1 – Introduction

1.1 Background and motivation

Flexible strain sensors have become essential in wearable monitoring, soft robotics, human motion capture, and interaction technologies that require sensing elements capable of stretching, bending, and conforming to non-rigid surfaces. Traditional fabrication approaches, including coating, casting, and multi-step lamination, restrict geometric freedom and introduce reliability limitations due to manual assembly and material incompatibilities. These constraints have led to increasing interest in additive manufacturing as a means to produce mechanically compliant sensors with integrated functionality.

A fundamental bottleneck in this area is the limited availability of flexible and electrically conductive filaments that are both electrically conductive and suitable for fused deposition modeling. Most commercially available conductive materials rely on polylactic acid (PLA) filled with conductive particles including carbon black, graphene, or metal powders, and are consistently reported to exhibit brittleness, cracking, and failure under even moderate deformation [1]. Though it has excellent mechanical strength and stiffness, PLA is an inherently brittle resin, and its toughness is generally further decreased with the addition of conductive particles [1], [2]. This prevents their use in applications that require elastic, wearable, or high-compliance sensing.

In contrast, the conductive filaments used in this research were developed by Misiak et al.[3] and represent a new class of printable multi-walled carbon nanotube (MWCNT) modified hot-melt adhesive composites. These filaments combine the elasticity of copolyester or copolyamide adhesives with dense percolated nanotube networks, achieving conductivity levels rarely obtained in flexible FDM feedstocks. Through collaboration with Prof. Paulina Latko-Durałek at the Warsaw University of Technology, we proposed investigating the use of these filaments as a means to produce highly flexible 3D-printed capacitive strain sensors. These sensors would be produced in a single manufacturing step using multi-material FDM, an approach that is not feasible with conventional commercial materials. This combination of technological need, material opportunity, and manufacturing capability motivates the present research.

1.2 Problem statement

Despite increasing demand for flexible strain sensors driven by wearable health monitoring, soft robotics, electronic skin, and human machine interfaces, current technologies still face significant challenges in both performance and manufacturability. Recent reviews consistently emphasize that flexible, stretchable strain sensors are essential for next generation wearable and body conformable electronics, with applications in motion tracking, rehabilitation, intelligent robotics, and AI-assisted human machine systems [4], [5], [6]. However, many existing devices rely on multistep fabrication routes such as sequential coating, patterning, and assembly, which increase cost and complexity and make large-scale production difficult [7], [8]. These limitations have led to growing interest in additive manufacturing and other direct-write approaches as routes to integrate the sensing element and mechanical support in a single structure [9], [10]. A key element in additive manufacturing of these devices is the use of conductive, flexible filaments. MWCNT-based composites are one of the main contributors in this field. Electrical performance in MWCNT-based composites is highly sensitive to printing parameters such as temperature, layer height, orientation, and infill density, yet systematic understanding of these effects remains incomplete. Most studies focus on resistive transduction, which suffers from drift, hysteresis, and poor repeatability in soft materials [11], [12]. Capacitive sensing offers greater stability [13], but research on fully printed capacitive devices is scarce, and designs often depend on manual assembly or multi-stage construction.

There is therefore a clear need to:

1. Understand how printing conditions affect conductive nanocomposite behaviour,
2. Analyse the dielectric mechanisms that govern their response, and
3. Develop a reliable, single-step printed capacitive strain sensor using flexible MWCNT-based filaments, with a robust method for reliably processing the signal coming from the sensor.

1.3 Objectives of the research

The primary objective of this research is to understand how additive-manufacturing conditions shape the electrical and dielectric behaviour of MWCNT polymer nanocomposites and to use those

insights to realize a fully printed capacitive strain sensor. First, the study examines the influence of key FDM parameters, such as layer height, print orientation, infill pattern, print speed, and extrusion temperature, on the conductivity and network formation of MWCNT-filled filaments. Building on this, the work investigates the dielectric response of the same composites under varying frequency, temperature, and mechanical loading, with the aim of identifying the dominant polarization and conduction processes. A further objective is the design and fabrication of a single-step, multi-material capacitive sensor in which conductive and insulating regions are produced within one continuous print. To support real-time measurement, a resonance-based readout system is implemented using a commercially available evaluation module from Texas Instruments. Finally, the sensor is evaluated under mechanical deformation, focusing on its sensitivity, stability, drift characteristics, and noise behaviour.

1.4 Scope of the thesis

This thesis is centered on the investigation, characterization, and application of flexible multi-walled carbon nanotube (MWCNT) reinforced hot-melt adhesive (HMA) copolyester and copolyamide filaments developed by our research collaborators. The primary goal is to determine whether these filaments can support single step multi-material fabrication of capacitive strain sensors using fused deposition modeling (FDM). The study examines three specific formulations: ABR (copolyester 5 wt.% MWCNT), G1839_10 (copolyester 10 wt.% MWCNT), and G2A_10 (copolyamide 10 wt.% MWCNT), evaluating their electrical, dielectric, and deformation-dependent behaviors under various printing and testing conditions. The scope is restricted to laboratory-scale prototyping, benchtop dielectric spectroscopy, and manually induced strain responses; it does not include large-scale manufacturing, long-term durability analyses, or industrial reliability testing.

Chapter 2 provides a comprehensive review of the scientific and technological context for this work. It surveys existing flexible strain sensing technologies, including resistive, capacitive, piezoelectric, and optical methods, and evaluates their respective advantages and limitations for deformation sensitive applications such as wearable monitoring, soft robotics, and human machine interfaces. The chapter places particular emphasis on the challenges of resistive transduction, specifically drift, hysteresis, and instability in soft polymer systems, while highlighting the

increasing interest in capacitive devices due to their superior repeatability and lower intrinsic drift. It also reviews relevant literature on carbon-based polymer nanocomposites, focusing on conductive network formation, percolation mechanisms, and how filler concentration impacts electrical properties. Additive manufacturing approaches for functional materials are discussed, emphasizing benefits such as geometric flexibility, system integration, and rapid fabrication. Previous research on printed conductive filaments and flexible electronics is examined to illustrate the limitations of multistep or manual sensor assembly. The chapter concludes with an in-depth overview of dielectric phenomena in MWCNT composites, including storage and loss permittivity.

Chapter 3 focuses on understanding how printing parameters affect the electrical properties of the MWCNT-based filaments. The influence of nozzle temperature, layer height, infill density, raster orientation (orientation angle), and printing speed is systematically investigated to determine their impact on conductivity (resistivity), and MWCNT network continuity. The chapter examines how these processing variables modify interlayer contact quality, conductive path formation, and overall resistivity. The second part of chapter 3 analyzes the underlying causes of the observed electrical behavior, with emphasis on MWCNT dispersion.

Chapter 4 examines the dielectric behavior of the composites using temperature dependent dielectric spectroscopy performed on ARES G2 rotational rheometer (TA Instruments) coupled to an E4980LA LCR meter (Keysight Technologies). Storage and loss permittivity, conductivity contributions, and relaxation behavior are investigated across frequencies and temperatures relevant to polymer relaxations. The chapter quantifies how MWCNT concentration and thermal activation influence polarization and conduction pathways. Special attention is paid to the transition from interfacial polarization-dominated responses to conduction-dominated behavior as frequency decreases. This chapter also explores the effect of continuous oscillation on dielectric response of the material across a wide range of shear strain and oscillation frequency.

Chapter 5 describes the design, fabrication, and characterization of the fully 3D-printed, single-step multi-material capacitive strain sensor. It details the geometric rationale behind the hexagonal structure, the co-printing of conductive and insulating filaments, and the challenges of ensuring robust interfacial adhesion between materials. The chapter further outlines the resonance-based readout system using the FDC2214EVM evaluation module, including hardware setup,

signal-processing strategy, calibration methods, and the Python-based data acquisition and visualization pipeline. This final chapter integrates the outcomes of earlier chapters to demonstrate the feasibility and performance of the monolithic printed sensor.

Chapter 2 - Literature review

2.1 Introduction

Flexible strain sensors have become an important class of devices in wearable systems, soft robotics, biomedical monitoring, and human motion analysis. Their widespread use arises from the need to measure deformation on surfaces that bend, twist, or stretch, which conventional rigid sensors cannot accommodate. As applications increasingly require lightweight, conformable, and safe interfaces with the human body or deformable structures, materials and fabrication strategies that enable mechanical compliance and reliable signal transduction have gained significant attention across the literature.

Additive manufacturing, particularly fused deposition modeling, has emerged as a promising approach for producing flexible sensing elements with tailored geometries and functions. Unlike traditional fabrication routes that depend on coating, casting, or multi step assembly, 3D printing enables direct patterning of conductive and insulating regions within a single build. This capability allows researchers to create geometries that enhance sensitivity, durability, and stretchability, including serpentine paths, auxetic lattices, multilayer structures, and embedded conductive channels. The development of nanocomposite filaments containing conductive fillers such as carbon nanotubes further expands this field, providing printable materials with tunable electrical and mechanical properties suitable for strain transduction.

Various sensing mechanisms have been explored for flexible strain detection, with resistive and capacitive approaches being the most widely reported in the literature [14], [15]. Resistive sensors rely on changes in electrical resistance caused by deformation of a conductive network, where stretching alters distances between conductive particles or disrupts percolated pathways. While straightforward to implement, resistive sensors often exhibit drift, hysteresis, and reduced repeatability under large deformation. Capacitive sensors, in contrast, operate by measuring changes in capacitance resulting from variations in electrode spacing, overlap area. Their performance is less dependent on maintaining continuous conductive pathways, offering improved stability and long-term reproducibility. As a result, capacitive architectures have gained growing interest for applications requiring reliable and consistent output under repeated loading.

Together, these developments form the scientific foundation for the literature reviewed in this chapter. Advances in flexible materials, 3D printing, and nanocomposite design continue to shape

the capabilities of strain sensors, while the choice of sensing mechanism, device structure, and material formulation remains central to ongoing research in this field.

2.2 Fused deposition modeling (FDM) and fused filament fabrication (FFF): Principles, history, and technical insights

Fused filament fabrication (FFF), also known as fused deposition modeling (FDM), is the most widely adopted material extrusion additive manufacturing (AM) method, both in consumer grade 3D printing and in a substantial portion of industrial prototyping. Patented in 1989 by S. Scott Crump (U.S. Patent No. 5,121,329), FDM was commercialized by Stratasys in the early 1990s, primarily for rapid prototyping, design verification, and conceptual modeling applications [16].

Its designation as the primary material extrusion AM technique reflects not only its historical importance but also its current dominant market share, low capital cost, simple process architecture, and compatibility with a wide range of thermoplastics. The expiration of core patents in 2009 accelerated democratization of the technology through the RepRap Project, initiated in 2005 by Adrian Bowyer at the University of Bath, which enabled the development of low cost, open-source printers [17]. This transition shifted FDM/FFF from specialized industrial tools to accessible platforms for education, hobbyist use, research, and functional part production across fields such as biomedical devices, electronics enclosures, tooling, and soft robotics.

FDM operates through the extrusion of heated thermoplastic filaments, primarily acrylonitrile butadiene styrene (ABS), polylactic acid (PLA), or elastomeric resins such as thermoplastic polyurethane (TPU) via a precisely controlled extrusion nozzle. As shown in Figure 1, the process involves the sequential layering of material onto a thermally conditioned build platform, following predefined G-code toolpaths which is the standard machine instruction language used in CAM processes, including FFF/FDM printing. Generated by slicing software, it provides line by line commands controlling motion, extrusion, and temperature, which the printer firmware executes to produce the part. This additive manufacturing method greatly speeds up prototyping and enables the creation of complex, customized shapes. Key process parameters, such as nozzle and bed temperatures, print speed, layer height, and infill orientation, significantly affect the mechanical properties, dimensional accuracy, interlayer adhesion, and, in cases involving conductive composite filaments, their electrical functionalities [18], [19].

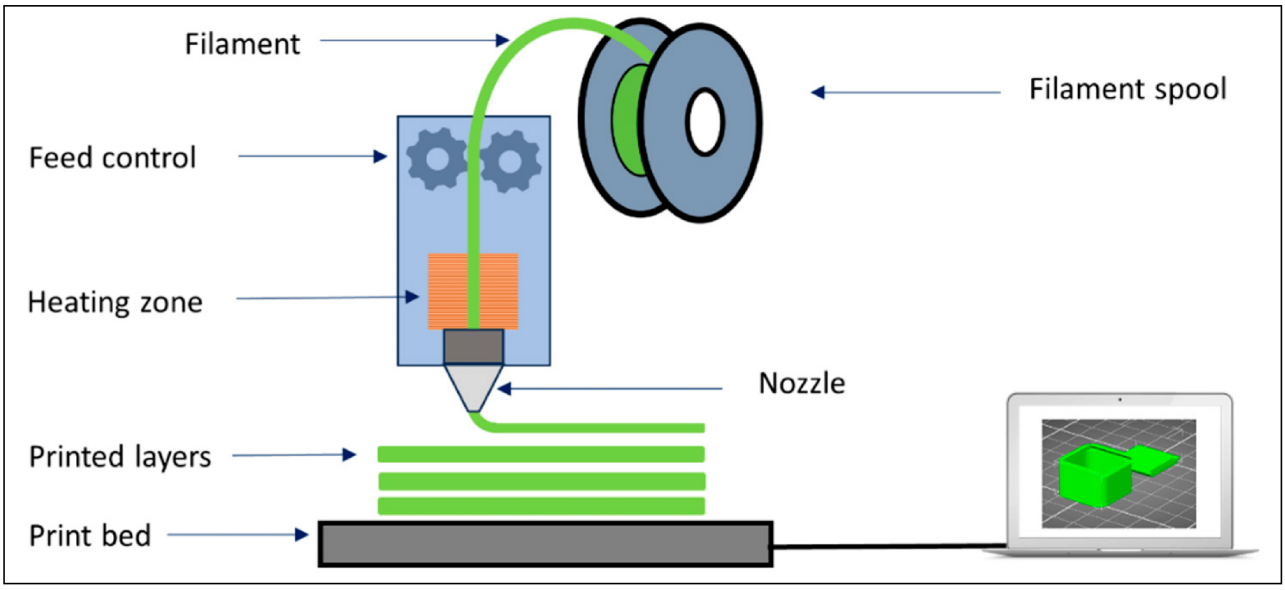

Figure 1: FDM schematic structure

Compared to other additive manufacturing methods, such as stereolithography (SLA) and selective laser sintering (SLS), FDM offers benefits in cost, mechanical strength, and ease of material handling. Unlike SLA, which requires photopolymers and curing steps, or SLS, which involves managing powders, FDM uses solid thermoplastic filaments, reducing complexity and lowering barriers for small scale and academic applications [20]. Figure 2 shows the schematic of SLA configuration in both direct write curing process and projection-based curing process. In SLA, liquid photopolymers must undergo controlled photo curing and post processing (washing, UV curing), which increases printing time and requires specialized handling. In SLS, polymer or metal powders must be carefully stored, spread, and recycled, and the build chamber must go through lengthy heating/cooling cycles; powder removal and filtration add further time and safety constraints. Compared to direct ink writing (DIW), FDM offers better mechanical handling, scalability, and throughput, making it an ideal choice for functional and wearable electronics.

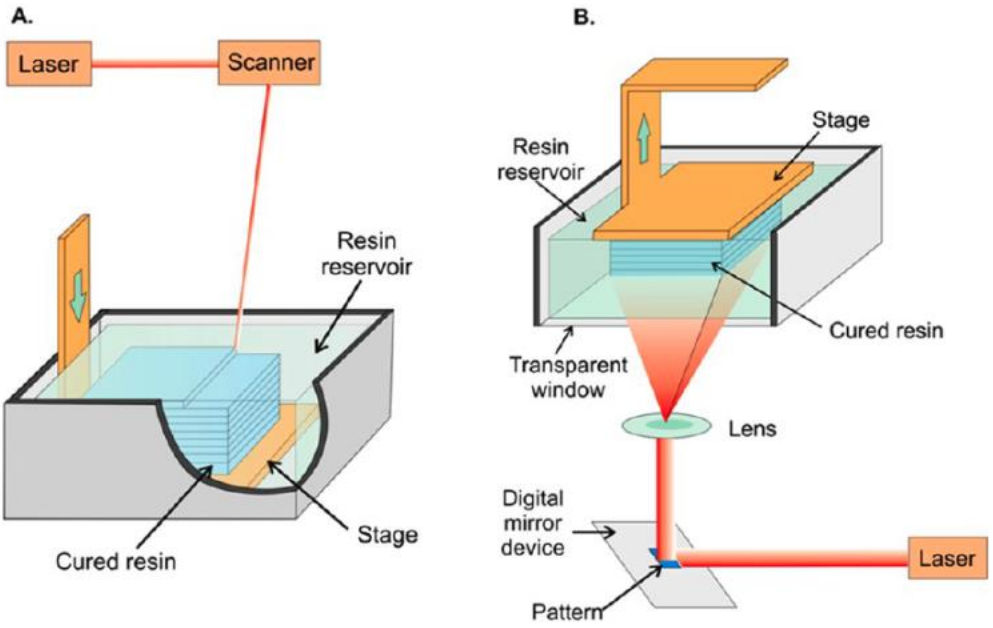

Figure 2: (A) Schematic of a bath configuration SLA printer with a direct write curing process. (B)Schematic of a layer configuration SLA printer with a projection-based curing method [20].

The evolution of FDM materials has greatly expanded their applications. Early filaments, mainly rigid ABS and PLA had limited flexibility and lacked modern functionalities, such as electrical conductivity. In the mid 2010s, polymer nanocomposite filaments with carbon-based fillers like carbon black (CB), graphene, and multi walled carbon nanotubes (MWCNTs) appeared, improving both mechanical and electrical properties [21]. MWCNT infused filaments, for example, allow for direct printing of piezoresistive and capacitive sensors by creating conductive percolation networks within polymer matrices [22].

The broader capabilities of soft matter 3D printing, including programmable control over composition and architecture across multiple length scales, have catalyzed innovations in soft sensors, shape morphing systems, and soft robotics. Building on this foundation, multi material FDM techniques, especially dual extrusion configurations, have further enabled direct embedding of conductive and insulating materials, using flexible polymers like TPU, thermoplastic elastomer (TPE), and copolyester HMA, for streamlined fabrication of wearable sensors and biomedical components. For instance, copolyester based hot melt adhesives, used as the polymer matrix for MWCNT composites, combine thermoplastic processability with strong adhesion, tunable viscosity, and high flexibility. These HMAs exhibit a low melting range (138–148 °C), excellent

wetting and bonding to substrates due to additives such as tackifiers, which are low molecular weight resins that enhance surface adhesion and improve interfacial bonding with both the substrate and embedded fillers. Tackifiers can also promote more uniform dispersion of nanofillers within the polymer matrix by increasing polymer–filler affinity and reducing filler aggregation, which helps maintain elasticity even after conductive nanofillers are incorporated. Such characteristics make them attractive candidates for fabricating flexible, conformable strain sensors via FFF 3D printing [3].

Despite these advancements, challenges remain in achieving uniform filler dispersion, strong interlayer bonding, and consistent electrical properties in printed nanocomposites. In producing conductive filaments, poor dispersion can cause filler agglomeration and disrupt conductive pathways. Twin screw extrusion provides better mixing than traditional single screw systems because the intermeshing screws exert both shear and elongational forces that help break up agglomerates and distribute fillers more evenly within the polymer matrix. This enhances interfacial bonding and improves both conductivity and electromechanical response. In some cases, twin screw extrusion is combined with techniques like solvent assisted mixing or masterbatch dilution to further improve dispersion. Careful control of printing parameters such as extrusion temperature, print speed, and layer thickness is essential to ensure consistent sensor performance.

2.3 Structural design and geometrical structures

The structural design and customization of 3D printed strain sensors are pivotal in controlling and tailoring their performance characteristics, including sensitivity, stretchability, and durability. This section reviews geometrical design strategies, the influence of FDM process parameters, customization capabilities, benefits and limitations of FDM, real world examples of functional strain sensors, and challenges associated with multi material printing.

Geometric design plays a critical role in optimizing the performance of 3D printed strain sensors. In additive manufacturing, geometric design refers to the deliberate patterning and layout of printed traces within a layer. For strain sensing applications there are common 2D geometries, which are depicted in Figure 3. The 2D configuration affects stretchability, gauge sensitivity, and stability under deformation. Common geometries include straight traces, serpentine paths,

horseshoe layouts, grid networks, and auxetic patterns. Each topology redistributes strain differently; serpentine and horseshoe layouts accommodate elongation through unfolding, grid structures balance isotropic response and stability, and auxetic patterns expand laterally when stretched, enhancing compliance. These geometries are thus selected based on desired sensitivity, mechanical durability, and manufacturing simplicity. Serpentine patterns are widely adopted due to their ability to accommodate large deformations through unfolding, enhancing stretchability.

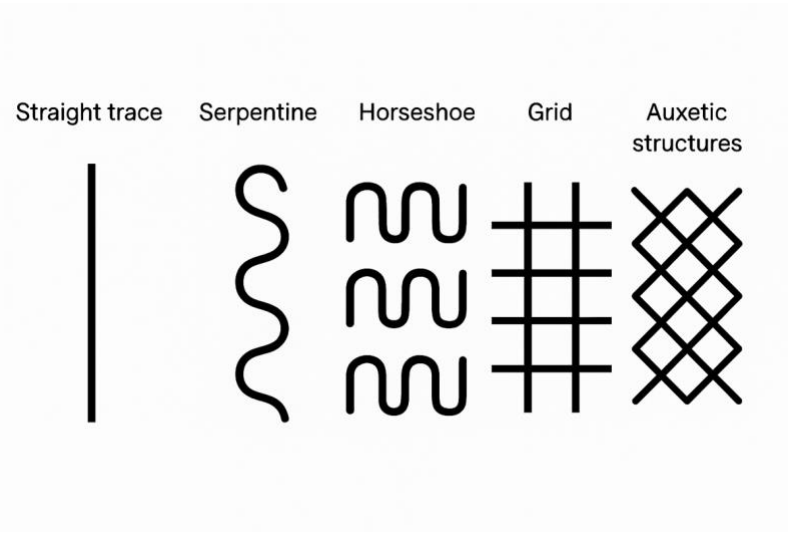

Figure 3: Common 2D geometries for printed strain sensors: straight, serpentine, horseshoe, grid, and auxetic patterns.

For instance, a serpentine shaped strain sensor using FDM with thermoplastic polyurethane (TPU) and a carbon black (CB) conductive layer achieved high stretchability and stability for gesture recognition applications [23]. The serpentine geometry allowed the sensor to maintain a stable conductive network under strain, demonstrating its suitability for wearable electronics. It can be seen in Figure 4 that strain can change the distribution of stress in the substrate, and that can result in changes in resistivity and gauge factor. This behaviour arises because the serpentine path redistributes tensile deformation through bending and unfolding rather than direct axial stretching of the conductive layer. As a result, fewer conductive pathways are ruptured during elongation, enabling the sensor to sustain electrical continuity at strains approaching 200%. The study further showed that after Dimethylformamide assisted softening, the serpentine structure enhanced extensibility and reduced required tensile force, helping to preserve carbon nanotube

(CNT)/carbon black (CB) particle contacts during deformation. This structural robustness contributed to a high gauge factor (58.08), a rapid response time (~0.1 s), and mechanical durability over 1000 strain cycles, supporting reliable use in gesture recognition and wearable monitoring applications.

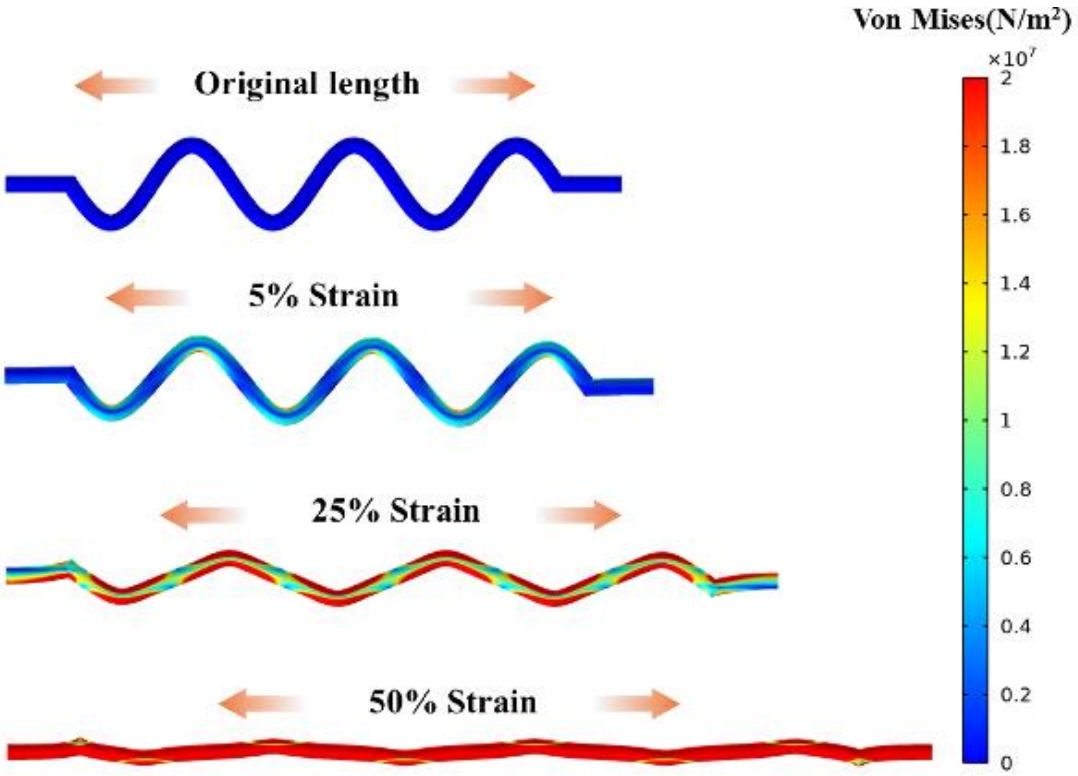

Figure 4: Simulation of mechanical properties of the serpentine-shaped substrate [23].

Auxetic structures, characterized by a negative Poisson's ratio, which describes how a material changes shape in directions perpendicular to an applied load, have been explored to improve sensor sensitivity. When a material is stretched in one direction, it typically becomes thinner in the transverse direction; when compressed, it expands laterally. A stretchable strain sensor utilizing a continuous fiber reinforced auxetic structure fabricated via direct ink writing (DIW) exhibited a gauge factor (GF) of 18.23 at 20% strain, representing a 2.52-fold increase in sensitivity compared to non-auxetic designs [24]. The fabrication process is being shown in Figure 5. The auxetic structure's lateral expansion under tensile strain enhanced the piezoresistive response, making it ideal for motion detection. A key conclusion from the study is that the auxetic lattice not only improves sensitivity through lateral expansion but also provides exceptional mechanical

robustness and durability during repeated loading. The negative Poisson's ratio helps stabilize conductive pathways by preventing excessive thinning under tension, allowing the sensor to maintain signal integrity over large deformation. The authors further demonstrated reliable cyclic performance, fast response, and consistent strain dependent resistance change, indicating strong potential for wearable motion monitoring systems. Taken together, these results confirm that auxetic structural engineering is an effective strategy to enhance both sensitivity and mechanical resilience in stretchable strain sensor architectures.

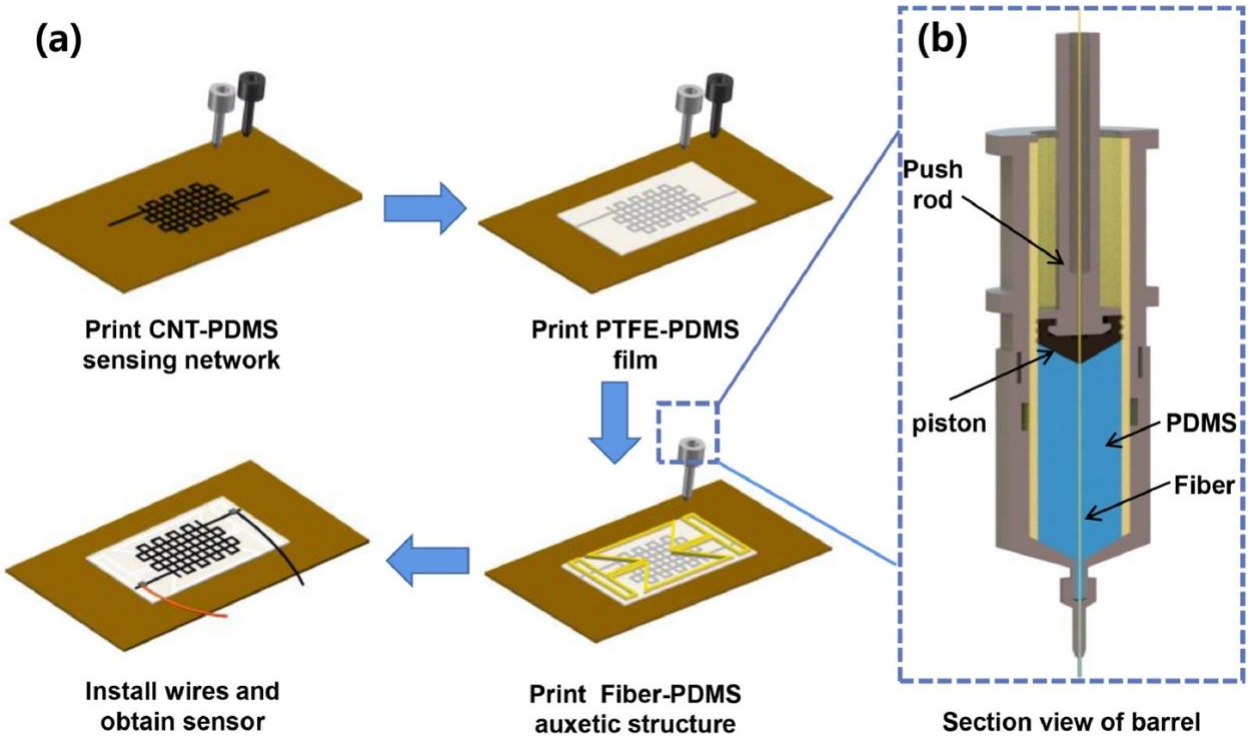

Figure 5: (a) Fabrication process of the auxetic structure sensor; (b) Section view of the barrel for printing the auxetic structure [24].

In addition to serpentine and auxetic layouts, the use of cell-based metamaterial architectures offers a structural approach to program how a sensor deforms, and therefore how it transduces signal while preserving the interior architecture needed for routing electrodes and dielectrics. Overvelde et al. [25] showed that unit cell geometry alone can prescribe kinematic pathways (e.g., hinging, buckling, snap through) that are repeatable and spatially localized across a lattice. For multi-material FDM/DIW, this is directly useful, by assigning conductive faces to specific cell walls and insulating faces to others, we can co-print electrodes and dielectrics inside the lattice

without obstructing its voids or hinges. During loading, the lattice governs where gaps close, areas overlap, or distances change; the conductive/non-conductive faces merely read out those geometric changes as piezoresistive or capacitive signals. In practice, this yields sensors whose sensitivity are set primarily by cell geometry (wall thickness, ligament length, hinge angle) rather than by fundamental material patterns, and whose internal channels remain open for wiring, strain relief, or fluidic routing.

Paulose et al. [26] developed a class of mechanical metamaterials whose deformation is guided not only by geometry but also by topological states of self-stress. In these lattices, certain internal patterns store mechanical "tension routes," which determine where the structure prefers to bend or buckle when stretched. In simpler terms, the structure is designed so that when you apply strain, only specific regions deform, while the rest remains comparatively rigid. The deformation is therefore not random – rather, it is funneled toward particular pathways set by the lattice's topology. This targeted deformation has important implications for sensing. Because strain concentrates in predictable zones, conductive pathways in the rest of the material experience minimal distortion. As a result, sensors embedded in such lattices show reduced signal drift, hysteresis, or loss of conductivity, even under large and complex motion. In effect, the topological design "protects" the conductive network by localizing strain in non-critical regions while preserving structural and electrical continuity in the rest. This can enhance measurement fidelity, long term stability, and performance in flexible or wearable devices.

2.4 Effect of printing parameters on the conductivity of 3D printed conductive composites

The electrical conductivity of 3D printed conductive polymer composites, typically measured inversely through resistivity or resistance, is critically influenced by printing parameters in fused filament fabrication (FFF) or fused deposition modeling (FDM). These parameters influence the formation of percolated conductive networks within the polymer matrix, which is often filled with carbon-based additives such as carbon black (CB), carbon nanotubes (CNTs), or graphene. 3D Printing parameters can alter conductivity drastically, primarily due to changes in filler alignment, interlayer fusion, void formation, and material homogeneity. This section synthesizes findings from key studies on rigid (PLA/ABS based) and flexible (TPU/thermoplastic starch (TPS) based) composites, highlighting common parameters such as layer height, printing orientation/infill angle,

temperature, and others like nozzle diameter, extrusion rate, and annealing. Comparisons reveal trade-offs between conductivity, mechanical stability, and print quality, with gaps in multi-parameter optimization and long-term performance under strain or environmental stress.

2.4.1 Layer height

Layer height has a significant impacts conductivity by influencing interlayer bonding and filler distribution. From one aspect, a thinner layer height means that more layers are needed to build a structure of the same height. This inherently results in more interlayer bonding between printed paths, which increases the overall resistivity of the printed structure. Thinner layers also often lead to higher resistivity due to increased voids, shear disruption of conductive paths, and nozzle clogging, particularly in high viscosity MWCNT filled composites. Thicker layers generally improve conductivity through better fusion and slower cooling, promoting homogeneous structures which can lead to better bonding between layers. For instance, Pentek et al. [27] systematically studied how layer height (100–400 μm) and printing orientation (X vs Z) affect resistance in carbon filled PLA and ABS composites produced via FFF. They observed that, for PLA printed in the X orientation, increasing the layer height from 100 μm to 400 μm increased measured resistance from ~10 kΩ to ~26 kΩ, indicating that thicker layers reduced interlayer contact quality, resulting in poorer formation of conductive pathways. In contrast, ABS in the X orientation remained stable at ~5 kΩ over the same layer height range, suggesting that its conductive carbon phase was more evenly dispersed and maintained electrical connectivity even as the lamella thickness increased.

In the Z-orientation, both materials showed consistently high resistance (~200 kΩ) that changed little with layer height. This is explained by the fact that current must cross interlayer boundaries in Z, where MWCNT/CB alignment is disrupted and polymer interfaces dominate, producing strong electrical insulation and preventing formation of continuous conduction pathways. Similarly, follow up work by Dembek et al.[28] reported that excessively small layer heights (<0.2 mm) caused printing failures, and that resistivity decreased from ~15 Ω·cm (0.3 mm/0.4 mm nozzle) to ~3 Ω·cm (1 mm/1 mm nozzle), stabilizing when height exceeded 0.3 mm, consistent with the idea that thicker layers and larger nozzles promote more continuous conductive filaments. In flexible TPU/TPS elastomers, Glogowsky et al. [29] found that increasing layer thickness (200–

300 μm) significantly reduced resistivity for TPU15CNT, decreasing from ~82 Ω·cm to ~11 Ω·cm. TPU15CNT refers to a custom TPU-based masterbatch blended with ~15 wt.% MWCNT, giving it high filler loading and strong conductive network formation. The pronounced improvement with thicker layers is attributed to reduced internal void formation and enhanced interlayer MWCNT percolation under slower cooling at higher print volume. By contrast, TC8OEX, a commercially available TPS-based elastomer containing carbon black, showed no major layer height dependence, with resistivity remaining ~7–10 Ω·cm across different thicknesses. Its relatively stable behaviour is attributed to its high carbon black filler fraction, which ensures that conductive pathways persist even when printing constraints introduce voids or imperfect layer fusion. Meanwhile, Eel (a commercial TPU with <18% carbon black) could not be reliably printed above 100 μm due to flow instability and insufficient stiffness. Its comparatively low filler content makes conductive path formation more sensitive to microstructural defects. Overall, optimal layer heights fell around 0.3–0.5 mm for rigid composites and 200–300 μm for elastomers, balancing conductivity and print quality. In general, thinner layers worsen anisotropy, especially in the Z-axis, because thermal gradients and weak interlayer fusion reduce filler bridging between layers, increasing resistance.

However, increasing layer height also introduces drawbacks. Thicker layers reduce dimensional accuracy and surface quality because the printed filament traces are less able to follow fine geometric details, producing more pronounced layer stepping and rougher surfaces. This limits resolution for small features and may hinder sensor integration where tight tolerances are required. Additionally, thicker layers can trap internal voids if cooling is uneven, which can compromise mechanical uniformity even when electrical conductivity improves.

2.4.2 Orientation angle (infill angle)

Orientation angle dictates filler alignment relative to current flow, with perpendicular paths increasing resistance. Fillers like MWCNTs or CB tend to orient along the print direction due to shear flow, creating anisotropic conductivity where paths parallel to the flow of the electrical current minimize tortuosity and electron hopping distance, while perpendicular orientations increase effective resistance by forcing charge carriers through insulating polymer regions. Pentek et al. [27] highlighted that conductivity along the Z axis (perpendicular to the printing direction)

yielding 100x higher resistance than X axis (along the printing direction) (~200 vs. 10–26 kΩ for PLA; 50 vs. 5 kΩ for ABS), attributed to orthogonal carbon alignments and interlayer insulators via SEM. Lee et al. [30] noted that increasing the lamination angle which is, the direction in which individual layers are deposited relative to the reference axis, from 0° to 45° increased the initial resistance (4790 Ω compared to 3071 Ω for a single layer). This effect diminished once the printed thickness exceeded approximately 3.6 mm. The authors attributed this behaviour to shrinkage and the formation of nonuniform crystalline grains, referring to heterogeneous semicrystalline domains that develop during polymer cooling and locally disrupt conductive pathways.

Glogowsky et al. [29] further showed that infill orientation strongly influences electrical performance: lengthwise deposition (90°) yielded the lowest resistivity (approximately 11 to 140 Ω·cm), diagonal patterns at 45° provided intermediate values (approximately 20 to 200 Ω·cm), and crosswise deposition at 0° produced the highest values (approximately 80 to 300 Ω·cm). This trend is consistent with the extrusion shear field aligning conductive fillers, such as MWCNTs or carbon black, along the printing direction, thereby enhancing conduction along the alignment direction. For the proprietary conductive elastomer TC8OEX, however, 90° infill caused mechanical instability, likely due to its softer matrix and the anisotropic stress field associated with highly aligned printed strands. Perpendicular Z axis orientations were unsuitable for electrical transport because insulating layers lie between adjacent printed traces, preventing efficient filler bridging. Overall, while 45° infill offers a compromise between mechanical stability and electrical performance, lengthwise deposition (90°) remains ideal when maximizing conductivity is the primary objective.

2.4.3 Printing nozzle temperature

Printing nozzle temperature plays a key role in determining the electrical conductivity of 3D printed conductive polymer composites by influencing the material's flow, filler distribution, and overall microstructure during extrusion. At lower printing temperatures, the polymer melt remains highly viscous, which increases resistance to flow and makes it harder for the conductive fillers to move or align within the matrix. This elevated melt viscosity inhibits uniform filler dispersion and wetting of the polymer by the filler, leading to clumping or local aggregation of the conductive particles. These filler agglomerates and poorly wetted zones act as discontinuities in the conductive

network, creating gaps or voids that disrupt the pathways and therefore result in higher resistance and lower conductivity. Insufficient heat also reduces layer fusion, when adjacent printed tracks or layers fail to adequately interdiffusion, insulating interfaces may form, further hindering charge carrier movement across the part.

This phenomenology is supported by previous research. For example, Iffelsberger et al. [31] found that increasing nozzle temperature in a PLA/graphite filled composite improved conductivity because higher melt temperatures reduced viscosity, improved particle wetting, and enabled better dispersion of graphite flakes within the PLA matrix. In the study by Paz et al. [32], the authors observed that in graphene-nanoplatelet/ABS composites the electrical conductivity of printed parts improved when printing at higher temperatures, which they attributed to lower viscosity, fewer interlayer defects, and improved filler continuity. More generally, the review by Ma et al. [33] on 3D printed polymer composites highlights that thermal processing (including nozzle temperature) modulates rheology, filler alignment, and void formation, all of which strongly impact electrical performance.

By contrast, when the nozzle temperature is too low, the melt may cool and solidify too rapidly after extrusion, limiting filler migration and hindering the formation of well-connected conductive networks. Under these conditions, higher pressure and shear may be required to force material through the nozzle, increasing shear-induced filler breakup or misalignment and creating more internal stress or micro-voids. These structural defects act as additional electrical resistances. Furthermore, poor fusion between layers further compounds the problem by introducing insulating interfaces perpendicular to current flow. Thus, optimal nozzle temperatures strike a balance between sufficient melt fluidity to allow filler movement and dispersion, while avoiding excessive degradation or polymer damage at high temperatures. As temperature increases within an optimal range, viscosity drops significantly, allowing better flow and more uniform distribution of fillers. This promotes the formation of continuous percolated networks where fillers connect effectively, reducing interfacial resistance and enabling smoother electron transport, thus improving conductivity.

However, excessively high temperatures risk degrading the polymer matrix through chain breaking or oxidation, introducing defects that scatter charge carriers and raise resistance. Overheating can

also lead to uneven cooling, causing stresses that warp the structure or misalign fillers, offsetting any gains in dispersion. Dembek et al. [28] showed 230°C optimal (ρ=3.40 Ω·cm), with 210°C causing clogging/high ρ (4.85 Ω·cm) and 250°C lowering ρ (2.89 Ω·cm) but degrading PLA. Glogowsky et al. [29] reported higher temperatures (220–240°C) decreased ρ in TC8OEX (10 to 7 Ω·cm) and TPU15CNT (30 to 11 Ω·cm), insignificant for Eel (~200–300 Ω·cm) due to brittleness. Ambient temperature also affects conductivity, with Pentek et al. [27] finding lower resistance indicating metal like behaviour, possibly due to reduced thermal scattering in fillers.

2.4.4 Infill density

Infill density determines how much of the printed volume is solid material versus internal voids. Higher infill density creates denser internal networks, reducing electrical resistance. Increasing infill decreases the volume of insulating voids and increases the number of continuous conductive pathways within the printed part. This effectively lowers the percolation threshold by keeping conductive filler domains in closer proximity, thereby enhancing electron transport efficiency. Pentek et al. [27] demonstrated this effect in PLA and ABS specimens printed with their filament roads aligned along the X axis (printing direction). In this configuration, conductive traces follow the same direction as the extrusion flow, promoting stronger interparticle contacts. Under these conditions, 100 percent infill resulted in the lowest resistance (~5–8 kΩ for PLA printed along X; ~1–2 kΩ for ABS printed along X), while 20 percent infill yielded the highest (~10–16 kΩ for PLA; ~2.5–4 kΩ for ABS). An anomaly occurred at 50 percent infill for PLA, where the resistance deviated from the expected monotonic trend; this behaviour was attributed to incomplete fusion between adjacent extruded roads or heterogeneous filler dispersion interrupting continuous conductive pathways.

2.4.5 Post-print annealing

Annealing is widely used in FDM-printed conductive composites to relieve residual stresses generated during rapid heating–cooling cycles and shear-induced molecular orientation. In FDM, conductive PLA filaments are melted, extruded, and quenched too quickly for polymer chains to fully relax, which creates internal stress, non-uniform crystal grains, and disrupted conductive pathways. These microstructural defects increase electrical resistance and reduce conductivity. Lee

et al. [30] demonstrated that thermal annealing provides enough mobility to relax these stresses, promote grain refinement, and reduce defect density, thereby improving electron transport. Lee found that thermal annealing (2h at 120°C) reduced resistance up to 43% (in thinner/45° samples), via stress relief and grain refinement. Post-print annealing reduces resistance because it directly targets the internal stresses and microstructural defects created during FDM printing. During extrusion, the molten PLA/carbon black filament cools too rapidly to reach an energetically stable configuration. Shear gradients at the nozzle wall further create regions of high dislocation density and uneven grain sizes. Lee et al. observed that annealing at 120 °C reduced electrical resistance by approximately 42% across both 0° and 45° lamination angles, whereas annealing at 62 °C produced no meaningful conductivity improvement because chain mobility remained insufficient. These results confirm that annealing refines microstructure and enhances electrical conductivity mainly by eliminating stress-induced defects.

2.4.6 Printing speed

Printing speed exhibited only a limited influence on the electrical conductivity of the conductive thermoplastic composites studied in the literature. Glogowsky et al. [29] evaluated multiple commercially available conductive filaments and found that resistivity remained largely unchanged across the tested printing speeds of 1600 to 2400 millimetres per minute. Three commercially available conductive elastomer filaments were evaluated in their work. TPU15CNT, TC8OEX, and Eel. TPU15CNT is a thermoplastic polyurethane containing a high loading of carbon nanotubes, providing stable conductivity with flexibility. TC8OEX is a proprietary thermoplastic elastomer with a high concentration of carbon black, yielding relatively low resistivity. Eel is a soft, highly elastic conductive TPU with moderate conductivity. These materials together represent different combinations of flexibility and filler content, enabling comparison of how printing parameters influence electrical behaviour. Their statistical analysis showed that neither TC8OEX nor TPU15CNT displayed significant variation in resistivity across this speed range. Only the Eel material showed a measurable difference between the lowest and highest speeds, and even this change was modest in magnitude. Because higher printing speeds did not negatively affect resistivity, the authors concluded that it is generally preferable to use higher speeds to reduce fabrication time without compromising electrical performance.

Glogowsky also found speed had minimal effect (1600–2400 mm/min), but Object by Object mode (slower cooling) lowered resistivity vs. Layer by Layer for Eel.

2.4.7 Nozzle diameter

Larger nozzle diameters generally improve conductivity because they allow lower shear during extrusion, producing more stable material flow and reducing the likelihood of defects that interrupt conductive pathways. Dembek et al. [28] showed that conductive PLA composites printed with 0.8–1.0 mm nozzles exhibited stable resistivity values of approximately 3 Ω·cm, whereas smaller nozzles (0.4–0.5 mm) produced significantly higher resistivity in the range of 8–15 Ω·cm, in part due to increased flow instability and clogging at the die. These results indicate that electrically conductive thermoplastics processed through FDM benefit from higher material throughput and reduced shear. Rigid matrices such as PLA and ABS were found to be highly sensitive to geometric parameters like layer height and orientation, while elastomer-based systems responded more strongly to process parameters such as temperature and infill angle. Materials with higher conductive-filler content, such as TC8OEX, tended to show more stable resistivity across processing conditions, reflecting their more robust percolation structure.

2.5 Dispersion, percolation, and conductivity mechanism

In the development of conductive polymer nanocomposites, particularly those used in additive manufacturing techniques like FDM, understanding the mechanisms of dispersion, percolation, and conductivity is critical. These factors directly influence the electrical performance and mechanical properties of the resulting materials, which are crucial for applications such as strain sensors, wearable electronics, and flexible circuits. Fillers must be uniformly distributed throughout the polymer matrix to form an effective percolated network that facilitates electron transport. However, because of their inherently high aspect ratio and surface energy, MWCNTs, in particular, tend to agglomerate strongly, which leads to discontinuity in conductive pathways. This phenomenon is often referred to as filler agglomeration, and it significantly reduces the effectiveness of the conductive fillers, leading to localized conductivity and compromised mechanical properties [34].

To address dispersion challenges, surface functionalization of MWCNTs is commonly employed to improve their compatibility with polymer matrices. Functionalised MWCNTs exhibit reduced agglomeration and enhanced interfacial interaction, leading to improved composite homogeneity [35]. Additionally, methods such as sonication, melt mixing, and solution casting are commonly used to enhance the dispersion of MWCNTs within the polymer matrix. These techniques ensure that the fillers are more uniformly distributed, which is essential for creating continuous conductive networks. The concept of percolation is crucial to understanding conductivity in MWCNT based polymer composites. Percolation refers to the formation of a continuous conductive network within the composite once the filler reaches a critical concentration. Below this critical concentration, known as the percolation threshold, the material behaves as an insulator. Once the percolation threshold is surpassed, however, the material exhibits a dramatic increase in electrical conductivity, as a continuous network of conductive pathways is formed, and it maintains a steady conductivity after surpassing the percolation threshold, as shown in Figure 6.

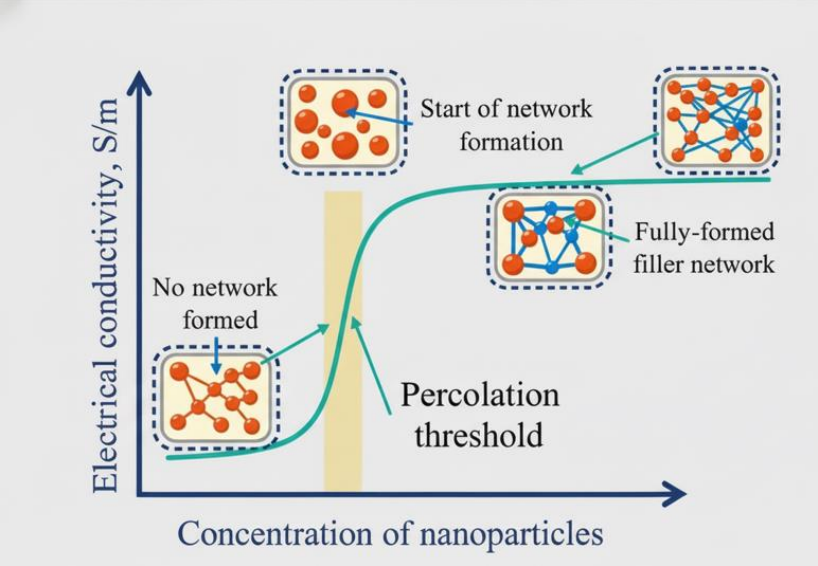

Figure 6: Schematic illustration of the electrical conductivity (percolation) behavior of a composite as a function of conductive nanoparticle concentration.

The percolation threshold in MWCNT based composites is generally very low due to the exceptional aspect ratio and electrical conductivity of MWCNTs. Even small amounts of MWCNTs can significantly enhance the electrical properties of the composite once the percolation

threshold is achieved. However, the exact value of the percolation threshold is influenced by several factors, including the polymer matrix, and the processing conditions.

Percolation is often described mathematically using percolation theory, which is grounded in statistical mechanics. The theory models the behaviour of a network of sites or bonds (in the case of conductive composites, these are the fillers) that are either occupied or unoccupied. The transition from insulation to conduction occurs when the occupied sites or bonds form a continuous path throughout the system. A percolation probability represents this, typically modeled using a power law:

$$\sigma \sim (\phi - \phi_c)^{\beta} \tag{2.1}$$

where:

- σ is the conductivity,
- ϕ is the volume fraction of the filler,
- ϕ_c is the percolation threshold
- β is the critical exponent.

This power law relationship indicates that conductivity increases exponentially as the filler concentration approaches and surpasses the percolation threshold [36].

Percolation models have been developed to describe the relationship between filler loading and conductivity. These models typically exhibit a power law relationship, where the conductivity increases exponentially with increasing filler content once the percolation threshold is crossed. Studies have shown that MWCNTs, due to their multi layered structure, tend to form percolated networks at lower loadings compared to single walled CNTs (SWCNTs) [34]. For example, MWCNT filled polymer composites may exhibit percolation at as low as 1 wt.% MWCNTs [3], while SWCNTs require slightly lower loadings due to their higher aspect ratio and different dispersion characteristics [37].

Once the percolation threshold is surpassed, MWCNTs form a continuous network that allows for efficient electron transport. The conductivity mechanism in MWCNT composites involves both

electron hopping and ballistic transport. In regions where MWCNTs are well dispersed and aligned, charge carriers can travel with minimal scattering, leading to ballistic transport. However, in regions with poor dispersion or agglomerated MWCNTs, charge carriers must rely on electron hopping between adjacent MWCNTs, which can introduce resistance and reduce conductivity.

The polymer matrix also plays an important role in the conductivity mechanism. A strong interface between the MWCNTs and the polymer is essential for effective charge transfer. Poor interfacial bonding can result in weak conductive pathways, reducing the overall conductivity of the composite. To enhance interfacial bonding, polymer matrices may be modified with additives or compatibilizers that improve the interaction with MWCNTs. Additionally, MWCNT loading must be optimized to balance conductivity and the mechanical properties of the composite. Too much filler can lead to brittleness and reduced flexibility, which is undesirable for applications such as wearable electronics or flexible sensors [35], [38], [39].

2.6 Conductive fillers in composite resins

Carbon conductive filler can be classified by their dimensionality: zero dimensional (0D, CB), one dimensional (1D, such as CNTs and carbon fibers (CF)), two dimensional (2D, graphene, graphene nanoplatelets (GNP), graphite nanosheets (GNS)), and three dimensional (3D, like bulk graphite, porous carbons, carbon foams). The ordered arrangement of carbon atoms in these materials confers several advantages, including high electrical conductivity, chemical stability, low density, and strong mechanical properties. Owing to their excellent conductivity, carbon materials are frequently used as fillers in polymer composites, transforming insulating polymers into conductive ones. Additionally, they improve the processability and mechanical strength of these composites.

2.6.1 Carbon black

Carbon black (CB) is the most widely used carbon material due to its light weight, low cost, and good conductivity. As the first carbon material employed as a conductive filler in polymer composites, it remains the most used conductive filler in industrial applications [34], [40]. Smaller particle size, greater complexity, and fewer surface active groups in Carbon black would lead to an increase in conductivity. Scientists initially found it possible to create conductive composites by adding a high amount of carbon black fillers, which makes the composite's processing more

difficult and reduces its desired mechanical properties [41]. Currently, CB research focuses not on increasing the traditional dosage, but on enhancing the electrical conductivity of composites by lowering CB's threshold content and altering the filling method. One problem with immiscible polymer blends is that the weak adhesion between phases often reduces their mechanical strength. To address this, researchers have used double percolation structures, in which conductive fillers are concentrated in just one phase of the blend instead of spreading across the whole matrix. This makes it easier to form a conductive network and lowers the percolation threshold. Chen [42] worked on a polystyrene/polypropylene (PS/PP) blend (60/40), where carbon black (CB) was mainly dispersed in one phase. The result was a strong double percolation structure with a much lower percolation threshold. Still, the material's toughness needed improvement. By adding a small amount (2 wt.%) of SEBS, Chen managed to keep the double percolation arrangement while improving both the electrical properties and the mechanical performance. (Figure 7)

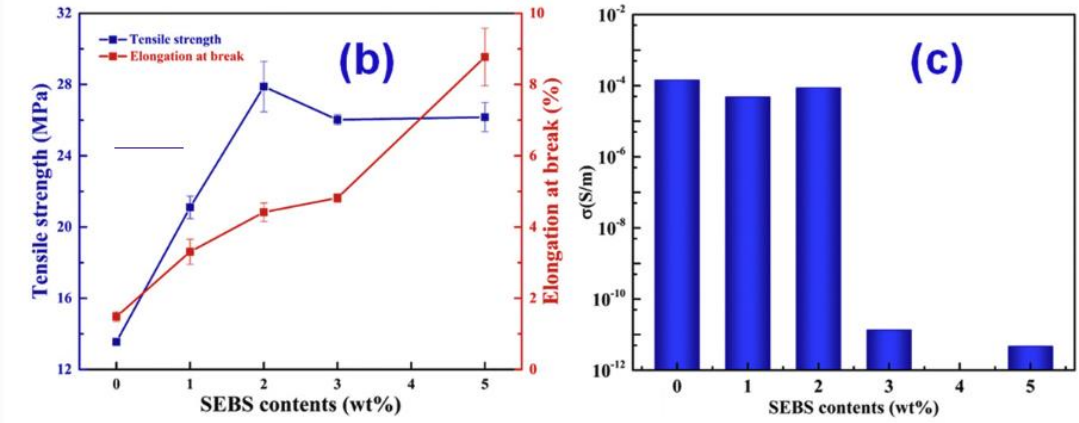

Figure 7: Effect of styrene-ethylene/butane-styrene (SEBS) content on the (b) tensile properties (strength and elongation at break) and (c) electrical conductivity of CB/styrene-ethylene/butane-styrene (SEBS)/polystyrene (PS)/polypropylene (PP) composites [42].

Previously, Gao et al. [43] had demonstrated a similar concept using polyether ether ketone/thermoplastic polyimide (PEEK/TPI) blends with CB. By controlling the distribution of CB through melt blending, they reduced the percolation threshold from approximately 10 wt.% to 5 wt.% (Figure 8).

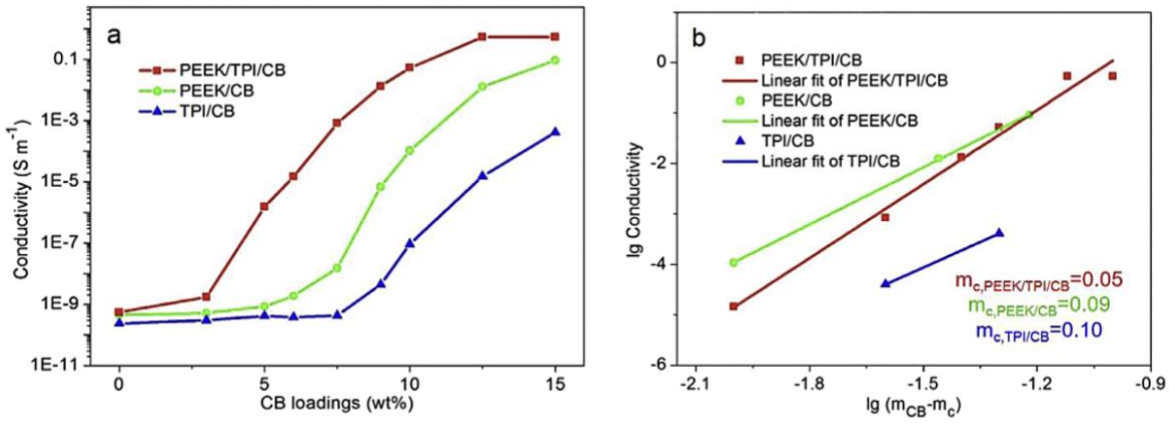

Figure 8: (a) Effect of CB content on the conductivity of the composites at 1 kHz (b) Linear fit of conductivity of the composites [43].

2.6.2 Carbon nanotubes

In 1991, Japanese scientist Sumio Iijima discovered carbon nanotubes (CNTs) while working on the preparation of C60 using an arc discharge method [44]. CNTs are essentially rolled up graphite sheets that form hollow cylindrical structures. Their one-dimensional hollow shape grants them a high aspect ratio. Due to this high aspect ratio and their extensive surface area, CNTs tend to disperse unevenly within a polymer matrix, often leading to agglomeration and the formation of stress concentration sites. While their exceptional aspect ratio allows the formation of percolating networks at relatively low loadings, achieving such networks in printed parts depends on two key factors: (1) ensuring stable dispersion during compounding and filament fabrication, and (2) maintaining inter road and inter layer contacts during printing to preserve conductive pathways despite geometric discontinuities inherent in FDM.

On the compounding side, a two-step dispersion route, forming a MWCNT-rich masterbatch (often via solution casting), followed by melt mixing, consistently outperforms single step melt blending. An efficient variant for PLA uses a small amount of lignin as a bio dispersant/plasticizer. In a PLA/MWCNT system, adding just 1 wt.% lignin at 5 wt.% MWCNT transformed the composite

from near insulating (~2.8×10^{-7} S·cm^{-1} without lignin) to ~1.4×10^{-1} S·cm^{-1}, while improving FFF printability and interlayer adhesion relative to PEG enough to power simple printed circuits [45].

Beyond dispersion, morphology engineering provides another powerful strategy to lower the percolation threshold in CNT polymer composites. Instead of dispersing CNTs uniformly throughout a single phase polymer, researchers have explored double percolated polymer blends, in which two immiscible polymers form a co continuous morphology, allowing CNTs to migrate into one of the phases selectively as it can be seen in Figure 9 [46]. In such systems, the conductive filler is not wasted in the insulating phase. Instead, it concentrates in the continuous domain, forming an interconnected conductive scaffold that spans the entire material at a much lower global CNT loading.

A representative case is the percolation behaviour in a polylactic acid /low density polyethylene/carbon nanotube (PLA/LDPE/CNT) system. Here, CNTs preferentially localize in the LDPE phase during melt mixing, assisted by thermodynamic affinity and viscosity contrast. Because LDPE forms a co continuous network with PLA, the CNT rich LDPE phase effectively becomes a conductive highway embedded within the PLA matrix. This morphology allows the overall composite to achieve electrical connectivity at far lower loadings than would be possible in a single-phase material. The percolation threshold was reduced to ~0.208 vol% (~5.56 wt.%), and at 7.5 wt.% CNT the conductivity increased by a factor of ~13.8 compared with an LDPE/CNT control prepared without PLA. The improvement was attributed to selective CNT migration, phase co continuity, and filler confinement at the phase interface, all of which enhance network density without requiring higher overall filler content [46].

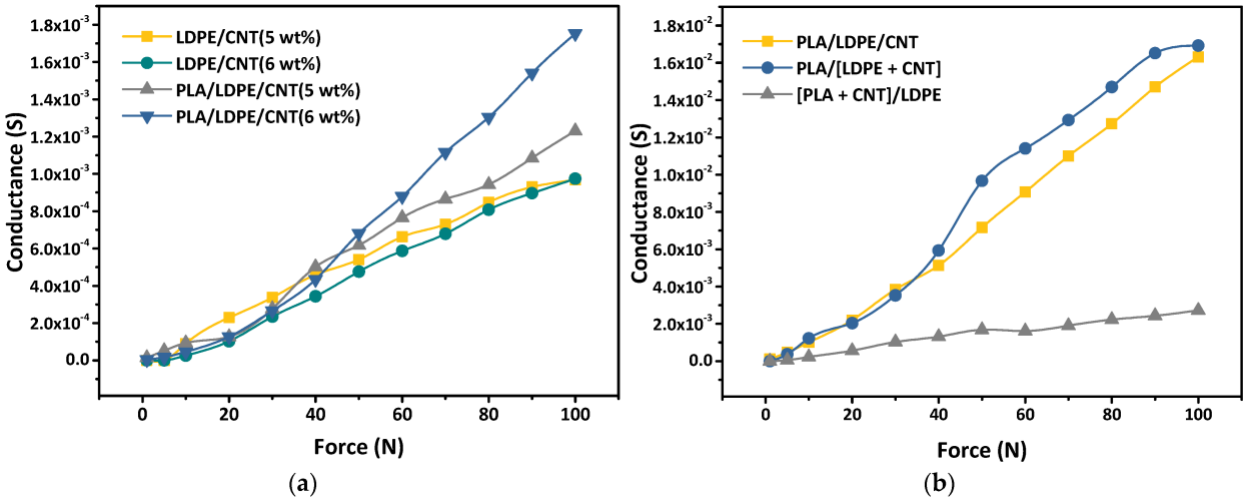

Figure 9: The influences of (a) CNT loading contents and (b) melt mixing sequences on the electrical responsiveness property of the composites [46].

2.6.3 Carbon fibers

Carbon fiber (CF), especially in shortened or chopped form, serves as an effective conductive filler in polymer composites for FDM. Compared to MWCNTs or carbon black, CF needs a higher loading to reach percolation, usually around 8–12 wt.% in PLA based systems. For example, hybrid polypropylene (PP) composites containing CF and carbon black achieved conductivity sufficient for electromagnetic interference (EMI) shielding, even though their percolation thresholds were above 5 wt.% CF. When used in a hybrid system, percolation thresholds and conductivity performance improved compared to CF only systems, showing that CF can connect conductive networks more effectively when mixed with other carbon fillers [47]. CF also brings unique anisotropy due to alignment during extrusion: fibers tend to orient along print paths, resulting in direction dependent conductivity [48]. In silicone-based matrices, printed parts showed resistivity in the print direction ~6–7x higher than in the transverse direction, which is a direct result of fiber orientation and stacking [49].The inclusion of CF notably enhances mechanical properties such as tensile modulus, strength, and thermal stability. A recent study reinforced both PLA and ABS with 1–5 wt.% CF, identifying 3 wt.% CF as the optimal balancing point between improved strength and minimal agglomeration. For ABS with 3 wt.% CF, tensile strength reached ~29.7 *MPa*, for PLA with the same CF content, mechanical gains were also observed. The best overall performance, including impact resistance, tensile strength, and uniformity, was achieved

at these mid range loading levels, as higher loadings (5 wt.%) caused performance declines likely due to CF clustering [50].

2.7 Current state of the art in 3D printing of conductive filaments

A significant number of studies have focused on the properties and applications of commercially available conductive filaments. Flowers et al. [1] investigated dual material fused deposition modeling (FDM) for 3D printing electronic components and circuits using three commercially available conductive PLA filaments with carbon black, graphene, or copper fillers. They evaluated the resistivity, mechanical durability, and high frequency impedance of the printed traces, finding values of about 12 Ω·cm (carbon black), 0.78 Ω·cm (graphene), and 0.014 Ω·cm (copper). The copper-based filament exhibited the lowest resistivity, superior mechanical resilience, and impedance comparable to that of copper PCB traces above 1 MHz, enabling higher performance printed circuits. In contrast, while the carbon black and graphene-filled filaments were functional, they proved to be brittle, fracturing with minimal bending. This brittleness limits their suitability for flexible or mechanically dynamic applications. The copper filament maintained electrical performance after over 500 bending cycles. By leveraging dual material printing, the authors created resistors, capacitors, and inductors whose properties could be predictably adjusted through geometry or material selection. These components were integrated into a fully 3D printed high pass filter with performance comparable to traditional components, as well as a wireless power receiver coil. The study also demonstrated embedding and connecting surface mounted devices within printed structures using a low cost, open-source dual material printer, underscoring FDM's potential in producing complex, three dimensional circuits with both printed and embedded electronic elements.

Al Rubaiai et al. [51] developed a fully 3D printed, stretchable wind sensor in which the conductive filament serves as both the structural and electronic sensing element. Fabricated via dual extrusion FDM, the sensor incorporates a thin layer of electrically conductive thermoplastic polyurethane (ETPU) within a hyperplastic X60 substrate, enabling rapid customization of geometry without needing molding or secondary assembly. The ETPU contains dispersed carbon black fillers that create a percolated conductive network, whose resistance changes in response to mechanical strain. When wind flows bend the sensor, the induced strain rearranges the conductive pathways at the

microscale, changing particle contact and spacing. This results in a measurable electrical response, with ETPU showing the unusual behaviour of increased conductivity under tensile strain, unlike conductive PLA or graphene PLA, which typically see resistance increase with strain. The ETPU sensor showed a high gauge factor (GF = 20), a usable strain ranges up to 12.5%, and reliable wind speed sensitivity above 3.5 m s^{-1}. Finite element modeling was used to couple wind loading with strain distribution in the conductive layer, and simulations closely matched wind tunnel experiments across different velocities. Compared to traditional mechanical anemometers like cup and vane devices, the printed sensor eliminates moving parts, reduces wear susceptibility, and avoids the bearing friction threshold, while offering a low cost, scalable fabrication process. The lack of delicate thermal elements also makes it more robust than hot wire anemometers, which are prone to fragility and higher power demands. Resistance changes were measured using a simple voltage divider circuit, enabling direct electromechanical transduction without separate strain gauges or embedded wiring, highlighting its potential for low maintenance, customizable, and field deployable environmental sensing.

A triaxial accelerometer was fabricated through single process FDM. In the reported design, Arh and Slavič [52] co printed three functional materials in one uninterrupted build: nonconductive PLA for the rigid housing and beams, a piezoresistive PLA loaded with carbon black for the strain sensitive gauges, and a copper filled PLA for low resistance signal routing. The gauges were positioned at the fixed ends of three orthogonal cantilever beams, each aligned with one of the x, y, and z axes, while short, thick copper PLA traces provided interconnections to external connectors. This integration created a monolithic, self-contained sensor requiring no post assembly wiring or adhesives. The prototype had an overall cube like geometry with dimensions of 35 mm × 35 mm × 35 mm and beam lengths of approximately 25 mm. Dynamic tests with harmonic base excitation showed that the three axes had natural frequencies between 500 and 680 Hz, with flat and stable sensitivity responses in the 20–150 Hz range. Axial sensitivities reached approximately 15.6 mΩ s^2/m (x axis), 16.2 mΩ s^2/m (y axis), and 6.3 mΩ s^2/m (z axis). Cross axis sensitivity was low, generally under 3%, indicating good mechanical and electrical decoupling of the three beams. From the conductive filament perspective, the study demonstrates how combining high resistivity and low resistivity conductive filaments in a single FDM process enables functional separation of sensing and interconnect roles, improving performance without secondary processes such as

applying conductive ink or embedding wires. Reported filament resistivities were approximately 15 Ω.cm for PLA with carbon black and 0.006 Ω.cm for the copper filled PLA used as highly conductive paths. Compared to capacitive designs such as Schouten et al. [53] or Aeby et al. [54], which rely on geometric or anisotropic dielectric coupling, the Arh and Slavič device leverages direct piezoresistive conversion of strain into resistance change, making it suitable for dynamic inertial sensing while preserving the simplicity and reproducibility of a fully printed architecture.

Schouten et al. [53] developed a flexible capacitive force sensor via FDM using multi material printing, a method highly relevant to functional device fabrication with conductive filaments. The electrodes were printed from conductive thermoplastic polyurethane, which combines elasticity with stable electrical conductivity, and the dielectric layer was printed from X60 ultra flexible filament to allow significant deformation under load. In this parallel plate design, applied force decreased plate separation, increasing capacitance in proportion to the load. Testing at 25 kHz and 1 V excitation revealed a capacitance change of approximately 160 fF for a 6.6 N force increase, showing both sensitivity and repeatability. This work also demonstrates how conductive polymers, traditionally used in piezoresistive configurations, can also serve as electrodes in capacitive architectures. By separating conductive and dielectric roles into different printable materials, Schouten et al. avoided mechanical compromise in the sensing layer while maintaining electrical stability. This approach opens pathways for integrating conductive filaments into multi modal sensor systems within a single 3D printed structure. Compared to earlier piezoresistive approaches using conductive PLA [51], [52], the use of conductive TPU in a capacitive design mitigates brittleness issues and resistance drift, offering greater durability for applications involving repeated deformation.

Helou et al. [55] introduced soft mechanical metamaterials capable of performing digital logic operations through deformation controlled conductive pathways. The substrate was cast from urethane rubber using 3D printed molds; surface channels were then filled with a silver TPU conductive ink and connected using embedded copper leads. This approach enabled tunable electromechanical responses in which the conductive phase acted as an embedded network whose electrical connectivity changed predictably under compression or bending. By programming the unit cell geometry, they implemented logic gates such as AND, OR, NOT, NAND, NOR, and XOR without discrete electronic components. Mechanical deformation altered contact states

between conductive struts, directly changing circuit continuity. This deformation induced switching behaviours were built into the metamaterial architecture, allowing mechanical electrical logic operations with high repeatability over multiple cycles and offering potential for integrated sensing and computation within soft robots, wearable devices, and adaptive systems. It also has been seen that polymer composites can serve as active computational elements, though the conductive phase here is a cast silver TPU ink network rather than a commercial filament.

A thin, flexible capacitive force sensor was developed by utilizing the inherent anisotropic electrical properties of FDM printed conductive thermoplastic polyurethane. In this design, Wolterink et al. [56] printed two conductive layers directly on top of each other, with the layer interface serving as the dielectric gap. In conductive FDM prints, high inter layer resistance reduces resistive coupling, making capacitive coupling the main mechanism. When a normal force was applied, the distance between layers decreased, leading to an increase in capacitance. This eliminated the need for a separate dielectric layer, simplifying fabrication. The sensor used commercially available conductive ETPU filament, with each layer printed to a thickness of approximately 0.3 mm. Its flexibility allowed it to conform to curved surfaces, making it suitable for wearable devices or soft robotics. The capacitance–force relationship was nonlinear, influenced by the viscoelastic creep and damping behaviour of ETPU. Despite this limitation, the device demonstrated reproducible performance and durability under repeated loading cycles.

A fully FDM 3D printed capacitive transducer was demonstrated using a combination of flexible and conductive materials. In this design, Aeby et al. [54] employed thermoplastic polyurethane as the dielectric layer and semi rigid carbon-based PLA as the electrically conductive electrodes. Multiple sensor samples were fabricated with varying dielectric thicknesses to investigate performance dependencies. Load testing showed that relative sensitivity was not influenced by dielectric thickness but was instead determined by the Young's modulus and surface area of the electrodes. To verify this observation, four samples with different dielectric thicknesses were tested under identical loading conditions, and all exhibited consistent relative sensitivity. One optimized configuration, using a 2 mm^2 electrode area with a 400 μm dielectric, produced a capacitance change of 857 f. The use of only FDM printed layers for both dielectric and electrodes eliminated the need for additional assembly steps, making this approach suitable for low cost, customizable sensor production. From the conductive filament research perspective, this highlights

how pairing a flexible dielectric with rigid conductive electrodes enables stable capacitive sensing even when geometric parameters such as dielectric thickness are varied.

A soft pressure sensor capable of both flexibility and stretchability was fabricated through multi-material 3D printing. In the reported design, Emon et al. [57] arranged five functional layers: a pressure sensitive layer placed between two conductive electrode layers, all enclosed by insulating top and bottom layers. This layered arrangement produced discrete sensing nodes, which is called taxels, at the points where the orthogonal electrodes intersected. The prototype implemented a 2 × 2 electrode configuration, resulting in four taxels. When manual force was applied to one of these taxels, changes in the electrical output (ΔVout) provided localized pressure detection. The integration of all functional elements in a single multi material print reduced assembly requirements and allowed the sensor to maintain its performance when deformed or stretched. For conductive filaments, the significance lies in demonstrating how electrode networks and sensing layers can be co printed with insulating structures, enabling compact, encapsulated sensor architectures.

2.8 Capacitive sensing

There are several approaches to sense an electrical change in a material. One way is sensing the change in capacitance. A capacitor is a two terminal passive device that stores energy electrostatically. When a potential difference is applied across its plates, equal and opposite charges accumulate, creating an electric field in the dielectric. The capacitance C is defined as the ratio of stored charge Q to applied voltage V:

$$C = \frac{Q}{V} \tag{2.2}$$

For an ideal parallel plate capacitor, capacitance is determined by geometry and material properties:

$$C = \varepsilon_0 \varepsilon_r \frac{A}{d} \tag{2.3}$$

where ε_0 is the vacuum permittivity, ε_r is the relative permittivity of the dielectric, A is the effective plate overlap area, and d is the plate separation. Based on the ideal situation there are two physical variables to change the capacitance. Distance between conductive plate and overlapping area.

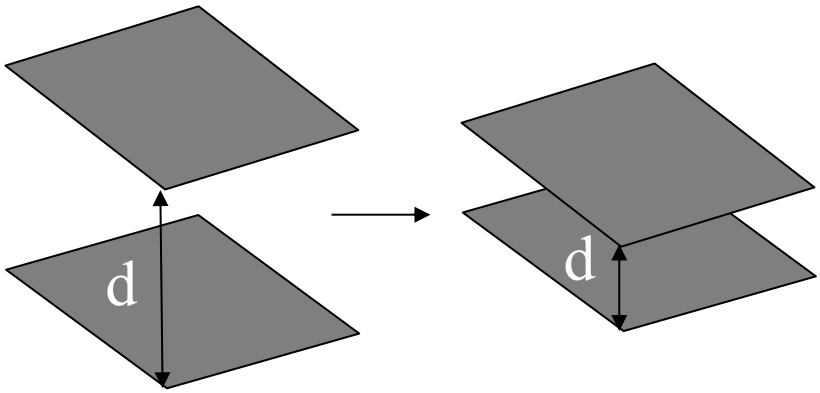

When a capacitor is subjected to an alternating electric field, it no longer behaves as a simple static charge-storage element. Instead, its electrical response is governed by a frequency-dependent capacitive reactance, which opposes changes in voltage. For an ideal capacitor, this reactance is:

$$X_C = \frac{1}{\omega C} \tag{2.4}$$

and the corresponding complex impedance is purely imaginary:

$$Z_C = -\frac{j}{\omega C} \tag{2.5}$$

where $\omega = 2\pi f$ is the angular frequency, and j is the imaginary unit. This relation indicates that current leads voltage by 90 degrees in an ideal capacitor.

Real capacitors do not exhibit this idealised behaviour. Practical devices contain additional resistive and inductive elements that introduce loss, phase distortion, and frequency-dependent deviations. These non-idealities are commonly represented using an equivalent circuit consisting of:

- Equivalent series resistance (ESR): captures resistive losses arising from electrode resistance, dielectric loss, and contact resistance.
- Leakage resistance (RP): models the finite insulation resistance of the dielectric, representing slow charge dissipation through the bulk material.
- Stray inductance (LS): arises from electrode geometry and connection leads, becoming significant at high frequencies.

As a result, the total impedance of a real capacitor contains both real and imaginary contributions. The real part accounts for dissipative phenomena, while the imaginary part continues to represent energy storage. The deviation from ideal behaviour is quantified by the dissipation factor, defined as:

$$D = \tan\delta = \frac{Real\ part\ of\ Z}{Imaginary\ part\ of\ Z} \tag{2.6}$$

In a real capacitor, the real part of the impedance represents the *resistive* component of the system which is the energy that is irreversibly lost as heat due to dielectric loss, leakage pathways, electrode resistance, or conduction through partially percolated filler networks. The imaginary part represents the capacitive component, associated with energy that is reversibly stored and released in the electric field.

In polymer-based dielectrics, and especially in MWCNT filled composites, the dissipation factor is influenced by several mechanisms, including dipolar relaxation, interfacial (Maxwell–Wagner–Sillars) polarization. A high D indicates strong resistive losses and reduced phase shift, while a low D is characteristic of predominantly capacitive behaviour suitable for precise strain measurement. We will cover these in detail in upcoming sections.

2.8.1 Capacitance measurements - time domain measurement

Time domain techniques extract capacitance values from the charging and discharging behaviour of a capacitor. These methods rely on measuring voltage–time relationships rather than impedance or resonance.

RC step response-based capacitance measurement:

When a voltage step *Vs* is applied across a resistor–capacitor circuit, the capacitor voltage follows:

$$V_c\,(\mathrm{t}) \;=\; V_s\,(1 \;-\; e^{-\frac{t}{RC}}) \tag{2.7}$$

At a known resistance *R*, the time t_{th} at which the voltage reaches a threshold *Vth* is:

$$t_{th} = \; -RC\; ln\left(1 - \frac{V_{th}}{V_s}\right) \tag{2.8}$$

Thus, capacitance can be extracted from measured delay times and using RC circuit.

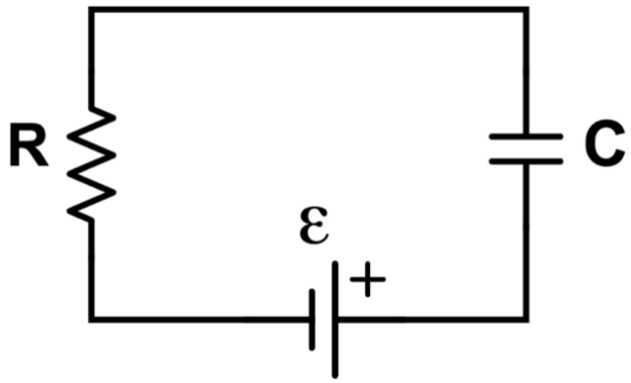

Figure 10: Schematic of RC Circuit

Constant current charging-based capacitance measurement:

For a constant charging current, I, the capacitor voltage rises linearly:

$$V(t) = \frac{I}{C}t \tag{2.9}$$

Rearranging yields:

$$C = \frac{It}{\Delta V} \tag{2.10}$$

- I = constant current applied,
- ΔV = measured voltage increases across the capacitor,
- t = time taken for the capacitor to reach ΔV.

This technique is highly valued because it removes the exponential dependence of the RC method and avoids sensitivity to resistance tolerances. The linearity of the voltage–time response ensures improved accuracy.

The limitations include the requirement for a precise and low noise current source, as well as sensitivity to leakage resistance (Rp) and dielectric absorption, particularly during long charge times. Additionally, noise in the comparator or threshold detector continues to impact timing accuracy. This method is often employed in precision capacitance to time converters and in circuits where relative changes in capacitance need to be monitored with minimal influence from other components.

Relaxation oscillator-based capacitance measurement:

A capacitor can also be measured by embedding it in an oscillatory charge discharge loop. In a basic relaxation oscillator, the capacitor alternately charges and discharges between two voltage thresholds (V_{low} and V_{high}).

The charging follows:

$$V_c(t) = V_{high} - (V_{high} - V_{low})e^{\left(\frac{-t}{RC}\right)} \quad (2.11)$$

The period of oscillation depends linearly on RC. For many common configurations:

$$T = K.R.C \quad (2.12)$$

where K is a dimensionless factor that arises from the logarithmic charge–discharge behaviour of the capacitor between the comparator's upper and lower threshold voltages. Its value is fully determined by the hysteresis ratio of the trigger circuit. The frequency is then:

$$f = \frac{1}{K.R.C} \quad (2.13\_$$

Measuring oscillation frequency provides an indirect estimate of C.

Advantages include providing a continuous oscillating signal that can be easily measured by digital counters. It requires no external current source, only a resistor and comparator, making it suitable for embedded sensing applications where compact circuitry is preferred. However, the limitations involve accuracy being constrained by tolerance of the resistor and the comparator's threshold stability. Non idealities such as leakage and Equivalent Series Resistance (ESR) cause deviations from ideal RC timing, and environmental factors like temperature and supply voltage directly impact frequency stability. Despite these limitations, relaxation oscillators are widely utilized in low cost capacitance measurement integrated circuits, touch sensors, and embedded systems, since high resolution frequency counting can be achieved with microcontrollers.

Unlike time-based approaches that track charging or discharging dynamics, frequency-based methods determine capacitance by exploiting its effect on oscillation frequency or AC impedance. These techniques are typically more precise, less sensitive to drift in thresholds, and allow characterization of dielectric losses

2.8.2 Capacitance measurements – resonance/frequency-based measurement

Resonance based capacitive sensing is one of the most widely employed methods for detecting physical quantities such as displacement, strain, or pressure, as it offers high sensitivity,

mechanical simplicity. Traditional capacitance measurement techniques, such as RC time domain methods, rely on charging and discharging dynamics and are often limited by threshold drift, noise, and temperature sensitivity. In contrast, resonance based capacitive sensing determines capacitance indirectly, by embedding the sensing capacitor into a resonant circuit and tracking shifts in its natural oscillation frequency. This approach provides superior resolution, stability, and immunity to environmental interference, making it particularly suitable for the precise measurement of small capacitance changes.

An LC circuit, composed of an inductor (L) and a capacitor (C), forms a resonant system that stores and exchanges energy between the electric field of the capacitor and the magnetic field of the inductor. The system oscillates naturally at its resonant frequency, given by:

$$f_0 = \frac{\omega_0}{2\pi} = \frac{1}{2\pi\sqrt{LC}} \tag{2.14}$$

At resonance, the inductive reactance ($X_L = \omega L$) and capacitive reactance ($X_C = \frac{1}{\omega C}$) are equal in magnitude and opposite in phase. The impedance of the circuit is therefore minimized, allowing efficient energy exchange between the electric and magnetic domains.

If the capacitance of the sensor changes in response to an external stimulus, such as mechanical strain, pressure, or deformation, the resonant frequency shifts accordingly. For small variations in C, the fractional change in frequency can be expressed as:

$$\frac{\Delta f}{f_0} \sim -\frac{1}{2}\frac{\Delta C}{C} \tag{2.15}$$

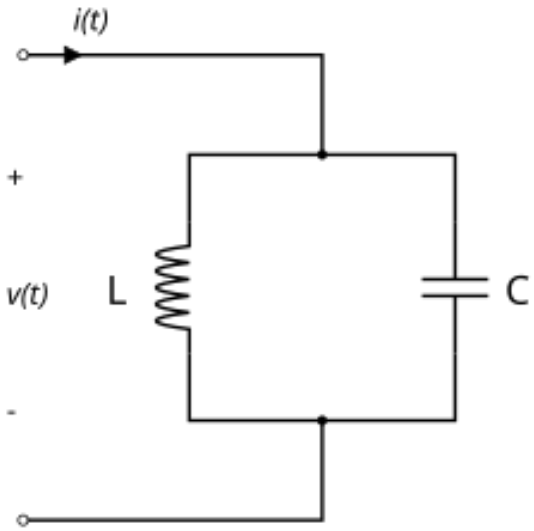

Figure 11: Schematic of LC circuit.

This inverse relationship implies that an increase in capacitance leads to a proportional decrease in resonant frequency. Capacitance can be measured by:

$$C = \frac{1}{4\pi^2 f^2 L} \tag{2.16}$$

L = inductance of the inductor

f = resonant frequency of the circuit

The Texas Instruments FDC2214 Evaluation Module (FDC2214EVM) used in this study operates precisely on the principle of resonance based capacitive sensing. The module incorporates a high frequency LC oscillator in which the external sensor capacitor, here, the 3D printed sensor is connected in parallel with an integrated inductor to form a resonant tank circuit. Variations in the sensor's capacitance, caused by deformation or strain, alter the LC circuit's resonant frequency.

2.9 Dielectric relaxation

Materials that respond to an applied electric field mainly through temporary charge displacement rather than continuous charge flow (DC conductance) are typically called insulators and fall under

the category of dielectrics. Most polymeric materials are considered dielectrics under standard usage conditions.

The investigation into the electrical response of polymeric materials serves three primary purposes. First, since polymers are considered for use as dielectric materials, understanding their electrical properties is essential. Second, dielectric measurements provide a practical and effective means to analyze the time dependent behaviour of these materials, often revealing relaxation phenomena that occur within the same temperature and time ranges as mechanical relaxations, driven by similar molecular mechanisms. Lastly, interpreting dielectric data to determine molecular parameters tends to be more straightforward than analyzing mechanical measurements, making it a valuable approach for studying polymer dynamics [58].

At the heart of AC impedance measurements lies the dielectric permittivity, a fundamental property that describes a material's ability to store electrical energy in response to an applied electric field.

Dielectric permittivity is denoted by (ε) , and it is typically expressed relative to the vacuum permittivity ε_0 (where $\varepsilon_0 = 8.85\,.10^{-12}F/m$) as the relative permittivity $\varepsilon_r = \frac{\varepsilon}{\varepsilon_0}$, also known as the dielectric constant. However, dielectric permittivity is not a static constant; it exhibits frequency dependence, particularly in complex materials like polymer composites.

Dielectric relaxation refers to the time dependent response of a material's polarization to an applied electric field, particularly when the field oscillates (as in AC impedance measurements). When an electric field is applied to a dielectric material, the material polarizes by aligning dipoles, displacing charges, or accumulating charges at interfaces. These polarization mechanisms require a finite time to respond due to the dynamics of molecular or charge interactions. When the frequency of the applied field ($\omega = 2\pi f$) increases, some mechanisms cannot keep pace, leading to a decrease in the material's ability to store charge, which can be seen by decrease in $\varepsilon_{r(\omega)}$ and an increase in energy losses.

Relaxation is characterized by a relaxation time (τ), which is the time constant associated with how quickly the polarization mechanisms can align with or respond to the changing electric field.

At frequencies where the condition $\omega\tau \sim 1$ is met, a polarization mechanism reaches its characteristic response time. In this regime, the dipoles or interfacial charges can no longer follow the oscillating field completely, which produces a maximum in the loss permittivity, accompanied by a reduction in the storage permittivity. This behaviour is a fundamental feature of dielectric relaxation and provides the basis for interpreting frequency-dependent permittivity in polymer materials and nanocomposites.

The observed frequency dispersion arises from several polarization mechanisms, each active over different characteristic frequency ranges. At the highest frequencies, typically above about 10^{13} Hz, electronic polarization occurs due to the rapid displacement of electron clouds relative to atomic nuclei. In the range of approximately 10^{10} to 10^{13} Hz, ionic or atomic polarization, arising from the relative motion of positive and negative ions in the lattice becomes relevant. At intermediate frequencies, generally between 10^3 and 10^{10} Hz, dipolar polarization dominates as permanent dipoles attempt to align with the applied field; this process is strongly temperature-dependent and relaxes at its own characteristic time [58], [59].

At low frequencies, typically below 10^3 Hz, the dielectric response of heterogeneous polymer systems is dominated by Maxwell–Wagner–Sillars (MWS) polarization [59]. This mechanism results from charge accumulation at interfaces between phases with different conductivities or permittivity such as the polymer matrix and conductive nanofillers and produces a pronounced increase in both storage and loss permittivity in the low-frequency region. In polymer nanocomposites containing fillers like carbon nanotubes, the large interfacial area and strong contrast in electrical properties intensify this effect, making MWS polarization the primary source of low-frequency dispersion.

To capture this behaviour, the complex permittivity $\varepsilon^*(\omega)$ is introduced:

$$\varepsilon^*(\omega) = \varepsilon'(\omega) - j\varepsilon''(\omega) \qquad 2.17$$

- $\varepsilon'(\omega)$: The real part, representing the storage component (energy stored per cycle).
- $\varepsilon''(\omega)$: The imaginary part, representing the loss component (energy dissipated as heat).

The loss tangent is then:

$$\tan \delta(\omega) = \frac{\varepsilon''(\omega)}{\varepsilon'(\omega)} \quad 2.18$$

Dielectric spectroscopy, enabled by AC impedance measurements, involves sweeping ω to map $\varepsilon_{r(\omega)} = \varepsilon'(\omega)$, and tan δ(ω). Once the complex permittivity is defined, the next step is to describe how a material with a specific polarization mechanism responds to an alternating field. The simplest and most fundamental model is the Debye relaxation, which represents an ideal ensemble of non-interacting dipoles characterized by a single relaxation time. In this model, the complex permittivity follows:

$$\varepsilon^*(\omega) = \varepsilon_\infty + \frac{\varepsilon_s - \varepsilon_\infty}{1 + j\omega\tau} \quad (2.19)$$

where:

- ε_s: Static (low frequency) permittivity.
- ε_∞: High frequency permittivity (after relaxation).
- τ: Relaxation time constant, related to the frequency at which tan δ peaks ($f_{max} = \frac{1}{2\pi\tau}$)

Separating real and imaginary parts:

$$\varepsilon'(\omega) = \varepsilon_\infty + \frac{\varepsilon_s - \varepsilon_\infty}{1 + (\omega\tau)^2} \quad (2.20)$$

$$\varepsilon''(\omega) = \frac{(\varepsilon_s - \varepsilon_\infty)(\omega\tau)}{1 + (\omega\tau)^2} \quad (2.21)$$

Relaxation processes are characterized by a peak in the imaginary part (ε′′) and a step-like decrease of the real part (ε′) of the complex dielectric function. While the Debye model describes an ideal system with a single relaxation time, real polymer systems and polymer–nanofiller composites often exhibit broader and asymmetric relaxation spectra due to molecular heterogeneity and interfacial effects. To account for these deviations, the Havriliak–Negami (HN)[60] model extends

the Debye formulation by introducing two empirical shape parameters. This generalized expression accommodates both the asymmetric broadening, and the distribution of relaxation times commonly observed in polymers and complex dielectric materials. Originally developed to model dielectric responses in polymer systems, the Havriliak–Negami function has become the most widely used empirical model for fitting broadband dielectric spectra. The HN formulation expresses the complex permittivity as:

$$\hat{\varepsilon}(\omega) = \varepsilon_\infty + \frac{\varepsilon_s - \varepsilon_\infty}{(1 + (i\omega\tau)^\alpha)^\beta} \tag{2.22}$$

Whereas before $\varepsilon_\infty$is the permittivity at the high frequency limit, ε_s is the static, low frequency permittivity, and $\tau$is the relaxation time of the medium. The exponents α, and β describe the asymmetry and broadness of the corresponding spectra.

In the Havriliak-Negami relaxation model, the storage (Eq 2.23) and loss permittivity (Eq 2.24) can be calculated as:

$$\varepsilon'(\omega) = \varepsilon_\infty + (\varepsilon_s - \varepsilon_\infty)(1 + 2(\omega\tau)^\alpha \cos\left(\frac{\pi\alpha}{2}\right) + (\omega\tau)^{2\alpha})^{\frac{-\beta}{2}} \cos(\beta\phi) \tag{2.23}$$

and

$$\varepsilon''(\omega) = (\varepsilon_s - \varepsilon_\infty)\left(1 + 2(\omega\tau)^\alpha \cos\left(\frac{\pi\alpha}{2}\right) + (\omega\tau)^{2\alpha}\right)^{\frac{-\beta}{2}} \sin(\beta\phi) \tag{2.24}$$

with

$$\phi = \arctan\left(\frac{(\omega\tau)^\alpha \sin\left(\frac{\pi\alpha}{2}\right)}{1 + (\omega\tau)^\alpha \cos\left(\frac{\pi\alpha}{2}\right)}\right) \tag{2.25}$$

The model reduces to Debye when $\alpha = \beta = 1$, to Cole– Cole when $0 < \alpha < 1$ and $\beta = 1$, and to Cole–Davidson when $\alpha = 1$ and $0 < \beta < 1$. The Havriliak–Negami formulation, therefore,

provides the most general and accurate empirical representation for complex dielectric relaxation in polymer composites.

The complex dielectric function $\varepsilon^*(\omega)$ depends on both angular frequency and temperature, and this dependence originates from several intertwined processes. These include microscopic fluctuations in molecular dipoles, known as rotational diffusion, as well as the movement of mobile charge carriers, such as electrons, holes, or ions, through translational diffusion. Additionally, charge separation at interfaces leads to additional polarization effects, which contribute to the overall behavior of the dielectric function. The latter may occur at inner dielectric boundary layers (MWS) on a mesoscopic scale and/or at the external electrodes in contact with the sample (electrode polarization) on a macroscopic scale. Its contribution to dielectric loss can be orders of magnitude greater than that caused by molecular fluctuations. Each relaxation model introduces specific frequency- and temperature-dependent features into the dielectric response, and fitting these models allows the individual contributions to $\varepsilon'(\omega)$ and $\varepsilon''(\omega)$ to be quantified. Alternative representations such as the complex conductivity $\sigma^*(\omega)$ or the electric modulus $M^*(\omega) = 1/\varepsilon^*(\omega)$ are often employed to reveal relaxation processes that may be obscured in the permittivity formalism.

Chapter 3: Investigating the effect of printing parameters on conductivity

In this chapter, the effects of 3D printing parameters on the final conductivity will be investigated.

3.1 Introduction

As discussed before, there are several printing parameters that can affect the physical and electrical properties of the printed part. In this section, we investigate how these parameters can affect the conductivity of the printed part. We investigated 5 printing parameters: nozzle temperature, printing speed, orientation angle, infill density, and layer height.

The nozzle temperature determines the viscosity of the molten filament and directly affects MWCNT dispersion and interlayer fusion. At lower temperatures, incomplete melting leads to poor wetting between adjacent filaments and weak layer adhesion, resulting in increased voids and discontinuities in the conductive network. At excessively high temperatures, however, thermal degradation of the polymer matrix or localized MWCNT agglomeration can occur, reducing uniformity and stability. An optimal range allows sufficient chain mobility and nanotube rearrangement to promote percolation pathways while maintaining print dimensional accuracy.

Printing speed controls the residence time of the molten composite in the hot zone and influences filament cooling and bonding. Lower speeds promote better interlayer diffusion and MWCNT alignment continuity but may increase material shrinkage and thermal stress. Higher speeds reduce the time available for fusion and can trap micro voids at interfaces, increasing electrical resistance. Because MWCNTs tend to align along the direction of flow, the balance between shear rate and deposition rate defines the anisotropy of the resulting conductive pathways.

Infill percentage determines the internal density of the printed structure. Lower infill values create internal voids and discontinuities that interrupt conductive networks, leading to lower effective conductivity. Higher infill densities enhance inter filament contact, reducing resistance and improving charge transport. However, beyond a certain threshold, increasing infill may have diminishing returns, as resistivity becomes dominated by the intrinsic properties of the composite rather than geometry.

Layer height defines the vertical resolution and the thickness of each deposited layer. Smaller layer heights yield smoother surfaces and more homogeneous interfaces between layers, improving interlayer fusion and reducing insulating gaps. Larger layer heights accelerate printing but can lead

to incomplete bonding and increased interfacial voids, which act as barriers to electron transport. Because MWCNT connectivity often depends on the contact area between adjacent layers, optimizing layer height is critical to achieve consistent through thickness conductivity.

The orientation angle (Figure 12), also known as the raster or infill angle, refers to the direction of deposited filaments relative to the current flow during electrical measurement. In 3D printed MWCNT–polyester composites, this parameter significantly influences the formation and continuity of conductive networks. When the filaments are aligned parallel to the current direction (0°), electrons travel along continuous MWCNT rich paths with minimal interfacial resistance, resulting in higher conductivity. As the orientation angle increases (e.g., 45° or 90°), the current must traverse multiple filament junctions and polymer interfaces, where limited fusion and voids increase tunneling resistance. Consequently, the electrical conductivity decreases with increasing orientation angle, producing a measurable anisotropy between in plane and cross plane conduction.

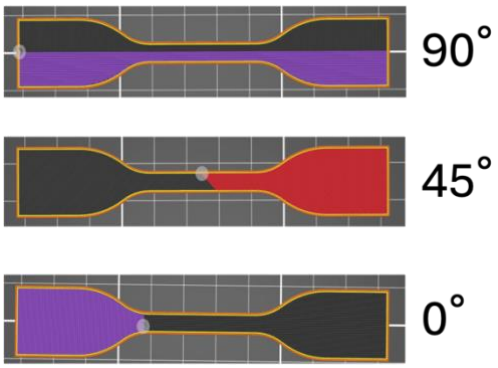

Figure 12: 3D printing infill orientation angle

3.2. Materials and methods

The conductive filaments used throughout this research were provided by the group of Misiak et al. [3], developed the conductive filaments used in this research: hot-melt adhesive (HMA) copolymers reinforced with multi-walled carbon nanotubes (MWCNTs), combining flexibility with electrical conductivity rarely achieved in printable feedstocks. These materials are exceptional because they combine the printability and elasticity of hot melt copolymers with the electrical conductivity of carbon nanotube networks, achieving conductivity levels rarely obtained in flexible FDM feedstocks.

Table 1: Polymer composites (ABR, G1839_10, and G2A_10) description

Filament code	Matrix polymer	MWCNT content(wt.%)	Description
ABR	copolyester (coPE)	5	Flexible conductive coPE adhesive with moderate MWCNT loading optimized balance of elasticity and conductivity
G1839_10	copolyester (coPE)	10	Highly conductive coPE composite with dense MWCNT network beyond percolation threshold
G2A_10	copolyamide (coPA)	10	Conductive coPA-based adhesive providing higher polarity and mechanical rigidity

Filaments were fabricated through a two-step melt compounding and extrusion process specifically optimized to ensure homogeneous nanotube dispersion and high conductivity while retaining flexibility:

1. Masterbatch formation – Multi walled carbon nanotubes (NC7000, Nanocyl, Belgium; diameter ~ 9.5 nm, length ~ 1.5 μm, carbon purity ~ 90 %) were incorporated into a copolyester hot melt adhesive (supplied by EMS-CHEMIE AG, Switzerland) using a semi-industrial co rotating twin screw extruder to produce a masterbatch containing 10 wt. % MWCNTs. This extrusion step applied strong shear forces to disperse nanotube agglomerates and create a preliminary conductive network within the polymer.

2. Dilution and re-extrusion – The 10 wt.% masterbatch were then diluted with neat polymer pellets to obtain lower MWCNT concentrations (1–9 wt.%). The diluted mixtures were again extruded using a HAAKE MiniLab conical twin screw mini extruder (Thermo Fisher Scientific, USA), which provided additional shear mixing and torque due to its variable diameter screws.

The resulting nanocomposite pellets were extruded into filaments of 1.75 ± 0.1 mm diameter, suitable for fused filament fabrication (FFF). All this information was obtained from Misiak et al.[3]'s paper, who collaborated with us on this research by providing access to the produced filament.

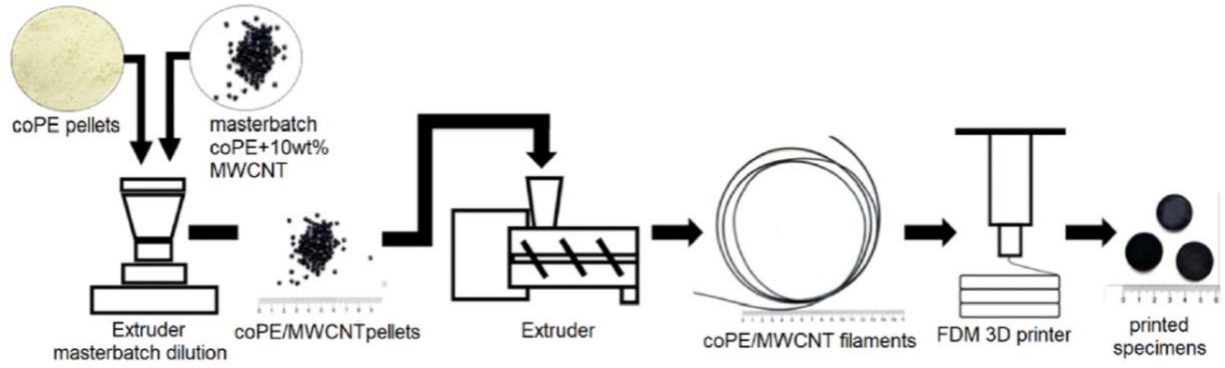

Figure 13: Flow chart of filament manufacturing process from copolyester adhesive, and MWCNT

Typical processing conditions were:

- Extrusion temperature: 150–175 °C (depending on MWCNT content)
- Screw speed: ~ 40–45 rpm
- Torque: 15–19 N cm

All filaments were smooth, flexible, and visually defect free. Microscopy confirmed that the MWCNT agglomerate size after the second extrusion was typically below 30 μm, and no internal porosity was detected by X-ray micro-CT analysis.[3] The combination of low percolation threshold (< 1 wt.%) and strong interfacial bonding between the MWCNT network and the hot melt matrix makes these filaments distinct among conductive composites. Even at high nanotube concentrations, they retain elasticity and can be printed into bendable structures capable of conducting current or serving as sensor substrates.

To investigate the effect of printing parameters, we printed type IV dogbone specimens conforming to ASTM D638 (as depicted in Figure 15) in different printing conditions using Prusa MK3S+ equipped with multi-material unit (MMU) and measured the resistivity using the four-probe method (Figure 14). The four-probe method eliminates contact resistance and provides accurate bulk resistivity compared to two-probe method. Four collinear electrodes are placed along the sample surface: the outer pair supplies a constant current (I), and the inner pair measures the potential difference (V) between two points unaffected by contact voltage drops. Because the voltage is sensed with a high impedance instrument, virtually no current flows through the voltage leads, and the measured potential corresponds only to the sample's intrinsic resistance.

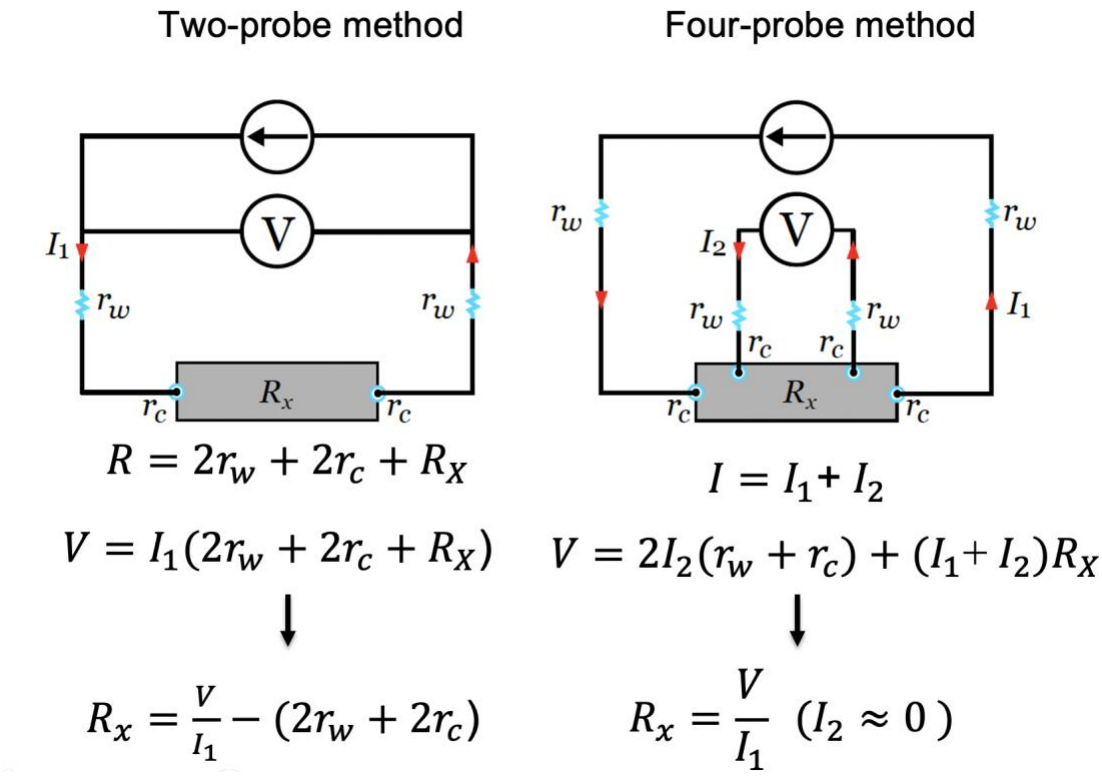

Figure 14: Two-probe and four-probe method for calculating resistivity.

As shown in Figure 14, the four-probe configuration eliminates the influence of contact and lead resistance, allowing a more accurate determination of the material's intrinsic resistivity. Because the voltmeter has a very high input impedance, the current flowing through the voltage-sensing terminals is effectively zero, ensuring that the measured voltage drop reflects only the sample's bulk behaviour.

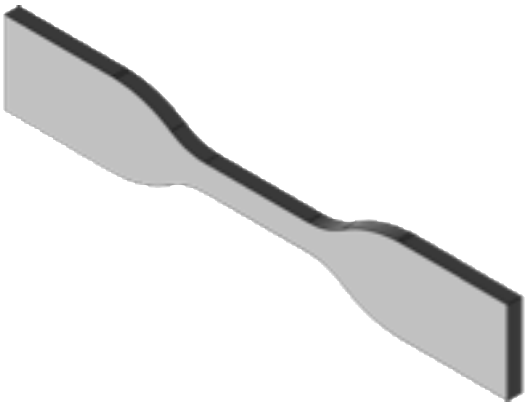

Figure 15: ASTM D638 type IV specimen.

A Rigol *DM3058ME* Digital multimeter was used to measure resistivity, and the outer and inner cables were attached as in Figure 16.

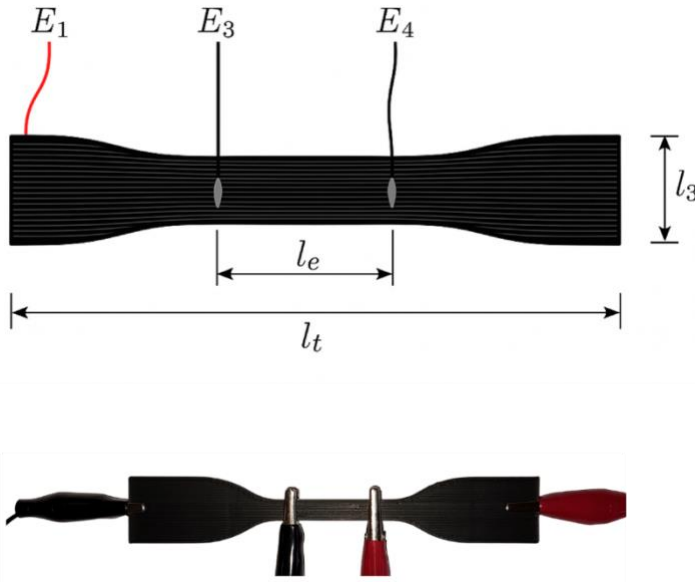

Figure 16: Four-probe connection on printed sample.

Resistivity is calculated based on:

$$\rho = \frac{R_x\, A}{l_e}$$

where:

$A = Cross\ sectional\ area$: $l_{2(thickness)}.l_3(cm^2)$

ρ = Resistivity ($\Omega.cm$)

l_e = length between internal electrodes (cm)

3.3 Results and discussion

3.3.1 Effect of layer height on electrical resistivity

Figure 17, and 18 summarizes the influence of layer height on electrical resistivity for both copolyamide with 10 wt.% of MWCNT (G2A_10) and copolyester 5 wt.% MWCNT(ABR) composites printed under various nozzle temperature, orientation combinations.

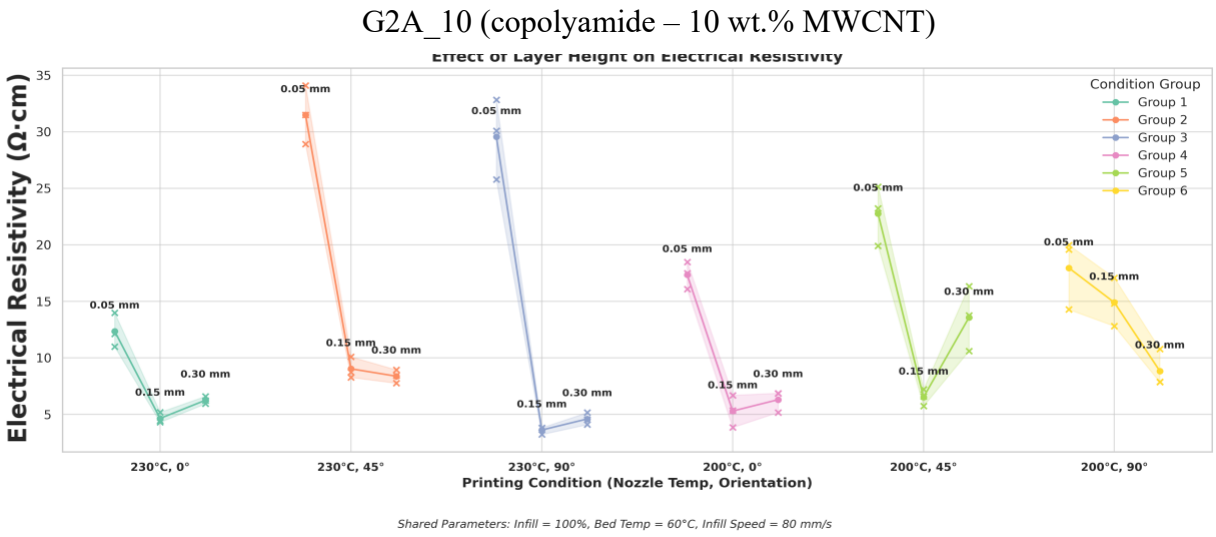

Figure 17: Effect of layer height on electrical resistivity of 3D-printed G2A_10 (copolyamide, 10 wt.% MWCNT) at two nozzle temperatures (200°C, 230°C) and three raster orientations (0°, 45°, 90°).

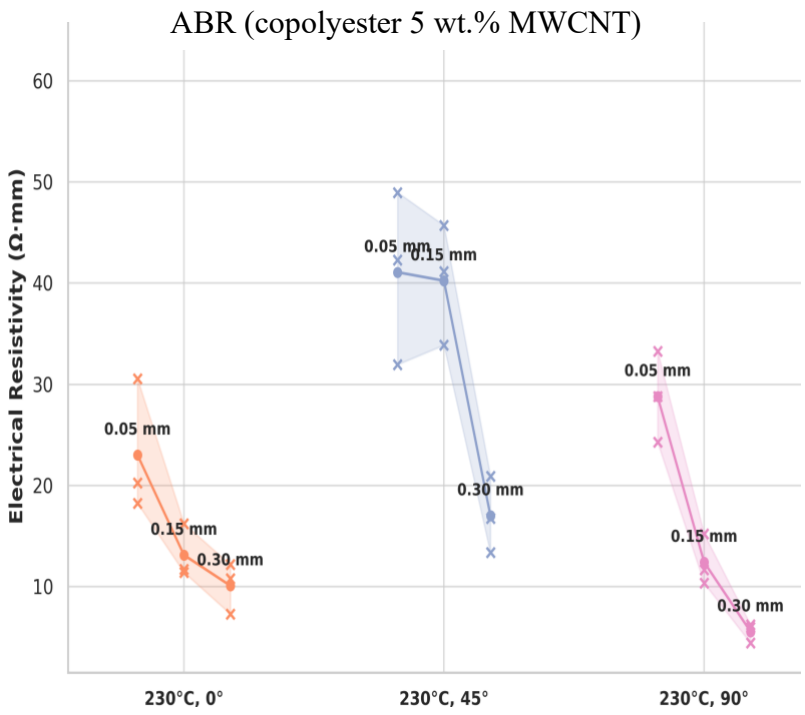

Figure 18: Electrical resistivity of 3D printed ABR as a function of layer height at 230 °C for three raster orientations (0°, 45°, and 90°)

It can be seen in Figures 17 and 18 that across all conditions, resistivity decreases systematically with increasing layer height, demonstrating that thickness strongly influences the formation of continuous conductive pathways. ABR_5 shows the same general tendency, although the magnitude of the change is smaller due to its lower MWCNT content and softer matrix, which allows more intimate MWCNT–MWCNT contact even at thinner layers.

This behaviour is attributed to the microstructural consequences of layer thickness. Because larger layer heights require fewer deposited layers, the number of interlayer junctions, each of which introduces an interfacial electrical barrier, is reduced. As a result, charge transport occurs through longer uninterrupted MWCNT rich domains, lowering resistivity. In contrast, thin layers contain more stacked interfaces, forcing current to traverse multiple MWCNT poor interfacial regions that introduce additional tunneling resistance. This interpretation aligns with results from Pentek et al. [27], who demonstrated that thin layers increase resistance due to numerous poorly fused interfaces, and with Dembek et al. [28], who observed that very small layer heights (<0.20 mm) promote void formation and unstable extrusion, leading to higher resistivity.

Likewise, Glogowsky et al. [29] reported that thicker layers enable more stable CNT bridging by reducing shear-induced disruption and promoting slower cooling, both of which enhance percolation. These effects are clearest under 230 °C, 45°, where G2A_10 printed at 0.05 mm exhibits more than a 3× higher resistivity than at 0.30 mm. For ABR_5, the effect remains directionally similar but less pronounced, consistent with a weaker and more compliant matrix that enables more MWCNT rearrangement even at small layer heights.

Collectively, these results confirm that layer height is a key determinant of electrical performance, and that larger layer heights (~0.30 mm) are preferable when maximizing conductivity, provided dimensional precision remains acceptable. Collectively, these results agree with the established literature and confirm that layer height is a primary determinant of electrical performance in conductive FDM composites, where larger layer heights (~0.30 mm) promote stronger percolated networks and reduced resistivity.

3.3.2 Effect of print orientation on electrical resistivity

Print orientation (raster angle) had a measurable influence on electrical resistivity. At 230 °C / 0.05 mm, specimens printed with filaments aligned parallel to the measurement direction (0°) showed the lowest resistivity (Figure 19). Rotating the raster to 45° increased resistivity noticeably, while 90° produced intermediate values. This trend reflects the formation of more continuous MWCNT-rich pathways when filaments are aligned with the probing direction, whereas off-axis patterns introduce additional interlayer connections. This behaviour is fully consistent with prior FDM composite studies: Pentek et al.[27] showed that conductivity along the print direction (X-axis-90°) is two orders of magnitude higher than other orientations, and Glogowsky et al. [29]similarly reported that 90° infill provides the lowest resistivity while 45° patterns introduce disruptive junctions that elevate resistance.

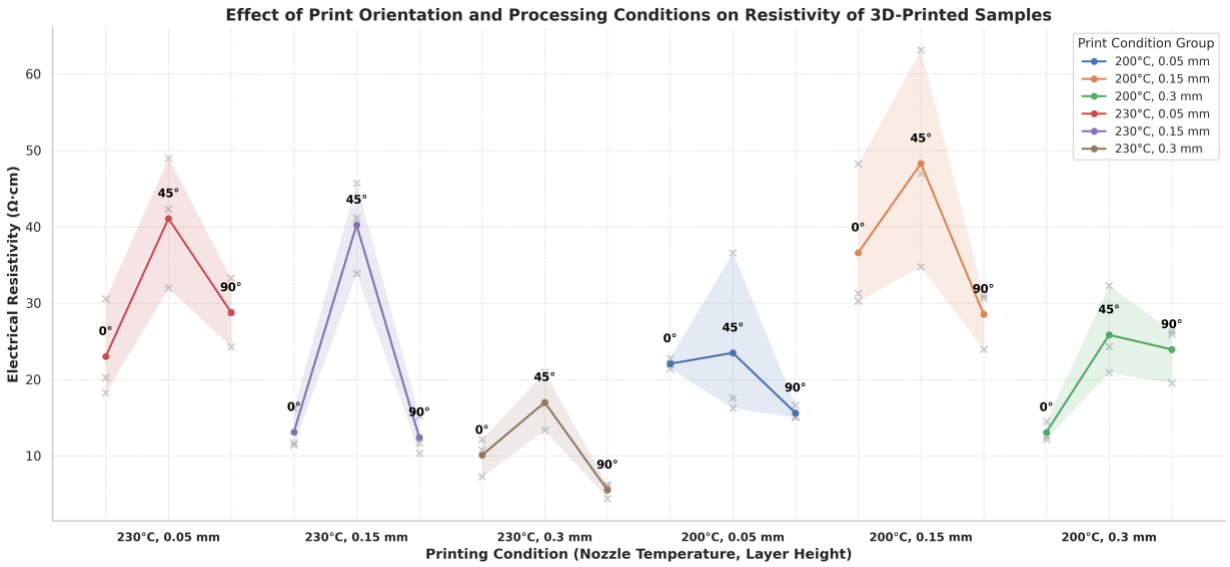

Figure 19: Effect of print orientation on the electrical resistivity of 3D-printed copolyester/MWCNT samples

At 230 °C / 0.15 mm, the same ordering (0° < 90° < 45°) was observed, though differences between angles were smaller. Increasing the layer height to 0.30 mm further reduced the orientation effect, likely due to fewer interlayer boundaries, which helps preserve conductive pathways regardless of raster direction. A similar pattern was observed at 200 °C, although absolute resistivity increased across all orientations. This is expected, as reduced melt mobility at lower temperature restricts MWCNT realignment, amplifying the resistive penalty associated with any misalignment from the 0° direction. The orientation effect again decreased with larger layer heights. Overall, 0° consistently provided the best conductivity, while 45° produced the highest resistivity under nearly all conditions. The effect is strongest at small layer heights and diminishes as layers thicken.

3.3.3 Effect of printing speed on electrical resistivity

Printing speed exhibited a non-monotonic influence on electrical resistivity for both G2A_10 and ABR_5 composites, as shown in Figures 20 and 21. Instead, the intermediate speed of approximately 80 mm s^{-1} consistently produced the highest resistivity, while both lower speeds (40 mm s^{-1}) and the highest speed tested (around 120 mm s^{-1}) resulted in lower values that were similar in magnitude.

At low speeds, a reduced deposition rate likely enables better filament wetting and more effective interdiffusion at the interfaces. This extended residence time under the nozzle also allows MWCNTs more freedom to reorganize within the melt, forming denser pathways.[29], [32] These effects are consistent with the lower resistivity observed in this region.

The increase in resistivity at the mid-range speed appears to represent a transition region where neither fusion nor shear-alignment is fully favourable. At around 80 mm s^{-1}, the melt may not remain hot and mobile long enough to complete interlayer fusion, yet the shear rate may already be high enough to disrupt MWCNT clusters without providing sufficient realignment. As a result, micro voids, incomplete bonding, and disrupted percolation pathways are more likely to persist, potentially explaining the elevated resistivity.

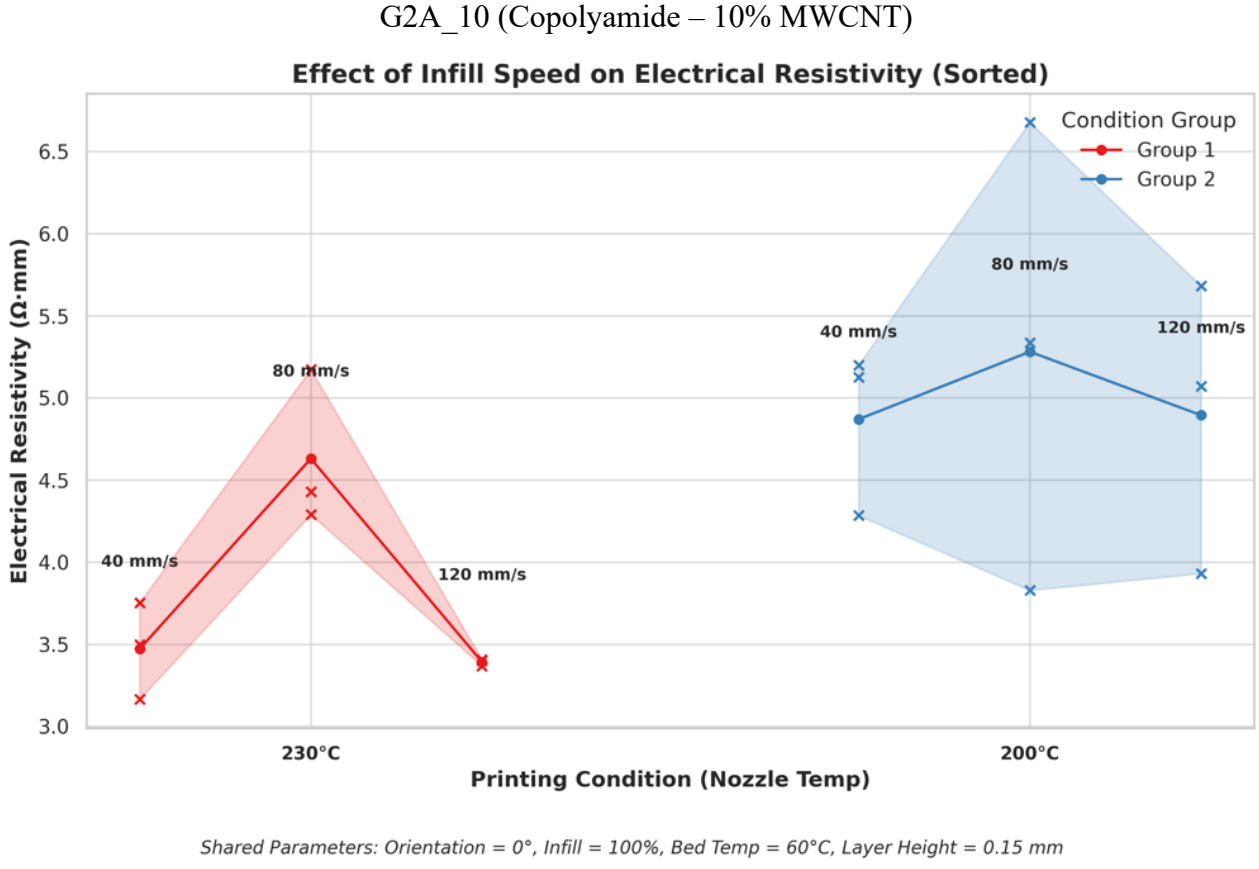

Figure 20: Effect of printing (infill) speed on electrical resistivity of 3D printed G2A_10.

ABR (copolyester – 5 wt.% MWCNT)

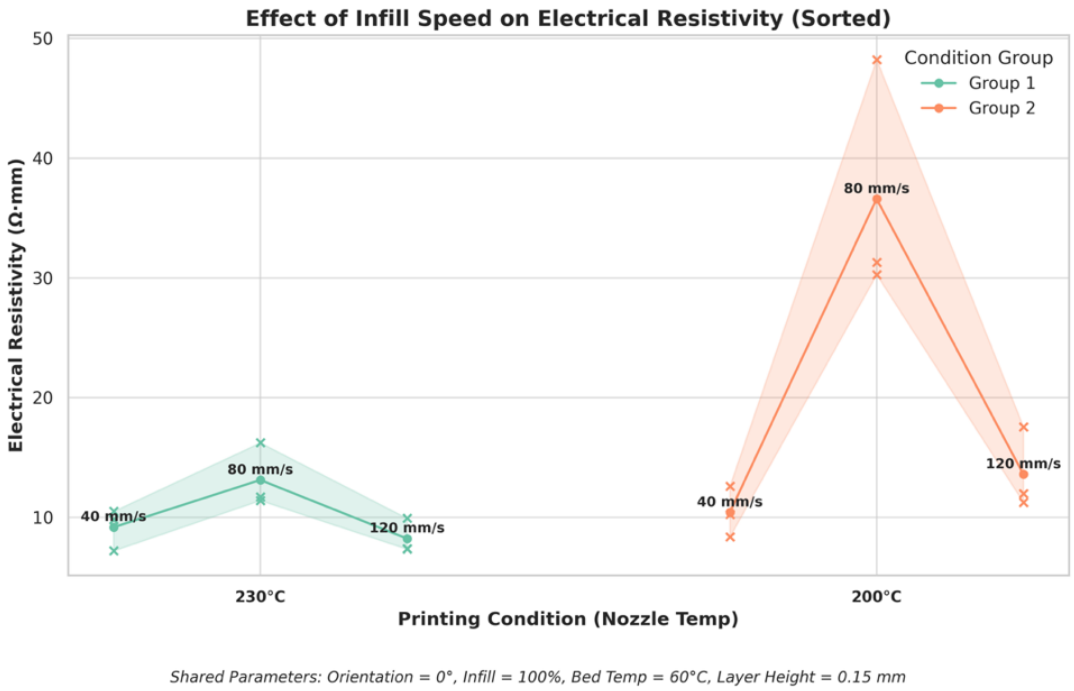

Figure 21: Effect of printing (infill) speed on electrical resistivity of 3D printed ABR.

At higher speeds near 120 mm s^{-1}, resistivity decreases again. A possible, though unconfirmed, explanation is that the high shear rate may promote some degree of nanotube orientation along the deposition direction, partially compensating for reduced fusion time. Without direct morphological evidence, this remains speculative, but the consistent drop in resistivity at the highest speed suggests that shear-induced alignment may contribute to network stabilization under rapid deposition.

This behaviour does not match the trends seen in comparable studies. Glogowsky et al.[29] reported that resistivity in TPU15CNT, TC8OEX, and Eel remained largely invariant across typical speeds, and Paz et al.[32] observed a monotonic increase in resistivity as printing speed increased in ABS/GNP composites. Neither study reported a resistivity maximum at intermediate speeds. This suggests that the behaviour seen in the present composites may arise from unique interactions between polymer rheology, cooling profile, and filler clustering at high MWCNT loading. Further investigation, such as microscopic imaging or rheological monitoring after extrusion, would be required to determine whether these hypotheses reflect the true mechanism.

Overall, while printing speed clearly affects the electrical performance of these composites, the underlying cause of the observed non-monotonic behaviour remains uncertain and may be specific to the microstructure and rheology of these materials.

3.3.4 Effect of nozzle temperature on electrical resistivity

In both ABR (5 wt.% MWCNT) and G2A_10 (10 wt.% MWCNT) (Figure 22, and 23), increasing the nozzle temperature from 200 °C to 230 °C reduces electrical resistivity at layer heights of 0.15 mm and 0.30 mm. The improvement is attributed to lower melt viscosity at higher temperatures, which enhances polymer–MWCNT wetting, promotes more uniform filler redistribution, and facilitates stronger interlayer fusion. These conditions support the formation of longer and less interrupted conductive pathways, consistent with the behaviour expected in highly loaded percolated networks. Similar temperature-assisted conductivity enhancement has been documented for other conductive FDM composites: Dembek et al[28]. reported improved CNT–PLA conductivity at higher nozzle temperatures due to reduced viscosity and improved bonding; Iffelsberger et al. [31] observed the same effect in graphite-reinforced PLA; and Paz et al. found analogous trends in ABS/graphene-nanoplatelet systems. The agreement between these studies and the present results supports the interpretation that sufficient bead volume allows the benefits of higher melt temperature to fully develop.

ABR (copolyester 5 wt.% MWCNT)

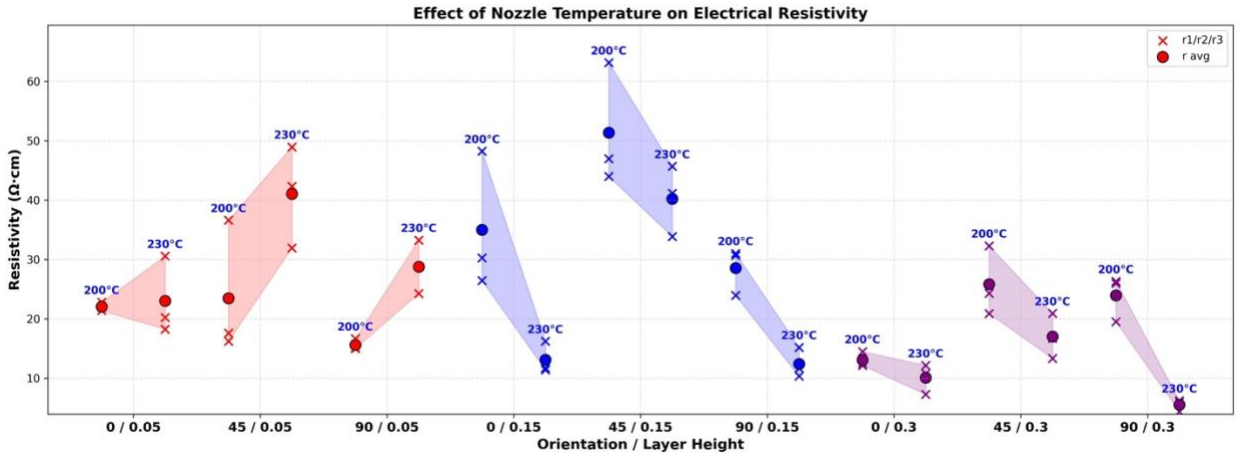

Figure 222: Effect of nozzle temperature on electrical resistivity of 3D printed ABR.

At the smallest layer height (0.05 mm), the response diverges from this behaviour. In both materials, resistivity remains high or increases slightly at 230 °C. None of the cited studies investigated nozzle-temperature effects in this extreme geometric regime, where the deposited filament has a very high surface-area-to-volume ratio. Under such conditions, solidification occurs almost immediately after extrusion, limiting the time available for MWCNT rearrangement and suppressing the temperature-driven improvements seen at larger bead volumes. The resulting microstructure is dominated by shear-aligned, rapidly frozen filaments with limited lateral bridging, which constrains the development of a well-connected percolation network despite the higher nozzle temperature. This behaviour indicates that nozzle temperature interacts strongly with layer height, and that trends observed at conventional layer heights cannot be directly extrapolated to ultra-thin deposition. Table 2 provides a summary of how each parameter affected the conductivity.

G2A_10 (copolyamide – 10 wt.% MWCNT)

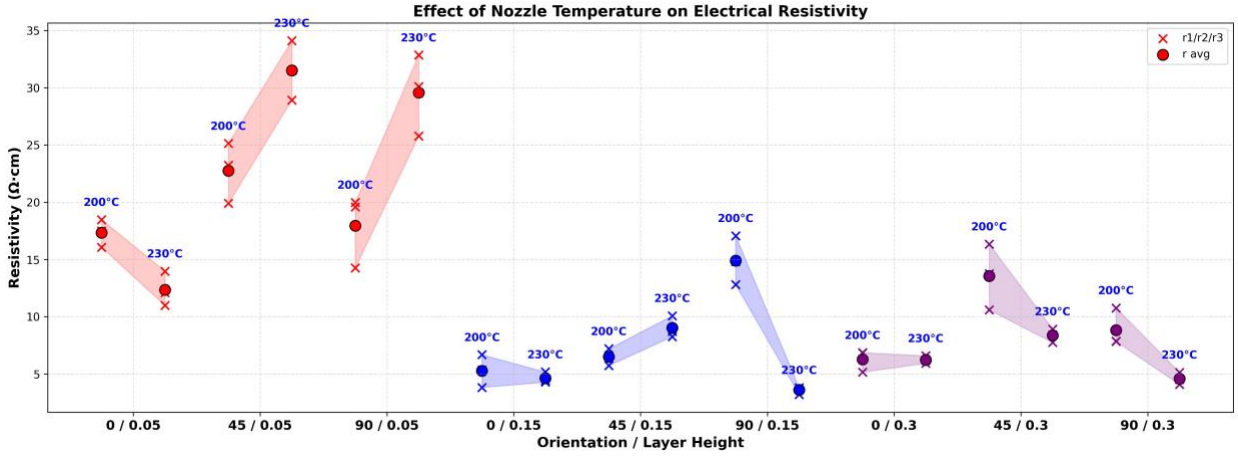

Figure 23: Effect of nozzle temperature on electrical resistivity of 3D printed G2A_10.

Table 2: Effect of each printing parameter on conductivity

Parameter	**Trend observed in this study**
Layer Height	Resistivity decreases as layer height increases (0.05 mm → highest ρ; 0.30 mm → lowest ρ).
Print Orientation	0° → lowest ρ, 45° → highest ρ, 90° → intermediate.
Printing Speed	Local maximum at ~80 mm/s; lower ρ at both slower (40–60 mm/s) and faster (~120 mm/s) speeds.
Nozzle Temperature	Higher temperature decreases ρ at 0.15–0.30 mm; opposite trend at 0.05 mm (ρ stays high or increases).

Chapter 4: Dielectric behaviour under dynamic shear

4.1 Introduction

The dielectric behaviour of conductive polymer composites depends strongly on network morphology, filler concentration, and external stimuli such as temperature and mechanical deformation. In MWCNT filled copolyesters, electrical transport arises through continuous MWCNT pathways, tunneling across MWCNT–MWCNT junctions, and interfacial polarization [61]. When MWCNT content exceeds the percolation threshold (~1 wt.%), conduction becomes the dominant mechanism [62], while Maxwell–Wagner–Sillars (MWS) polarization contributes primarily at low frequencies [63].

The objective of this study is to use dielectric rheology to resolve how dynamic mechanical deformation alters the electrical behaviour of polymer composites. Specifically, we aim to quantify how oscillatory shear influences the real (ε') and imaginary (ε'') components of permittivity in networks that are above the percolation threshold (5 wt.% and 10 wt.% MWCNT). By simultaneously applying mechanical shear and broadband dielectric spectroscopy, this work seeks to uncover how MWCNT connectivity, tunneling resistance, and interfacial polarization evolve under deformation. A further goal is to determine how temperature modifies these electromechanical interactions, as the experiments in this chapter are performed at 150 °C, which is above the glass-transition temperature (T_g) of the copolyester matrix. Operating above T_g ensures the polymer is in a softened, high-mobility state, allowing temperature-activated changes in MWCNT connectivity to occur under the same conditions used throughout our coupled dielectric–shear measurements.

Mechanical strain can modify MWCNT connectivity, changing tunneling gaps and junction density; thermal activation further enhances carrier mobility. Accordingly, this chapter examines these effects in copolyester composites containing 5 wt.% and 10 wt.% MWCNT by using (1) simultaneous oscillatory-shear and dielectric spectroscopy to study the electromechanical response under dynamic deformation, and (2) temperature-dependent dielectric tests without mechanical oscillation, following the same experimental structure used in the rest of this chapter. To the best of our knowledge, no prior study has applied broadband dielectric spectroscopy under dynamic shear to polymer composites far above percolation; this combined rheology–dielectric approach

therefore represents a unique experimental configuration and addresses a clear gap in the existing literature.

4.2 Materials and methods

Dielectric measurements were performed *in situ* under simultaneous mechanical oscillation using an integrated ARES G2 rotational rheometer (TA Instruments) coupled to an E4980LA LCR meter (Keysight Technologies). Cylindrical specimens with 25 mm parallel plate of rotational were mounted between the rheometer plates using a parallel plate geometry. The dielectric electrodes were integrated into the upper and lower plates, enabling simultaneous application of mechanical deformation and AC electrical excitation at root-mean-square potential of $1V$. The LCR meter applied a small signal AC voltage while sweeping electrical frequency in the range of 10^2–10^5 Hz from low to high frequency, and recorded capacitance, dielectric loss tangent and permittivity values. The rheometer applied controlled oscillatory shear deformation at mechanical oscillation frequencies of 10 rad s^{-1} and 30 rad s^{-1}, while strain amplitudes of 10%, 50%, and 100% were imposed.

Samples of both copolyester 5 wt.% MWCNT(ABR) and copolyester 10 wt.% MWCNT (G_1839) were printed in disc shape with a diameter of 25 mm. Before each test, the sample was soaked for 5 minutes at the designated temperature. Conditioning of the axial normal force of 300 g was also maintained throughout all the tests to ensure proper connection between the sample and the geometries. Before testing, open and short compensation procedures were performed directly on the rheometer–LCR integrated geometry to account for parasitic capacitances and fixture contributions. Calibration was performed at the lowest experimental temperature (~150 °C before sample loading) to minimize temperature-dependent parasitic effects (unwanted fixture capacitance that increases as the metal insulator geometry changes with temperature). This correction is essential in our high temperature dielectric shear tests because parasitic capacitance rises with fixture and wiring expansion, and without calibration would produce an artificial increase in measured permittivity as the sample is heated. This step ensured that the extracted complex permittivity originated primarily from the composite specimen rather than from the measurement hardware.

A second dielectric experiment was conducted to characterize the temperature dependence of the composite permittivity in the absence of mechanical oscillation. As in the coupled rheology-

dielectric configuration, the samples were prepared as 25mm diameter discs and positioned between the parallel plates of the ARES-G2 rheometer, with the LCR meter connected through the dielectric fixture to enable simultaneous electrical measurement. In this configuration, the rheometer was used only for control of temperature, axial force and axial alignment; no oscillatory strain was applied, and the samples remained static.

Prior to testing, open and short circuit calibrations were performed at the lowest test temperature (125 °C) to compensate for parasitic capacitance and fixture related stray impedance. Following calibration, temperature was increased stepwise (125 °C → 200 °C, step size of 25 °C), while maintaining a constant normal force sufficient to ensure full surface contact. At each temperature, dielectric spectra were recorded across 10^2–10^6 Hz, from which both storage permittivity (ε′) and loss permittivity (ε″) were obtained. All spectra were collected under isothermal conditions after temperature stabilization. Unlike the mechanical coupled measurements, no oscillation frequency parameter was present here; therefore, the resulting data captures the influence of thermal activation on charge transport, interfacial polarization, and conduction pathways in the MWCNT–copolyester network under static conditions.

4.3 Results and discussion

4.3.1 Coupled oscillation and dielectric spectroscopy

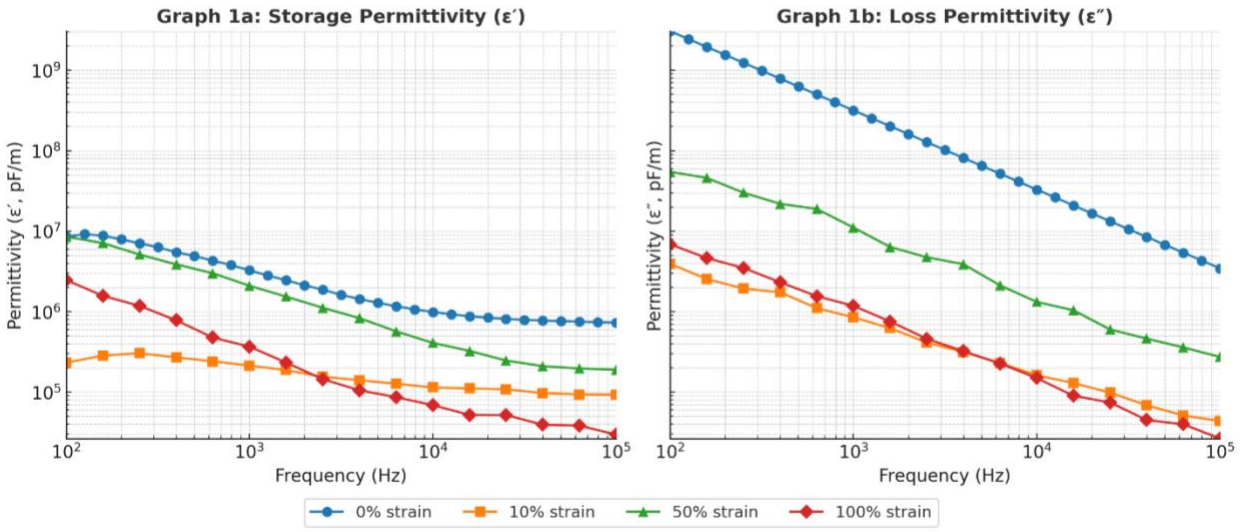

Figure 24: (a) Storage permittivity vs. frequency and (b) loss permittivity vs. frequency of copolyester 5% MWCNT at 150°C under varying shear strain at 1 rad/s as oscillation frequency

At 150 °C, and a mechanical oscillation frequency of 10 rad s^{-1}, both the storage (ε′) and loss (ε″) permittivity of the 5 wt.% MWCNT copolyester composite consistently decrease with increasing electrical frequency over the 10^2–10^5 Hz range (Figure 24). This frequency dependent decline reflects the relaxation behaviour typical of a conduction dominated composite. At lower frequencies, charge carriers can migrate and partially accumulate at MWCNT–polymer interfaces, resulting in localized interfacial polarization and higher permittivity. As the electrical frequency rises, the alternating field reverses too quickly for these carriers to respond, causing a gradual reduction in both ε′ and ε″ [64], [65]. In heterogeneous composites, charge carriers can accumulate at the interfaces between regions of different conductivity and permittivity, giving rise to Maxwell–Wagner–Sillars (MWS) interfacial polarization. R Belhimria *et al.* [66] demonstrated this effect in fibre polymer composites, where it appears at low frequencies when interfacial charge buildup dominates. If measurements were taken at lower electrical frequencies (< 10^2 Hz), which is outside the range of our instrument, interfacial MWS polarization would likely become more prominent, as charge carriers would have enough time to gather at MWCNT–polymer interfaces before the field reverses.

Across all applied strain levels, the loss permittivity ε″ remains several orders of magnitude higher than the storage permittivity ε′. This indicates that dissipative losses arising from free-carrier motion overwhelmingly dominate the dielectric response. Specifically, the major contribution comes from ohmic leakage conduction along continuous percolating pathways formed by the conductive filler network, with an additional contribution from charge-hopping (tunneling) processes across the remaining narrow insulating gaps or isolated clusters. Because both mechanisms involve real transport of charge carriers rather than reversible polarization, they manifest almost exclusively in the imaginary part ε″ of the complex permittivity, leading to the observed $\varepsilon'' \gg \varepsilon'$ behaviour, and the slope of -1 in ε″(ω) vs *f* double-logarithmic graph. A similar behaviour has been reported by J. Belattar [67] for highly loaded carbon black polymer composites above percolation, where continuous conductive networks produce strong dielectric loss while interfacial polarization remains only a secondary contribution at low frequencies MWCNT–polymer composites typically exhibit a sharp increase in dielectric permittivity near the percolation threshold due to micro capacitor structures formed between neighboring nanotubes separated by thin polymer layers [67]. Previous work by Latko-Duralek *et al.* [3] on the polymer composite

systems used in this study has shown that the electrical percolation thresholds for this copolyester-MWCNT system occur between 0.9 and 1 wt.%, meaning that both composites investigated here (5 wt.% and 10 wt.%) are well above percolation. Mechanical strain generally lowers both ε′ and ε″, but without altering the general frequency trend. The continuous conductive pathways formed at these loadings governs charge transport and energy dissipation, while interfacial MWS polarization contributes only marginally at low frequencies. The high MWCNT content at 5 wt.%, well above the percolation threshold, forms conductive pathways that span the sample, causing most of the applied electric energy to be dissipated as heat via charge transport rather than stored as dipolar polarization.

Mechanical strain generally decreases both ε' and ε'', but without altering the general frequency trend. The unstrained state (0 %) exhibits the highest permittivity values, consistent with intact MWCNT junctions and stable conductive pathways. As strain increases, deformation disrupts or misaligns MWCNT clusters, reducing the effective connectivity of the percolated network and limiting charge-transport pathways. Dynamic shear, disrupts or misaligns MWCNT clusters formation, reducing the effective connectivity of the percolated network and limiting charge transport pathways. In principle, larger strain amplitudes should produce progressively lower ε′ and ε″ values, as increased elongation breaks conductive bridges and suppresses interfacial polarization. But the response in the 5 wt.% composite is not strictly monotonic across all strain levels. The 50% strain had higher permittivity than 10% and 100%. This suggests a competition between two strain-driven processes. First at intermediate deformation, shear can promote microstructural rearrangement, such as densification or partial alignment of MWCNT clusters, which locally improves network connectivity and reduces average tunneling distances, second at larger deformation (100%), damage mechanisms such as debonding, micro voiding, and irreversible cluster separation dominate, leading to a net loss of conductive pathways and a strong drop in permittivity. The resulting non-monotonic strain dependence is therefore consistent with a moderately above-percolation network in which mechanical loading can both reorganize and destruct the conductive pathways, depending on the strain amplitude.

A subtle crossover between the 10 % and 100 % strain curves occurs between 10^3–10^4 Hz in both ε' and ε''. At low frequencies, the heavily strained (100%) sample occasionally exhibits slightly higher permittivity, likely due to slow relaxation of trapped charges in micro gaps formed by partial

separation of MWCNT clusters. This transient increase does not reflect renewed interfacial polarization, but instead localized charge accumulation in mechanically induced voids that temporarily delay carrier relaxation. In contrast, the 50% strain condition consistently exhibits higher permittivity than both the 10% and 100% strain states. To the best of our knowledge, this non-monotonic strain response has not been reported in the literature for similar MWCNT-polymer systems. We hypothesize that moderate deformation at 50% strain may reorganize and partially align MWCNT clusters without completely fragmenting the conductive network. This structural rearrangement could potentially (i) reduce average tunneling distances between nanotubes, (ii) increase the probability of inter-cluster contact, or (iii) enlarge the effective interfacial area involved in charge movement. These mechanisms would enhance charge hopping and localized conduction compared to the lightly strained (10%) state, where deformation is insufficient to significantly alter network topology. Under extreme deformation (100% strain), the network experiences large scale debonding and separation, sharply lowering both ε' and ε'' due to decreased conductive bridge density. To the best of our knowledge, no previous study has reported the same dielectric spectroscopy under dynamic shear, using polymer composite way above percolation, which indicates the gap in this research area. Strugova et al. [68] investigated the evolution of morphology and electrical properties of polypropylene (PP), and polystyrene (PS) blend nanocomposites containing few-layer graphene (FLG) or a mixture of FLG and MWCNT under controlled steady shear flow, not dynamic shear. They saw that steady shear deformation disrupted the electrical network in both PP/PS/FLG and PS/PP/FLG composites, and lead to reduction in conductivity. However, the PS/PP/FLG composites exhibited greater stability in electrical conductivity at lower FLG concentrations (above 3 wt.%) compared to the PP/PS/FLG composites (above 6 wt.%).

However, our explanation remains speculative and requires further experimental validation, such as direct microscopic observation through scanning electron microscopy (SEM). Additionally, simultaneous mechanical and electrical characterization with controlled displacement could help establish whether this behavior is reproducible as it wasn't seen for copolyester 10 wt. % MWCNT. Overall, a non-monotonic strain-dependent response in the 5 wt.% composite was witnessed. The undeformed state (0% strain) maintains an intact MWCNT network and exhibits maximum permittivity. Light deformation (10% strain) produces mild network distortion and modest reduction in dielectric properties. Intermediate strain (50%) shows enhanced permittivity,

potentially reflecting favorable network reorganization. Severe deformation (100% strain) causes network rupture and a substantial decline in both storage and loss permittivity.

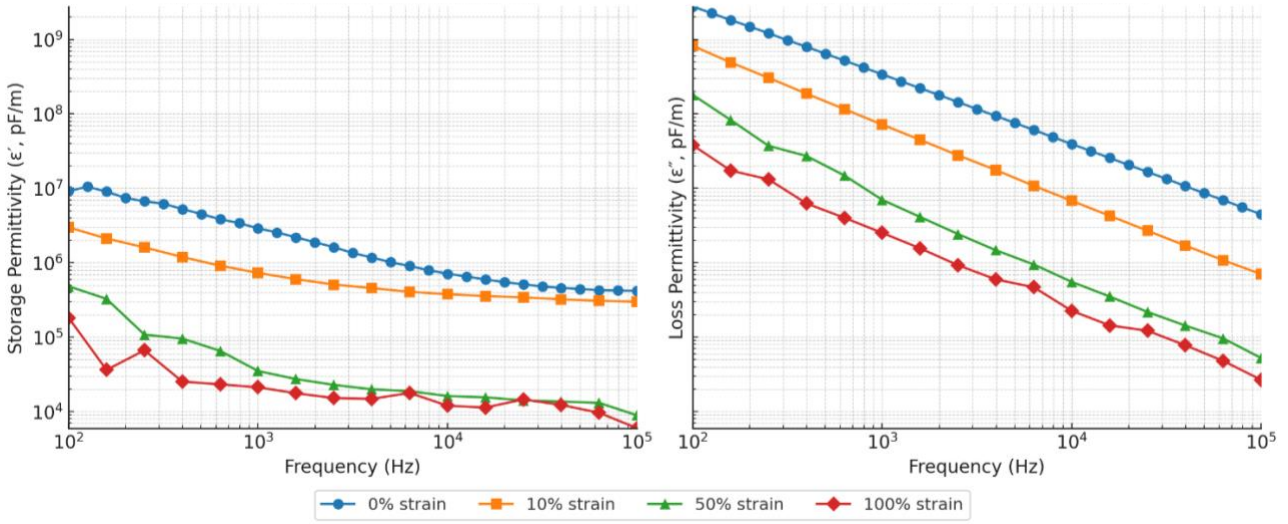

Figure 25: Storage permittivity, and loss permittivity vs frequency of copolyester 10% MWCNT at $150^{\circ}C$

Compared with the 5 wt.% composite, the 10 wt.% MWCNT copolyester exhibits an even more distinctly conduction dominated dielectric response. At 150 °C and 10 rad s^{-1}, both ε′ and ε″ decrease smoothly as electrical frequency increases from 10^2 to 10^5 Hz (Figure 25). This monotonic decline reflects the dominant role of charge migration and tunneling through a dense MWCNT network rather than interfacial polarization effects. At low frequencies, charge carriers have sufficient time to traverse these conductive pathways and accumulate locally, producing higher permittivity in both storage (real), and loss (imaginary). As the frequency increases, rapid field reversals prevent carriers from following the field, leading to the observed reduction in ε′ and ε″ as explained before.

Similar to copolyester 5 wt. % MWCNT in the entire frequency band, $\varepsilon'' \gg \varepsilon'$, confirming that dissipative conduction processes dominate over purely capacitive storage. Such behaviour is characteristic of composites positioned well above the electrical percolation threshold. Although the strain ordering is monotonic, the magnitude of strain induced decline is larger than in the 5 wt.% composite. For example, at 100 Hz, ε′ decreases by approximately 94 % from 0 % to 100 % strain (~2.98×10^6 $pF/m \rightarrow 1.82 \times 10^5$ pF/m), whereas the corresponding decline in the 5 wt.%

composite is ~83 %. Thus, the more densely percolated 10 wt.% network is less tolerant to large mechanical deformation which is in agreement with the findings of Strugova et al [68].

Comparison with the 5 wt.% composite highlights differences in strain effect on the electrical behaviour. Although both loadings are well above the percolation threshold (<1 wt.%), the 5 wt.% composite still exhibits a combination of conductive transport and interfacial polarization effects. As a result, it shows stronger frequency dependent dispersion and occasional strain induced crossovers in the 10^3–10^4 Hz range. In contrast, the 10 wt.% composite is fully conduction dominated across the measurement range, showing smoother frequency dispersion and no strain curve intersection. This reflects a denser MWCNT network in which deformation mainly breaks existing contacts rather than reorienting or creating new ones. The 5 wt.% sample exhibits higher relative storage contribution and greater strain sensitivity, whereas the 10 wt.% composite demonstrates higher baseline conductivity but greater permittivity collapse under large strain. These claims need more investigation, as with the current setup we use, it is not appropriate to compare the absolute value of two different samples.

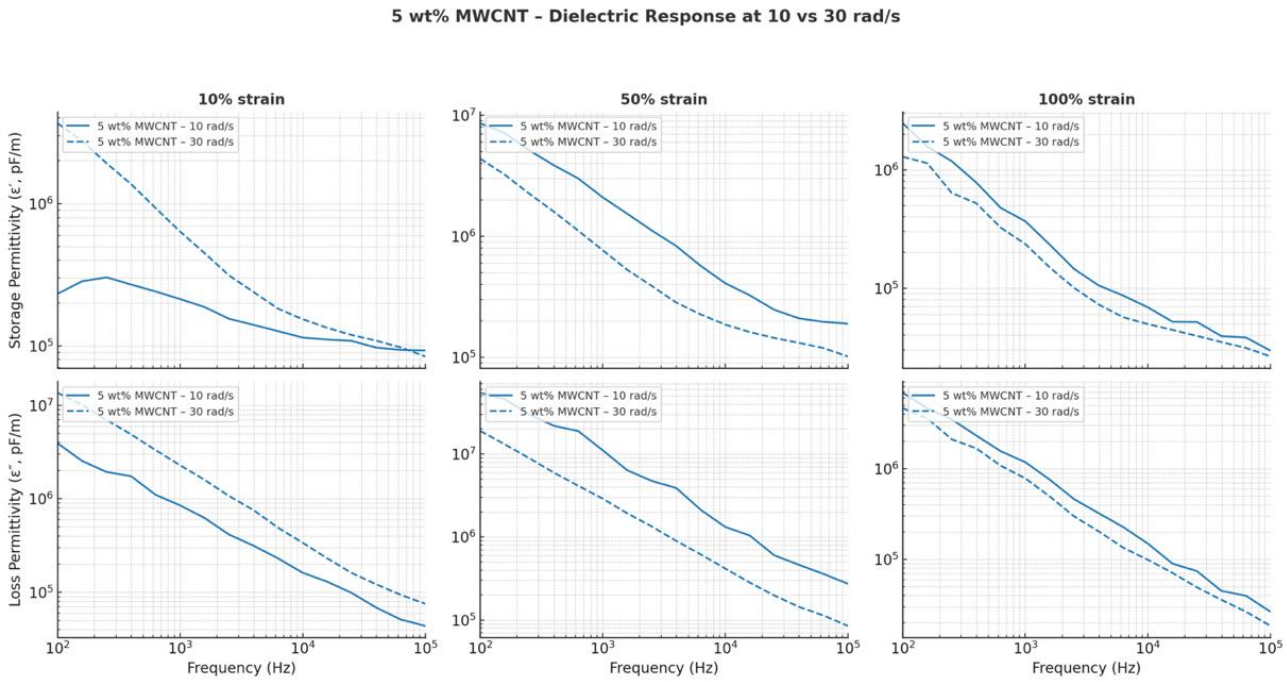

Figure 26: Storage and loss permittivity of the copolyester composite containing 5 wt.% MWCNT under 10% (left), 50% (middle), and 100% (right) strain amplitude, comparing dielectric response at 10 rad/s and 30 rad/s dynamic shear rate.

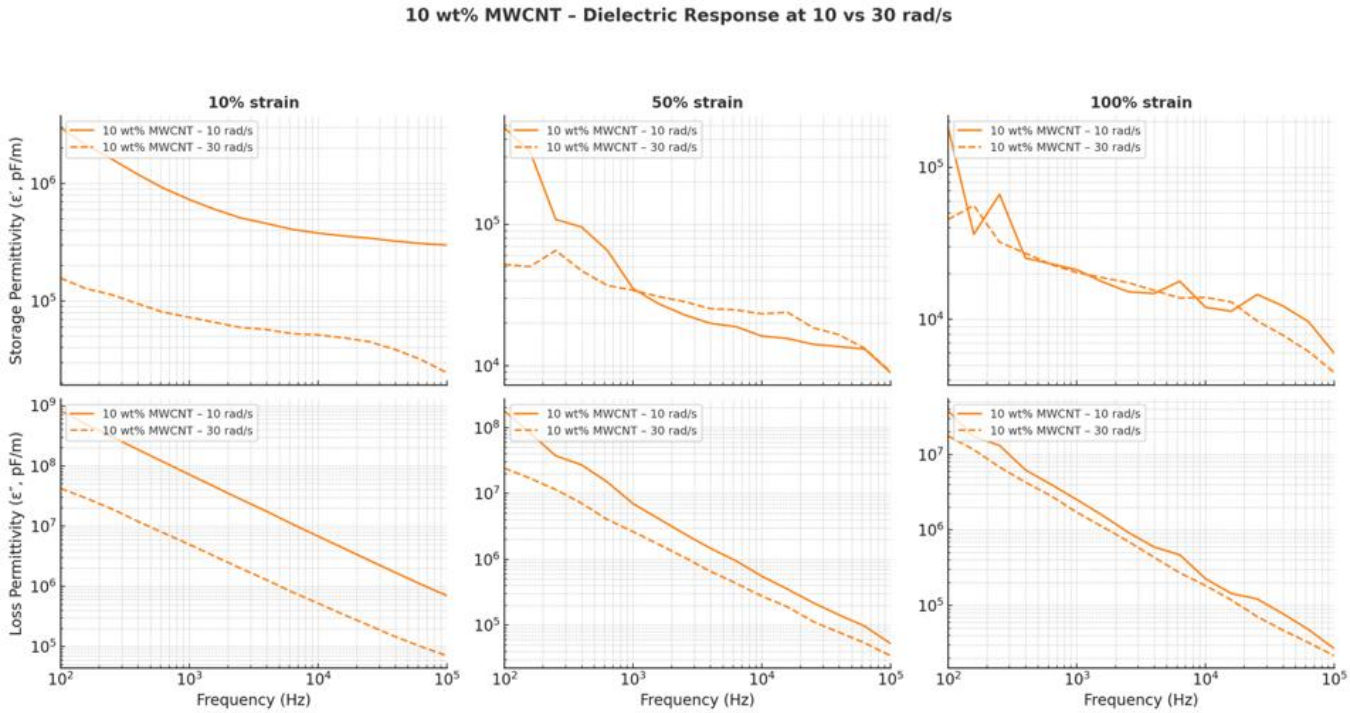

Figure 27: Storage and loss permittivity of the copolyester composite containing 5 wt.% MWCNT under 10% (left), 50% (middle), and 100% (right) strain amplitude, comparing dielectric response at 10 rad/s and 30 rad/s dynamic shear rate.

Figure 26, and 27 presents the effect of mechanical oscillation frequency (10 and 30 rad s^{-1}) on the dielectric behaviour of the 5 wt.% and 10 wt.% MWCNT copolyester composites at 150 °C for strain amplitudes of 10%, 50%, and 100%. At 10% strain in 5 wt.% MWCNT, increasing the oscillation rate to 30 rad s^{-1} yields slightly higher ε′ at low frequencies (<10^3 Hz), while both curves converge near 10^4 Hz. The corresponding ε″ remains higher at 30 rad s^{-1} across the full band. At 50 % and 100 % strain, the trend reverses: the 10 rad s^{-1} response remains higher for both ε′ and ε″ at all frequencies. The reduced gap between the 10 and 30 rad s^{-1} curves with increasing strain implies that network damage becomes the dominant influence once large deformation sets in, overshadowing the oscillation rate effect. We hypothesize that the observed strain-insensitive

conduction originates from the behaviour described above, but a more comprehensive investigation would be required to fully characterize this aspect.

At 10% strain in 10 wt.% MWCNT, the change rate dependence is opposite: 10 rad s^{-1} yields higher ε′ and ε″ than 30 rad s^{-1}, which we didn't observed for 5% wt. MWCNT. At 50% and 100% strain, ε″ and generally ε′ remain higher for 10 rad s^{-1}, but the relative difference between the two rates is smaller than in the 5 wt.% sample. The reason may be due to the denser and more redundant conductive network at 10 wt.% which could reduce the sensitivity to shear rate.

Overall, slower oscillation (10 rad s^{-1}) tends to maintain higher ε′ and ε″ by preserving MWCNT–MWCNT contacts and allowing time for stress relaxation within each mechanical cycle. Faster oscillation (30 rad s^{-1}) may temporarily enhance charge mobility at small strain through cyclic compression but generally accelerates microstructural fatigue under larger deformation.

4.3.2 Dielectric spectroscopic analysis of temperature dependency

As part of the dielectric characterization, the temperature dependence of permittivity was examined in the absence of mechanical oscillation. Raising the temperature from 125 °C to 200 °C produces a clear upward shift in both the storage (ε′) and loss (ε″) permittivity across the entire 10^2–10^6 Hz window (Figure 28). At low electrical frequencies (~10^2 Hz), ε′ increases by approximately one order of magnitude, from about 10^6 *pF/m* at 125 °C to about 10^7 *pF/m* at 200 °C, whereas ε″ grows more strongly. This temperature driven increase gradually diminishes with frequency, and above ~10^5 Hz the ε′ curves approach a shallow plateau of ~10^5–10^6 *pF/m*. Meanwhile, ε″ continues to decay smoothly and nearly linearly on a log–log scale, with a slope close to –1, suggesting a σ/(ε₀ω) type behaviour. Throughout the entire spectrum, ε″ remains significantly larger than ε′, confirming that the dielectric response is dominated by dissipative and conduction related processes rather than energy storage mechanisms, as we saw in the previous experiment.

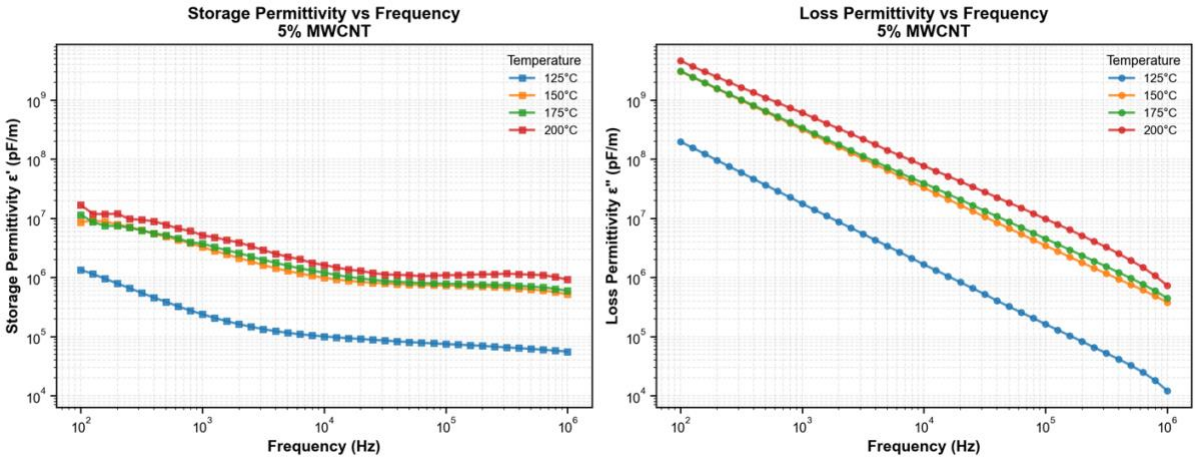

Figure 28: Storage and loss permittivity of copolyester 5 wt.% MWCNT at different temperatures

The temperature sensitivity of ε″ is consistent with increased charge mobility and enhanced hopping/tunneling transport within the percolated MWCNT network. Since the 5 wt.% loading lies well above the percolation threshold, electrical transport is not limited by isolated MWCNT clusters; instead, heat promotes charge delocalization along MWCNT–MWCNT contacts and reduces energy barriers for tunneling, increasing the effective conductivity [69]. Because the imaginary component is strongly influenced by $\sigma(T)/(\varepsilon_0\omega)$, ε″ shifts upward almost in parallel with temperature at all frequencies and keeps the -1 slope. A similar trend is seen in ε′. At high temperature, greater carrier mobility facilitates charge accumulation at MWCNT–polymer interfaces, producing higher ε′ values; however, at high frequency, the field oscillates too rapidly for such buildup. These results could indicate that temperature primarily enhances charge transport and energy dissipation rather than fundamentally altering the polarization mechanism.

Li et al. [70] reported observed a cross temperature in temperature dependence of impedance of MWCNT/polyvinylidene fluoride (PVDF) composites. The dielectric constants of these composites initially increased and then decreased with increasing temperature. However, upon further temperature increase, the dielectric constant again increases with increasing temperature. We did not observe the same behaviour in our materials, likely due to the shorter range of explored temperature and also higher overall percolation between conductive networks.

In some of our high-temperature experiments, both the 5 wt. %, and 10 wt. % MWCNT composites exhibited negative values in the extracted storage and loss permittivity at high frequencies. The 10

wt. % MWCNT formulation reached this instability at a lower temperature. These negative values do not have any physical meaning and simply indicate that the LCR meter is no longer capable of calculating reliable permittivity. Although the exact cause cannot be confirmed within this study, this instability may arise because the composite becomes highly conductive at elevated temperatures, which could drive the phase angle at high frequencies toward zero and force the instrument's equivalent circuit model to fail. The fact that these negative values appeared intermittently and were not consistently reproduced also prevents any firm interpretation. This limitation ultimately made it difficult to explore the very high-temperature regime, where the polymer itself becomes extremely soft and challenging to measure reliably. It is also worth mentioning that the lower region of the storage permittivity is being superimposed by electrode polarization, which makes it difficult to capture any type of relaxation. Further investigation and adjustments are needed to minimize the effect of electrode polarization.

4.4 Modeling of dielectric relaxation

As discussed in Chapter 2, there are several dielectric models to predict the electrical behaviour of dielectric material and especially composites. The analysis of dielectric data from polymer composites typically begins with traditional relaxation models, with the Cole-Cole model being the most widely used approach. Since ε* is a single complex function whose real and imaginary parts arise from the same set of model parameters, the Cole–Cole formulation should, in principle, describe both ε′ and ε″ simultaneously. To evaluate the applicability of this model to dielectric measurements, we initially attempted to fit the experimental data using the standard Cole-Cole formulation. The results revealed a striking contrast between storage and loss permittivity. For the storage permittivity (ε'), the Cole-Cole model provided an excellent fit with parameters $\varepsilon_\infty = 4.78 \times 10^5\ pF/m$, $\varepsilon_s = 4.10 \times 10^8\ pF/m$, $\tau = 0.850$ s, and $\alpha = 0.473$, achieving a coefficient of determination $R^2 = 0.989$. The experimental data points closely followed the fitted curve, indicating that the storage component exhibits relaxation behaviour consistent with the Cole-Cole framework.

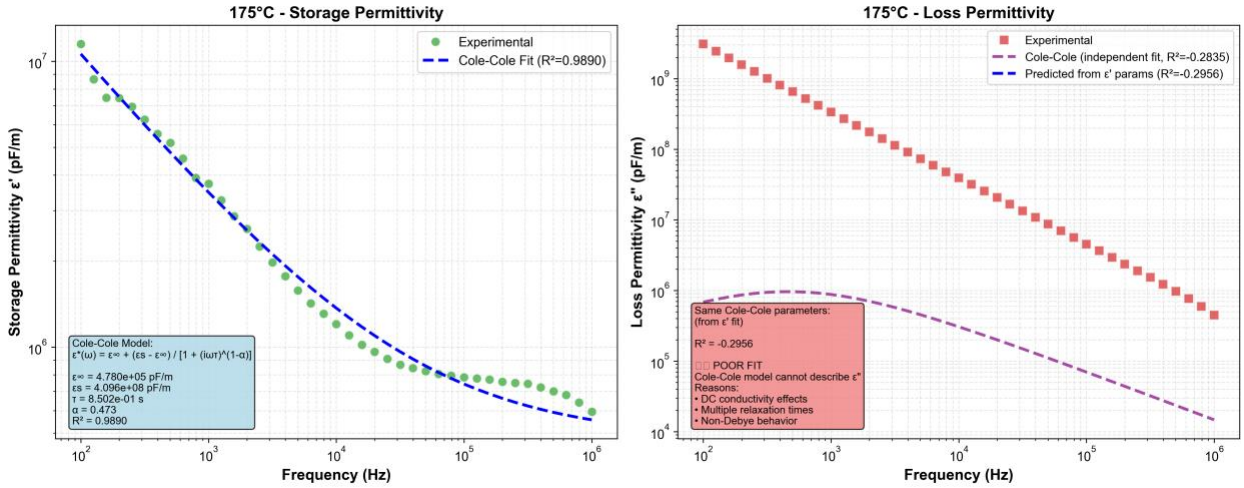

Figure 29: Cole-Cole fitting of storage and loss permittivity at $175^{\circ}C$ for ABR

However, when the same parameters were used to predict the loss permittivity (ε''), the model failed catastrophically, yielding R^2 = -0.296. Even when attempting to fit the loss data independently with its own set of Cole-Cole parameters, the fit remained poor (R^2 = -0.283). The negative R^2 values indicate that the model predictions are worse than simply using the mean value of the data, demonstrating that the Cole-Cole model fundamentally cannot describe the loss permittivity behaviour observed in these materials.

This failure is not merely a matter of parameter optimization but reflects a fundamental mismatch between the model's assumptions and the physical processes occurring in the material. A detailed examination of the loss permittivity data reveals three key characteristics that explain why traditional relaxation models are inadequate. First, the data shows a monotonic decrease across the entire frequency range (100 Hz to 1 MHz) with no observable relaxation peak.

4.5 Chapter summary and key findings

This chapter demonstrated that the dielectric response of MWCNT–copolyester composites under dynamic shear is governed predominantly by conduction processes associated with continuous percolated networks. Both composites 5 wt.% and 10 wt.%, exhibited $\varepsilon'' \gg \varepsilon'$ and a near $1/\omega$ decay in ε'' across 10^2–10^5 Hz, confirming that ohmic leakage and tunneling-driven transport dominate rather than dipolar or interfacial relaxation. Strain significantly alters network connectivity, but the manner of this response depends on filler loading. The 5 wt.% composite showed a non-monotonic strain dependence in which moderate deformation (50%) temporarily enhanced

permittivity, suggesting microstructural rearrangement consistent with a moderately-above-percolation network. Conversely, the 10 wt.% composite displayed a strictly monotonic decline in ε' and ε'' with increasing strain, indicating that its denser conductive network is less reconfigurable and more prone to irreversible contact loss under deformation. Oscillation-rate effects were secondary but systematic: lower mechanical frequency (10 rad/s) tended to preserve conductive junctions, whereas 30 rad/s promoted faster microstructural fatigue.

Independent temperature-only measurements revealed that increasing temperature (125–200 °C) primarily enhances charge transport by reducing tunneling barriers, yielding parallel upward shifts in ε' and ε'' without introducing relaxation peaks. The smooth $\sigma(T)/(\varepsilon_0\omega)$ behaviour further supports the dominance of conduction rather than Maxwell–Wagner–Sillars polarization at the tested loadings and frequency range. The failure of the Cole–Cole model to reproduce ε'' highlights this fundamental mismatch between classical relaxation models and conduction-dominated composites well above percolation.

Chapter 5: Prototyping of flexible strain sensors

5.1 Introduction

This chapter provides a clear overview of the sensing platform used in this work, from the printed device itself to the hardware and software that extract its capacitance changes. The sensor is produced as a single-step multi-material print, where a flexible MWCNT-based conductive filament forms the electrodes and TPU forms the surrounding structure. A hexagonal layout (Figure 30) is used because it gives a stable electrode separation and a controlled deformation path during manual compression. To measure the sensor response, the printed capacitor was connected to an LC resonant circuit monitored by the FDC2214 evaluation module (Figure 32). The board tracks frequency shifts associated with changes in capacitance, and a Python based acquisition system handles configuration, continuous streaming, drift management and real time visualisation. Together, these elements form the complete pathway for generating the data used in the subsequent analysis.

5.2 Sensor design and fabrication

The sensing element is a single step, multi-material FDM build produced on a Prusa MK3S+ equipped with a Multi Material Unit (MMU). This configuration enables automatic switching between two filaments:

(1) a flexible, conductive MWCNT–polymer composite (ABR, or G2A-10, or G1839), used to form the electrodes
(2) a non-conductive flexible filament, Ninjaflex TPU by Ninja Tek

The active device consists of a planar hexagonal body containing two opposing conductive walls that function as electrodes. All remaining walls and internal space are printed from the nonconductive flexible polymer. As it can be seen in Figure 30, the orange section is the nonconductive body, and the black section is the conductive walls. The hexagonal geometry was selected because it provides a simple, symmetric baseline separation between electrodes, a compact footprint, and deformation paths that are predictable under manual compression. Furthermore, the overlap area remains constant under compression, which facilitates easier

calibration of the sensor. Some versions include square extensions on opposite sides to make handling during compression easier (Figure 31).

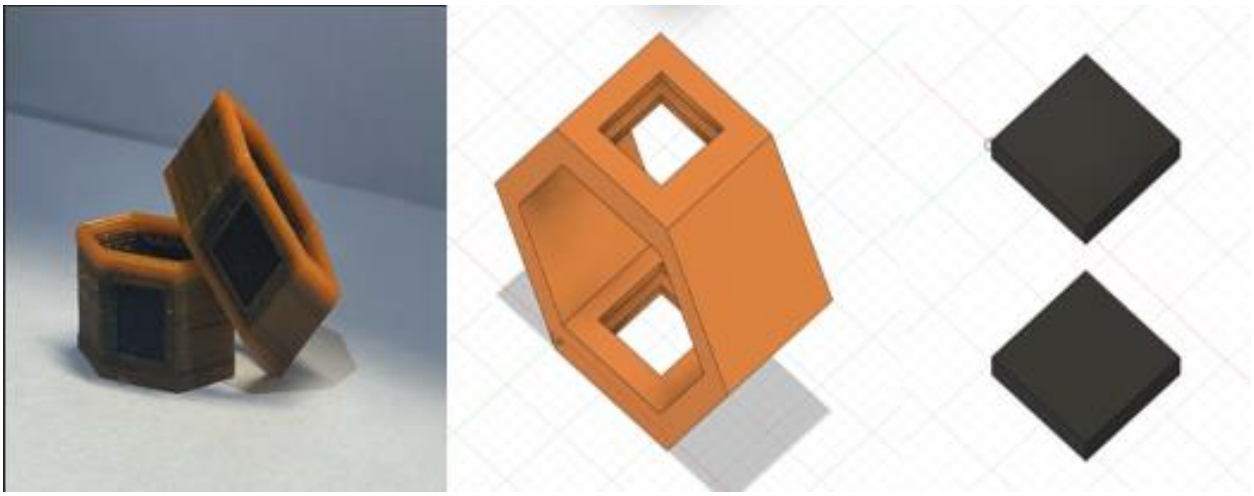

Figure 30: 3D modeling of hexagonal sensor design

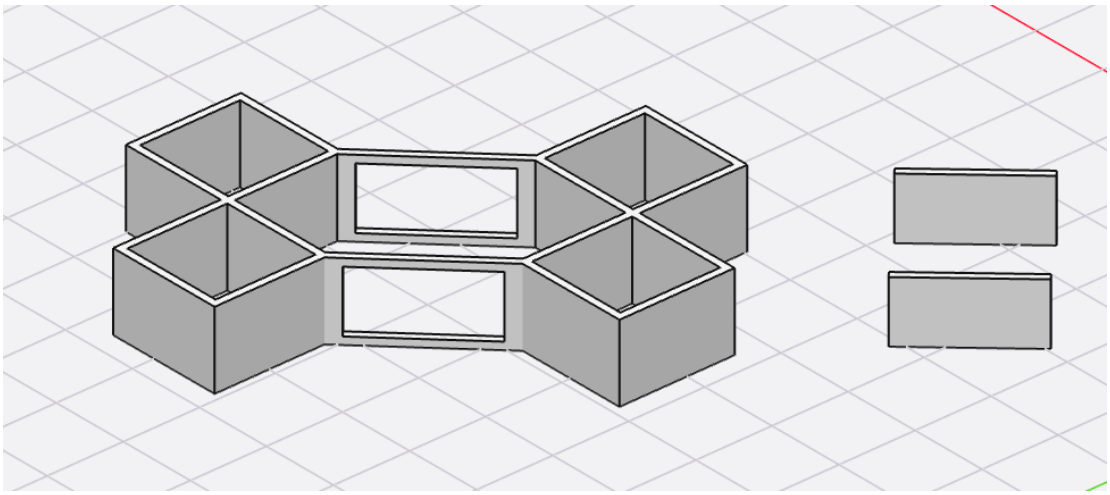

Figure 31: 3D modeling of hexagonal with square extension sensor design

The main challenge we face is the adhesion between the conductive and nonconductive parts, specifically to improve the adhesion of the hollow part inside the nonconductive part so the conductive electrode has more area for adhesion to the nonconductive part. Although the electrodes and dielectric are fabricated together, the electrical interface is not fully printed. To

interface the sensor with the device, the exposed ends of the conductive walls are manually coated with silver based conductive paint, and 34-gauge NiCr wire leads are bonded to these painted regions. This method was chosen because it provides reliable low contact resistance without modifying the printed geometry; it also avoids requiring embedded wires during printing. The resulting hybrid structure remains mechanically continuous, and reliable mechanical attachment between the sensor and evaluation board is essential to prevent contact resistance fluctuations during handling and testing. The result is a compliant, monolithic printed capacitor whose electrode spacing and area are defined by the toolpath, while external terminals are provided via silver painted contact points and soldered wires. No lamination, stacking, or adhesive layer assembly is required; the only post processing step is the formation of the external electrical interface.

5.3 Readout hardware and measurement strategy

As explained in chapter 2, capacitance measurement methods vary widely including charge discharge timing, AC bridge techniques, impedance spectroscopy, and frequency domain oscillator methods. In this work, we chose the frequency domain, LC-based resonant measurement because of its high sensitivity to small ΔC, its robustness to parasitic and wiring effects, and mainly how simple it is to handle. This approach is inspired by the previous work of Jun et al. [71] at MIT, known as the MetaSense project.

The printed capacitor is integrated into an LC resonant tank circuit connected to the FDC2214 evaluation module (EVM). This module tracks the tank's resonant frequency and outputs a 28-bit digital code proportional to frequency. Since $f \propto \frac{1}{\sqrt{LC}}$, changes in capacitance due to deformation of the printed sensor correspond to monotonic shifts in the output code. The FDC2214 operates using a narrow band, frequency-tracking detection architecture that concentrates exclusively on the resonance of the LC circuit. The device excites the tank, locks onto its resonant frequency, and performs synchronous demodulation within a very small window around that frequency. Signals that fall outside this narrow region are strongly suppressed because they do not match the demodulation frequency. As a result, broadband electromagnetic interference, low frequency environmental drift, high frequency radio noise, and digital switching artefacts are rejected before they reach the output. Only energy located within several kilohertz of the LC resonance is

preserved, which is the region that carries the capacitive information of the sensor. This narrow band behaviour becomes even tighter at lower sampling rates, which explains the very low system noise floor of approximately 0.3 femtofarads at 100 samples per second. The effective filtering is therefore not based on discrete band selection but emerges naturally from the physics of lock-in detection and from the internal decimation that follows it. In practice, this means the instrumentation chain maintains high resolution and stability even in electrically noisy environments.

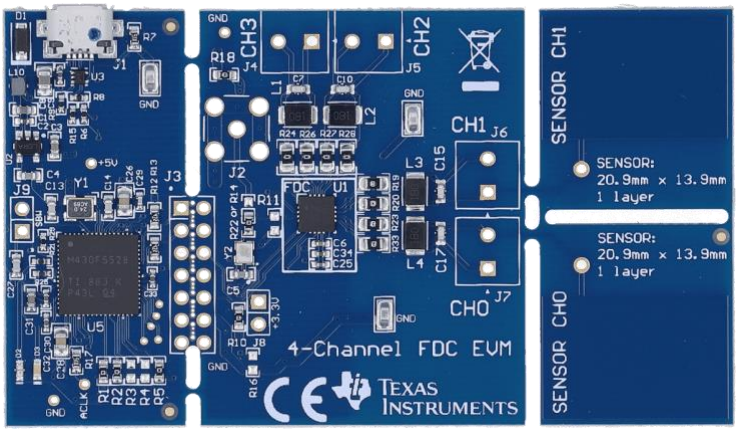

Figure 32: FDC2214 Evaluation module (EVM)

The printed capacitor was connected to channel CH0 of the EVM using the shortest possible leads. Lead length directly contributes stray capacitance and inductance; reducing the length therefore minimises parasitic loading on the LC tank, suppresses noise pickup, and ensures that the measured variation originates from the sensor itself rather than from wiring artefacts. The EVM was powered and accessed via USB, eliminating external supply hardware. A minimal test fixture was fabricated to secure the EVM and maintain strain isolation from cables. Figure 33 shows the general setup, including the printed sample, electrical connections, and the evaluation board. The board was operated in continuous streaming mode, allowing measurement values to be collected at ~100 Hz. Although the EVM can support higher rates with reduced resolution, the intended application and scope of this project does not demand higher temporal bandwidth.

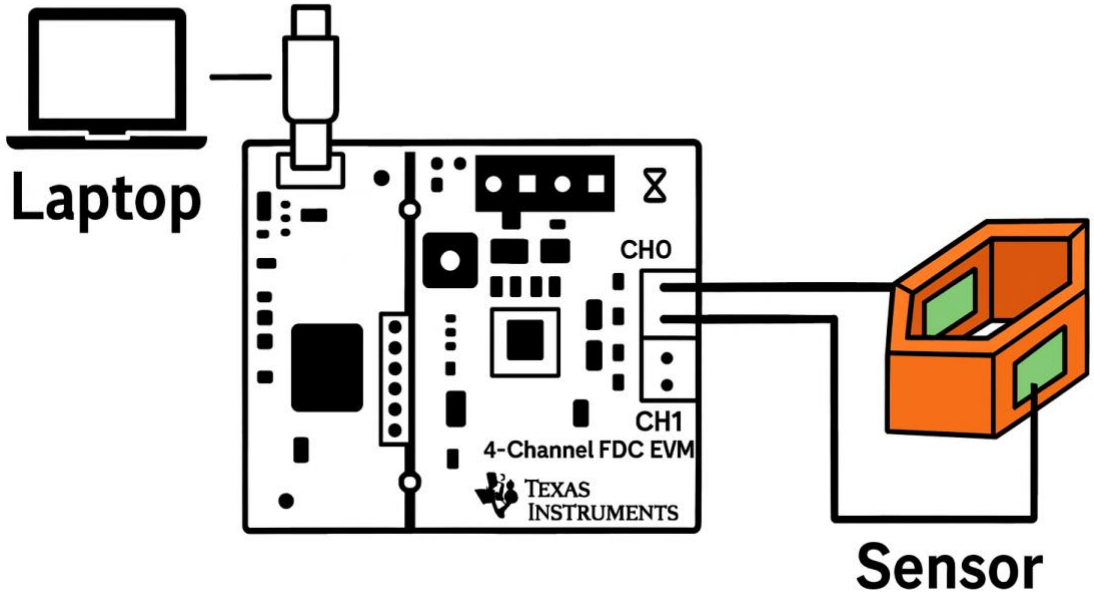

Figure 33: Schematic of sensor setup.

5.4 Software architecture and code-level description

The software stack is responsible for device configuration, real time data acquisition, filtering, streaming, storage, and visualisation. All acquisition logic was written in Python to allow rapid iteration and to avoid reliance on the proprietary desktop tools provided by the manufacturer. The system is organised around a single script that prepares the sensor, initiates the data stream, and exposes measurements through both persistent storage and a WebSocket broadcast channel. A secondary visualizer script provides a direct desktop view of the signal, while a JavaScript client built with p5.js offers a browser-based display. The process begins by scanning the available serial ports and attempting to identify the evaluation board using the vendor and product identifiers assigned by the manufacturer. If automatic detection fails, the user can select a port manually. When no valid hardware is present, the software automatically switches to a synthetic simulator that generates structured measurement data, which can keep the software running and waiting for receive connection. This keeps the entire visualisation pathway operational even when the physical board is not connected. Once a valid device is detected, the script writes a set of configuration registers inside the FDC2214. These registers are small memory locations that control how the

sensor behaves, including how quickly it measures, how long it waits for the signal to stabilise, which internal clocking mode it uses, and which sensing channel is active. The registers are written through a compact binary protocol that includes an eight-bit cyclic redundancy check, which confirms that each message has been delivered without corruption. A detailed description of the configuration registers appears in the section. After configuration, the board enters continuous streaming mode. In this mode, the device sends measurement frames at regular intervals without requiring further commands from the host computer. This avoids timing irregularities caused by software delays and is essential for a capacitive sensor that is sensitive to slow drift from temperature changes and mechanical relaxation of the printed structures.

The script then enters a non blocking loop that processes each incoming frame as soon as it arrives. The packet is verified using its integrity field, then passed through a rolling calibration step to correct gradual baseline movement caused by environmental factors. A smoothing stage reduces short term noise that does not reflect real physical changes. The raw, unmodified readings are written to an HDF5 file so that the complete signal remains available for later scientific analysis. At the same time, the normalised and smoothed values are broadcast through a WebSocket interface, allowing any connected visualisation tool to present a stable, real-time view of the sensor output. This structure keeps data acquisition, storage, and presentation clearly separated. The untouched data provide a reliable scientific record, while the processed stream offers an immediately interpretable signal for live monitoring. The acquisition system is implemented as a single Python application that integrates device discovery, register programming, binary protocol communication, continuous data streaming, adaptive signal conditioning, persistent storage, and network broadcasting. Although the script presents itself as a unified file, its internal organization follows a structured pipeline in which each stage performs a well-defined function. The script begins by defining symbolic constants corresponding to the FDC2214's internal register addresses. An example excerpt is shown below:

```
EVM_RCOUNT_CH0 = 0x08

EVM_SETTLECOUNT_CH0 = 0x10

EVM_CLOCK_DIVIDERS_CH0 = 0x14

EVM_DRIVE_CURRENT_CH0 = 0x1E
```

```
    EVM_MUX_CONFIG = 0x1B

    EVM_CONFIG = 0x1A
```

These symbolic names reproduce the device memory map exactly as documented in the datasheet and prevent index-based errors common in low-level register programming. Each register controls one element of the sensor's inductive measurement behaviour. The `RCOUNT` registers specify the conversion interval, which determines the number of oscillation cycles counted during each measurement and thus directly controls resolution. The `SETTLECOUNT` registers define the stabilisation interval following channel switching. The `CLOCK_DIVIDERS` entries determine the ratio between the reference clock and the sensor excitation signal, setting the effective sampling bandwidth. The `DRIVE_CURRENT` registers configure the amplitude of excitation current delivered to each LC tank, influencing oscillation strength and noise susceptibility. The `MUX_CONFIG` register establishes which channels are active and applies deglitch filtering, while the `CONFIG` register specifies the device's operational mode, including sleep, active, and external clock configurations.

All operational parameters applied prior to streaming are consolidated into a single configuration dictionary:

```
config_multichannel = {

    EVM_RCOUNT_CH0: 0xFFFF,(for all channels, removed for shortening)

    EVM_SETTLECOUNT_CH0: 0x0001,

    EVM_CLOCK_DIVIDERS_CH0: 0x1001,

    EVM_DRIVE_CURRENT_CH0: 0xF800,

    EVM_MUX_CONFIG: 0xC20D

}
```

The selected values reflect design decisions based on the operating characteristics of the FDC2214 and established conventions in prior hardware implementations. Setting `RCOUNT = 0xFFFF` on

every channel forces the longest possible conversion interval, thereby maximising effective resolution and reducing quantisation noise (the “rounding error” created by digitising an analogue signal). The `SETTLECOUNT = 0x0001` configuration minimises the delay following each channel transition. Given that the device is configured to continuously cycle across four channels, this setting achieves the fastest stable recapture of oscillation amplitude without introducing appreciable distortion.

The value `0x1001` written to the `CLOCK_DIVIDERS` registers configures both the reference and sensor clock dividers such that the excitation frequency remains stable while ensuring compatibility with the chosen conversion interval. This offers a suitable compromise between data rate and measurement precision. The `DRIVE_CURRENT` values determine the magnitude of current supplied to each resonant tank. Higher drive currents produce larger oscillation amplitudes and suppress jitter, but excessively high values may result in non-linear behaviour, particularly on smaller coils. Finally, the `MUX_CONFIG = 0xC20D` setting enables automatic sequential scanning of channels 0 through 3 and activates a 10 MHz deglitch filter intended to suppress high-frequency interference at the input.

The device uses TI’s simple binary command format. Each message the script sends is built as a small frame: command bytes first, then a CRC-8 at the end. The CRC is calculated inside `send_command()`,it runs the payload through the standard polynomial and tacks the checksum onto the frame before sending it out. On the FDC2214 side, the chip repeats the calculation when it receives a packet. If the CRC doesn’t match, the chip just throws the packet away instead of touching its registers. This keeps random serial noise or half-finished packets from flipping configuration bits.

A representative write operation is shown below:

```
def write_reg(port, addr, data):
    command = bytes.fromhex('4C150100042A') \
              + addr.to_bytes(1,'big') \
              + data.to_bytes(2,'big')
```

```
send_command(port, command)
```

The fixed header encodes the command type and packet structure; the register address and corresponding 16-bit data field follow; finally, the `send_command` routine augments the packet with a CRC-8 checksum. If the device reports a non-zero error code in its response header, execution terminates immediately to prevent operation in an inconsistent state.

Device initialisation proceeds by placing the FDC2214 into sleep mode, applying all configuration values from the dictionary, and then writing a final operational flag stored in `CONFIG_SETTING`. Once configured, the following instruction activates streaming mode:

```
start_stream(evm)
```

In this mode, the device autonomously transmits fixed-size 32-byte packets containing frequency conversion results for four sequential channels. Each packet is unpacked according to the layout defined in the datasheet:

```
def read_stream(serial_port): packet = serial_port.read(32)
(_, raw0, raw1, raw2, raw3) = struct.unpack('>3xB2xLLLL10x', packet)
```

The board outputs 32-byte packets corresponding to four sequential channel measurements. The unpacking format strips padding and header bytes, leaving 28-bit frequency codes as four unsigned integer values.

Unpacking 28 bits

`'>3xB2xLLLL10x'`:

- `>` → Big-endian byte order
- `3x` → Skip 3 bytes
- `B` → Read 1 unsigned byte
- `2x` → Skip 2 more bytes
- `LLLL` → Read 4 unsigned 32-bit integers — one per channel (raw_ch0 to raw_ch3)

- `10x` → Skip last 10 bytes of padding

Each new value is then introduced into a continuous min–max tracking window that maintains approximately ten seconds of recent data:

```
history[ch].append((t, raw))

while history[ch] and t - history[ch][0][0] > window:

       history[ch].pop(0)
```

This rolling buffer functions as an adaptive baseline correction method. Maintaining a fixed duration window allows the system to continually re-establish local minima and maxima without requiring explicit calibration cycles. The bounded window size ensures that only behaviour relevant to the current operating period contributes to normalisation.

Normalisation proceeds by computing the channel-specific range:

```
min_v = min(v for _, v in history[ch])

max_v = max(v for _, v in history[ch])

norm = (raw - min_v) / (max_v - min_v)
```

The resulting dimensionless quantity expresses the fractional deviation relative to the dynamic range observed in the recent window. Because deformation-induced changes are best captured via relative variation rather than absolute magnitude, this representation avoids dynamic-range compression and yields an intuitive scale.

To reduce jitter, a first-order exponential moving average is applied:

```
smoothed[ch] = round(

smoothed[ch] * smoothing_factor

+ norm * (1- smoothing_factor), 1

)
```

A smoothing coefficient of 0.5 was selected empirically as a compromise between responsiveness and noise suppression. The recursive form is computationally efficient and imposes no perceptible overhead on real-time acquisition.

Raw values are appended to an HDF5 dataset at the acquisition rate. Recording raw data ensures that future analyses can be conducted without distortion from online filtering or normalisation. Meanwhile, processed values are transmitted over an asynchronous WebSocket interface:

```
await websocket.send(
    f"{smoothed[0]},{smoothed[1]},{smoothed[2]},{smoothed[3]}"
)
```

Because the acquisition loop is non-blocking, multiple clients may monitor the sensor concurrently without affecting sampling frequency or database writes. Network latency does not propagate into the serial communication subsystem. In the event of an exception, the application closes the HDF5 table, stops streaming, and releases the serial port to maintain a consistent hardware state.

5.5 Real-time visualisation

Two visualisation paths were implemented: a Python desktop GUI and a browser-based p5.js client. Both subscribe to the same WebSocket stream. The Python GUI reads raw codes directly from the serial port, applies the same normalisation and smoothing pipeline, converts frequency to capacitance using the LC resonance expression, and displays the value as a height-modulated rectangle. Capacitance is obtained by mapping 28-bit output to frequency using the internal reference clock, then applying $C = \frac{1}{(2\pi f)^2 L}$, where L is the measured inductance of the external coil. The browser client is intentionally simple, receiving only pre-processed normalised values. Its rendering logic is summarised below:

```
ws = new WebSocket('ws://127.0.0.1:8080');
ws.onmessage = function(event) {
    let values = event.data.split(',');
    ch3Value = parseFloat(values[3]);
```

```
};
```

The value is displayed as a glowing cyan bar whose height corresponds to instantaneous relative change:

```
let rectHeight = map(ch3Value, 0, 100, 0, maxRectHeight);
rect(x, y, rectWidth, rectHeight, 0);
```

Because all computation occurs upstream, the client remains lightweight and platform independent. It can be opened from any web browser without installation, enabling rapid demonstration or remote observation across multiple machines. As it can be seen in the Figure 34, on the left is the undeformed sensor with the corresponding bar behind it, and the same thing on the right for the deformed sensor.

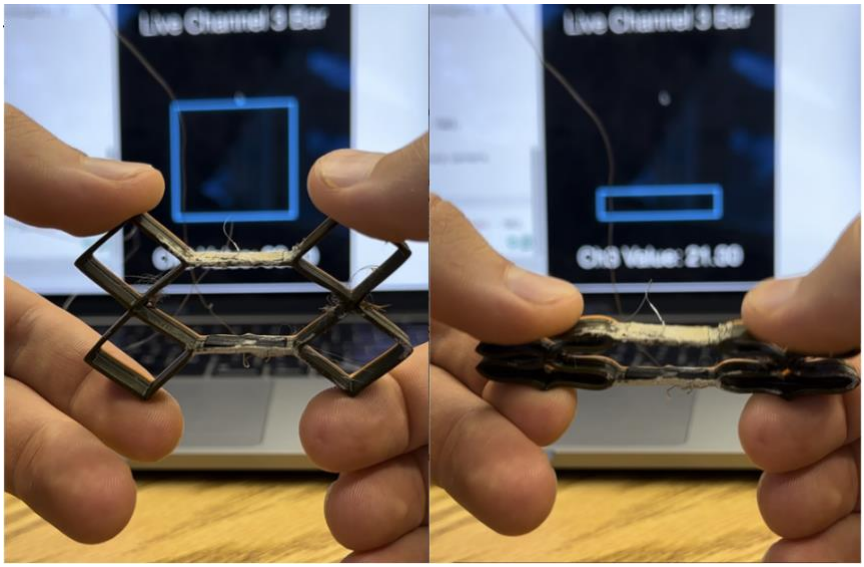

Figure 34: Demonstration of sensor performance (left) undeformed sensor, (right) deformed sensor.

The functional performance of the printed capacitive sensor was evaluated through manual compression-release cycles while monitoring the real-time capacitance response via the FDC2214 acquisition system. Figure 35 presents representative data from Channel 3, demonstrating the effect of the rolling min-max calibration algorithm on sensor readability. The left panel shows the raw normalized output before applying the adaptive calibration window. The sensor maintains a baseline around 90% in its undeformed state, with manual compressions producing drops to

approximately 80%. Figure 35 shows how adaptive minimum and maximum calibration change the sensor performance.

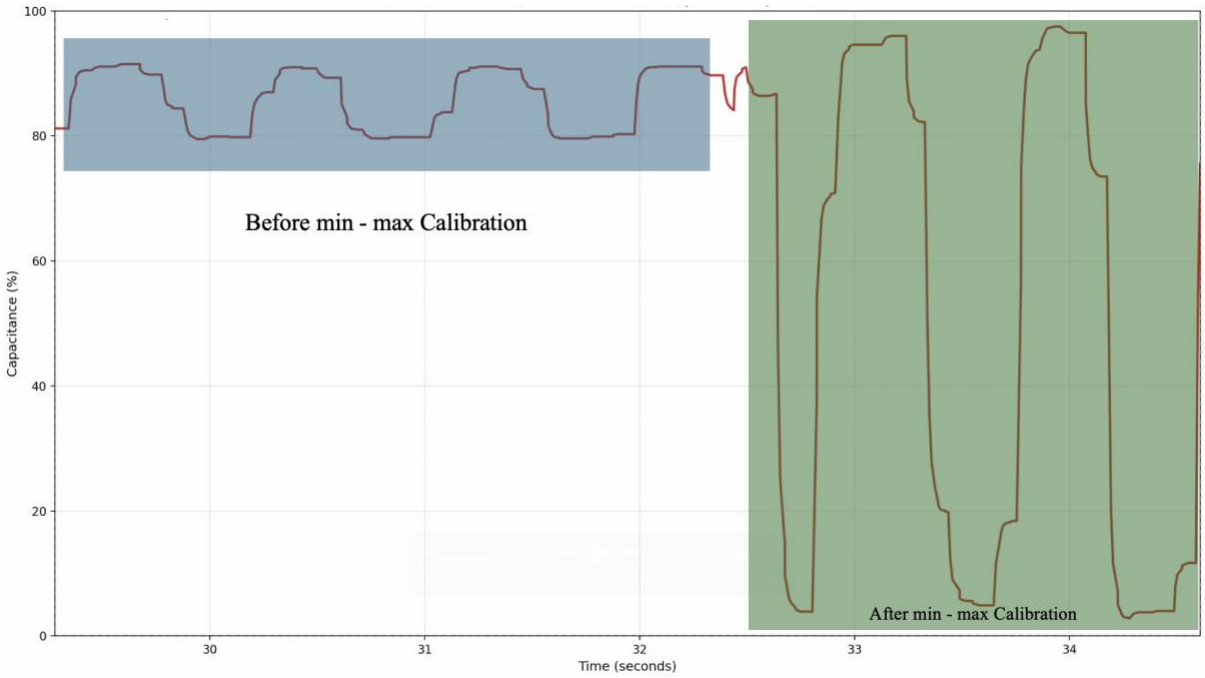

Figure 35: Real-time capacitance response of the 3D-printed sensor during manual compression cycles, showing the effect of the 10-second rolling min-max calibration.

The right panel demonstrates the effect of the 10-second rolling calibration described in Section 5.3. By continuously tracking minimum and maximum values and remapping the signal to span 0-100%, the system significantly enhances visual clarity.

5.6 Limitations and practical constraints

Although the acquisition pipeline provides a functional end to end pathway from printed sensor to visual output, several constraints limit its quantitative reliability. These constraints arise primarily from the electrical interfacing strategy, mechanical boundary conditions, environmental sensitivity, and the nature of the drift correction scheme. The most significant limitation concerns the physical connection between the printed composite electrodes and the evaluation board. Because the MWCNT–copolyester formulation does not readily form a mechanically secure or low-resistance bond with bare wiring, silver-based conductive paint, which itself can act as an electrode, is required not only to reduce contact resistance but to improve adhesion, and dried

silver paste can act as a conductive wall. Even with this treatment, 34-AWG Ni–Cr leads can shift under modest handling or during repeated strain.

A second limitation concerns noise introduced by lead wiring. The external wires introduce small but non negligible parasitic capacitances and act as mechanically compliant extensions of the electrodes. Motion of the leads relative to the board or surrounding objects readily couples into the resonant tank despite the high Q behaviour and internal filtering of the FDC2214. While the LC architecture inherently suppresses broadband electromagnetic interference, it does not reject mechanical perturbations of the wiring; these typically appear as genuine capacitance changes. Consequently, measurements remain sensitive to disturbances not originating in the printed structure.

Chapter 6 – Conclusion and future work

6.1 Conclusion

This thesis investigated how multi-walled carbon nanotube (MWCNT) hot-melt adhesive composites behave when processed by fused deposition modelling (FDM), how their dielectric and electromechanical responses evolve under frequency, temperature, and mechanical deformation. Across three experimental stages, we investigated 3D printing processing effects on conductivity, dielectric spectroscopy under dynamic mechanical strain, and the development of a functional capacitive 3D printed strain sensor.

The first major outcome is that the electrical performance of the printed composites is strongly governed by processing conditions. Layer height, raster orientation, printing speed, and nozzle temperature each reshaped the continuity of the MWCNT network. Increasing layer height from 0.05 mm to 0.30 mm consistently lowered resistivity, while alignment of the print path at 0 degrees produced the most conductive tracks and transverse deposition at 45 degrees yielded the highest resistivity. Printing speed showed a nonmonotonic trend, with a resistivity peak near 80 millimeters per second and lower values at both slower speeds of 40 to 60 millimeters per second and faster speeds near 120 millimeters per second. Nozzle temperature reduced resistivity when layers were sufficiently thick at 0.15 to 0.30 mm, but at very thin layers of 0.05 mm resistivity remained high or increased. Together, these observations demonstrate that conductivity in printed MWCNT composites is not an inherent material property but a process-dependent outcome dictated by how extrusion conditions assemble, align, and preserve the underlying MWCNT network.

The second major outcome concerns the dominant dielectric mechanisms operative in the composite. Across the 10^2–10^5 Hz range, both ε' and ε'' displayed monotonic decay with frequency and large conduction terms consistent with a $\sigma/(\varepsilon_0\omega)$ response. The absence of clear relaxation peaks indicates that classical dipolar or Maxwell–Wagner–Sillars polarization plays only a secondary role in these materials at the studied loadings. The network behaves as a percolated conductor whose AC response is governed by charge mobility rather than by polymer relaxations. Applying mechanical deformation further revealed that strain disrupts percolation by breaking or misaligning MWCNT–MWCNT junctions. High strains consistently reduced permittivity; the 10

wt.% composite showed the strongest absolute conductive response, while the 5 wt.% composite exhibited a subtle non-monotonic behaviour at intermediate strain that suggests temporary reorganisation or alignment of CNT clusters. This behaviour points to a more dynamic microstructural evolution under load than previously appreciated.

The final component of the thesis demonstrated a fully 3D printed monolithic capacitive strain sensor, produced in a single dual-material FDM operation. Flexible MWCNT composite filament was printed as the electrode architecture, and TPU formed the surrounding dielectric structure. The device exhibited clear, repeatable shifts in resonant frequency under deformation, confirming its capability as a functional soft sensor. Although raw signals exhibited drift and noise, simple but effective real-time processing, exponential smoothing and rolling min-max normalisation, yielded stable, easily interpretable outputs. This prototype validates that additive manufacturing can integrate conductive CNT networks and soft dielectrics into a seamless, fully printed sensing structure.

Taken together, the thesis establishes a coherent understanding: processing dictates microstructure; microstructure dictates dielectric and electromechanical behaviour; and these relationships can be exploited to design and print functional soft sensors.

6.2 Future work

Several focused research directions follow directly from the findings and limitations of this thesis.

A priority is to build a fixed, automated setup that can apply strain in a controlled manner while remaining isolated from any conductive components. This will allow proper calibration of the sensor and enable accurate evaluation of the relationship between the calculated percentage change and the actual applied deformation. Dedicated tensile and cyclic rigs are required to extract gauge factor, hysteresis, dynamic bandwidth, fatigue life, and long-term drift. This will transition the sensor from a qualitative demonstration to a fully benchmarked device.

The dielectric behaviour, specifically under dynamic shear is the gap in this region, and requires deeper exploration in three specific areas exposed by this thesis. Because the current study begins at 10^2 Hz, any slow interfacial or electrode polarization processes remain unobserved. Extending

measurements below 100*Hz* frequency is necessary to determine whether the composite hosts relaxation modes are currently hidden beneath the conduction-dominated regime. Microscopic imaging before and after dynamic loading could reveal whether shear cycles produce irreversible damage, reversible realignment, or entirely distinct network states before and after deformation. As noted earlier in the dielectric experiments, negative permittivity values were observed in some high-temperature, high-frequency measurements. Although these values are nonphysical and arise from limitations of the measurement method, their exact origin remains unresolved. Future work should therefore include testing with alternative LCR measurement configurations, improved shielding, and an extended frequency and temperature range to more reliably capture dielectric behavior in conductive regimes.

Scalability must be evaluated. Printing with smaller nozzle diameters (0.2 mm or below) would allow finer electrodes, thinner dielectric separations, and increased device resolution. This would test whether the sensor's performance improves or whether higher resolution introduces new limitations such as clogging, shear-induced MWCNT damage, or greater variability.

References

[1] P. F. Flowers, C. Reyes, S. Ye, M. J. Kim, and B. J. Wiley, "3D printing electronic components and circuits with conductive thermoplastic filament," *Addit Manuf*, vol. 18, pp. 156–163, Dec. 2017, doi: 10.1016/j.addma.2017.10.002.

[2] M. Kim *et al.*, "Electrically Conducting and Mechanically Strong Graphene–Polylactic Acid Composites for 3D Printing," *ACS Appl Mater Interfaces*, vol. 11, no. 12, pp. 11841–11848, Mar. 2019, doi: 10.1021/acsami.9b03241.

[3] M. Misiak *et al.*, "Electrically conductive and flexible filaments of hot melt adhesive for the fused filament fabrication process," *Physics of Fluids*, vol. 36, no. 3, Mar. 2024, doi: 10.1063/5.0195103.

[4] R. Wei, H. Li, Z. Chen, Q. Hua, G. Shen, and K. Jiang, "Revolutionizing wearable technology: advanced fabrication techniques for body-conformable electronics," *npj Flexible Electronics*, vol. 8, no. 1, p. 83, Dec. 2024, doi: 10.1038/s41528-024-00370-8.

[5] N. Yadav, Q. Zhang, D. Qi, A. Yadav, and H. Zheng, "AI-integrated wearable strain sensors: advances in e-skin, robotics, and personalized health monitoring," *Nanoscale Adv*, vol. 7, no. 16, pp. 4803–4819, 2025, doi: 10.1039/D5NA00574D.

[6] H. Souri *et al.*, "Wearable and Stretchable Strain Sensors: Materials, Sensing Mechanisms, and Applications," *Advanced Intelligent Systems*, vol. 2, no. 8, Aug. 2020, doi: 10.1002/aisy.202000039.

[7] Y. Liu, H. Wang, W. Zhao, M. Zhang, H. Qin, and Y. Xie, "Flexible, Stretchable Sensors for Wearable Health Monitoring: Sensing Mechanisms, Materials, Fabrication Strategies and Features," *Sensors*, vol. 18, no. 2, p. 645, Feb. 2018, doi: 10.3390/s18020645.

[8] X. Zhang, J. Chai, Y. Zhan, D. Cui, X. Wang, and L. Gao, "Design, Fabrication, and Application of Large-Area Flexible Pressure and Strain Sensor Arrays: A Review," *Micromachines (Basel)*, vol. 16, no. 3, p. 330, Mar. 2025, doi: 10.3390/mi16030330.

[9] M. J. Hossain, B. T. Tabatabaei, M. Kiki, and J.-W. Choi, "Additive Manufacturing of Sensors: A Comprehensive Review," *International Journal of Precision Engineering and Manufacturing-Green Technology*, vol. 12, no. 1, pp. 277–300, Jan. 2025, doi: 10.1007/s40684-024-00629-5.

[10] M. S. Hassan *et al.*, "3D Printed Integrated Sensors: From Fabrication to Applications—A Review," *Nanomaterials*, vol. 13, no. 24, p. 3148, Dec. 2023, doi: 10.3390/nano13243148.

[11] F. Huang, J. Hu, and X. Yan, "Review of Fiber- or Yarn-Based Wearable Resistive Strain Sensors: Structural Design, Fabrication Technologies and Applications," *Textiles*, vol. 2, no. 1, pp. 81–111, Feb. 2022, doi: 10.3390/textiles2010005.

[12] J. Chen *et al.*, "Polydimethylsiloxane (PDMS)-Based Flexible Resistive Strain Sensors for Wearable Applications," *Applied Sciences*, vol. 8, no. 3, p. 345, Feb. 2018, doi: 10.3390/app8030345.

[13] M. Amjadi, K. Kyung, I. Park, and M. Sitti, "Stretchable, Skin-Mountable, and Wearable Strain Sensors and Their Potential Applications: A Review," *Adv Funct Mater*, vol. 26, no. 11, pp. 1678–1698, Mar. 2016, doi: 10.1002/adfm.201504755.

[14] H. Souri *et al.*, "Wearable and Stretchable Strain Sensors: Materials, Sensing Mechanisms, and Applications," *Advanced Intelligent Systems*, vol. 2, no. 8, Aug. 2020, doi: 10.1002/aisy.202000039.

[15] D. Cafiso, S. Lantean, C. F. Pirri, and L. Beccai, “Soft Mechanosensing via 3D Printing: A review,” *Advanced Intelligent Systems*, vol. 5, no. 6, Jun. 2023, doi: 10.1002/aisy.202200373.
[16] S. S. Crump, “Apparatus and method for creating three-dimensional objects,” U.S. Patent No. 5,121,329, 1992
[17] R. Jones *et al.*, “RepRap – the replicating rapid prototyper,” *Robotica*, vol. 29, no. 1, pp. 177–191, Jan. 2011, doi: 10.1017/S026357471000069X.
[18] T. D. Ngo, A. Kashani, G. Imbalzano, K. T. Q. Nguyen, and D. Hui, “Additive manufacturing (3D printing): A review of materials, methods, applications and challenges,” *Compos B Eng*, vol. 143, pp. 172–196, Jun. 2018, doi: 10.1016/j.compositesb.2018.02.012.
[19] S. C. Daminabo, S. Goel, S. A. Grammatikos, H. Y. Nezhad, and V. K. Thakur, “Fused deposition modeling-based additive manufacturing (3D printing): techniques for polymer material systems,” *Mater Today Chem*, vol. 16, p. 100248, Jun. 2020, doi: 10.1016/j.mtchem.2020.100248.
[20] I. Gibson, D. Rosen, and B. Stucker, *Additive Manufacturing Technologies*. New York, NY: Springer New York, 2015. doi: 10.1007/978-1-4939-2113-3.
[21] A. C. de Leon, Q. Chen, N. B. Palaganas, J. O. Palaganas, J. Manapat, and R. C. Advincula, “High performance polymer nanocomposites for additive manufacturing applications,” *React Funct Polym*, vol. 103, pp. 141–155, Jun. 2016, doi: 10.1016/j.reactfunctpolym.2016.04.010.
[22] Z. Guo *et al.*, “Printed and Flexible Capacitive Pressure Sensor with Carbon Nanotubes based Composite Dielectric Layer,” *Micromachines (Basel)*, vol. 10, no. 11, p. 715, Oct. 2019, doi: 10.3390/mi10110715.
[23] P. Zhang, C. Guo, L. Huang, Y. Li, K. Zhang, and Y. Zhang, “Highly Stretchable Serpentine-Shaped Strain Sensor Based on 3-D Printing for Gestures Recognition,” *IEEE Trans Instrum Meas*, vol. 73, pp. 1–7, 2024, doi: 10.1109/TIM.2024.3488139.
[24] W. Yan, X. Tian, D. Zhang, Y. Zhou, and Q. Wang, “3D Printing of Stretchable Strain Sensor Based on Continuous Fiber Reinforced Auxetic Structure,” *Chinese Journal of Mechanical Engineering: Additive Manufacturing Frontiers*, vol. 2, no. 2, p. 100073, Jun. 2023, doi: 10.1016/j.cjmeam.2023.100073.
[25] J. T. B. Overvelde *et al.*, “A three-dimensional actuated origami-inspired transformable metamaterial with multiple degrees of freedom,” *Nat Commun*, vol. 7, no. 1, p. 10929, Mar. 2016, doi: 10.1038/ncomms10929.
[26] J. Paulose, A. S. Meeussen, and V. Vitelli, “Selective buckling via states of self-stress in topological metamaterials,” *Proceedings of the National Academy of Sciences*, vol. 112, no. 25, pp. 7639–7644, Jun. 2015, doi: 10.1073/pnas.1502939112.
[27] A. Pentek *et al.*, “The Effect of Printing Parameters on Electrical Conductivity and Mechanical Properties of PLA and ABS Based Carbon Composites in Additive Manufacturing of Upper Limb Prosthetics,” *Crystals (Basel)*, vol. 10, no. 5, p. 398, May 2020, doi: 10.3390/cryst10050398.
[28] K. Dembek, B. Podsiadły, and M. Słoma, “Influence of Process Parameters on the Resistivity of 3D Printed Electrically Conductive Structures,” *Micromachines (Basel)*, vol. 13, no. 8, p. 1203, Jul. 2022, doi: 10.3390/mi13081203.

[29] A. Glogowsky, M. Korger, and M. Rabe, “Influence of print settings on conductivity of 3D printed elastomers with carbon-based fillers,” *Progress in Additive Manufacturing*, vol. 9, no. 4, pp. 791–803, Aug. 2024, doi: 10.1007/s40964-023-00483-y.
[30] S. K. Lee, Y. R. Kim, T. J. Yoo, J. H. Park, and J. H. Kim, “Study on Electrical Characteristics of FDM Conductive 3D Printing According to Annealing Conditions,” *Journal of the Korean Society of Manufacturing Process Engineers*, vol. 17, no. 6, pp. 53–60, Dec. 2018, doi: 10.14775/ksmpe.2018.17.6.053.
[31] C. Iffelsberger, C. W. Jellett, and M. Pumera, “3D Printing Temperature Tailors Electrical and Electrochemical Properties through Changing Inner Distribution of Graphite/Polymer,” *Small*, vol. 17, no. 24, Jun. 2021, doi: 10.1002/smll.202101233.
[32] R. Paz, R. Moriche, M. Monzón, and J. García, “Influence of Manufacturing Parameters and Post Processing on the Electrical Conductivity of Extrusion-Based 3D Printed Nanocomposite Parts,” *Polymers (Basel)*, vol. 12, no. 4, p. 733, Mar. 2020, doi: 10.3390/polym12040733.
[33] T. Ma *et al.*, “Advances in 3D printing for polymer composites: A review,” *InfoMat*, vol. 6, no. 6, Jun. 2024, doi: 10.1002/inf2.12568.
[34] Q. Zhang, Y. Xu, Y. Yang, L. Li, C. Song, and X. Su, “Conductive mechanism of carbon black/polyimide composite films,” *Journal of Polymer Engineering*, vol. 38, no. 2, pp. 147–156, Feb. 2018, doi: 10.1515/polyeng-2016-0273.
[35] K. Yang, M. Gu, Y. Guo, X. Pan, and G. Mu, “Effects of carbon nanotube functionalization on the mechanical and thermal properties of epoxy composites,” *Carbon N Y*, vol. 47, no. 7, pp. 1723–1737, Jun. 2009, doi: 10.1016/j.carbon.2009.02.029.
[36] W. Bauhofer and J. Z. Kovacs, “A review and analysis of electrical percolation in carbon nanotube polymer composites,” *Compos Sci Technol*, vol. 69, no. 10, pp. 1486–1498, Aug. 2009, doi: 10.1016/j.compscitech.2008.06.018.
[37] A. Nogales *et al.*, “Low Percolation Threshold in Nanocomposites Based on Oxidized Single Wall Carbon Nanotubes and Poly(butylene terephthalate),” *Macromolecules*, vol. 37, no. 20, pp. 7669–7672, Oct. 2004, doi: 10.1021/ma049440r.
[38] Z. Ali, S. Yaqoob, J. Yu, and A. D’Amore, “Critical review on the characterization, preparation, and enhanced mechanical, thermal, and electrical properties of carbon nanotubes and their hybrid filler polymer composites for various applications,” *Composites Part C: Open Access*, vol. 13, p. 100434, Mar. 2024, doi: 10.1016/j.jcomc.2024.100434.
[39] J. Chen, B. Liu, X. Gao, and D. Xu, “A review of the interfacial characteristics of polymer nanocomposites containing carbon nanotubes,” *RSC Adv*, vol. 8, no. 49, pp. 28048–28085, 2018, doi: 10.1039/C8RA04205E.
[40] A. A. Balandin, “Thermal properties of graphene and nanostructured carbon materials,” *Nat Mater*, vol. 10, no. 8, pp. 569–581, Aug. 2011, doi: 10.1038/nmat3064.
[41] X. Li, D. Niu, P. Xu, W. Yang, and P. Ma, “High-toughness and antistatic PET/EMAG/CNTs nanocomposites from recycled sources by reactive compatibilization,” *Composites Communications*, vol. 47, p. 101855, Apr. 2024, doi: 10.1016/j.coco.2024.101855.
[42] J. Chen, X. Cui, K. Sui, Y. Zhu, and W. Jiang, “Balance the electrical properties and mechanical properties of carbon black filled immiscible polymer blends with a double percolation structure,” *Compos Sci Technol*, vol. 140, pp. 99–105, Mar. 2017, doi: 10.1016/j.compscitech.2016.12.029.

[43] C. Gao, S. Zhang, Y. Lin, F. Li, S. Guan, and Z. Jiang, “High-performance conductive materials based on the selective location of carbon black in poly(ether ether ketone)/polyimide matrix,” *Compos B Eng*, vol. 79, pp. 124–131, Sep. 2015, doi: 10.1016/j.compositesb.2015.03.047.
[44] S. Iijima, “Helical microtubules of graphitic carbon,” *Nature*, vol. 354, no. 6348, pp. 56–58, Nov. 1991, doi: 10.1038/354056a0.
[45] S. Lage-Rivera, A. Ares-Pernas, J. C. Becerra Permuy, A. Gosset, and M.-J. Abad, “Enhancement of 3D Printability by FDM and Electrical Conductivity of PLA/MWCNT Filaments Using Lignin as Bio-Dispersant,” *Polymers (Basel)*, vol. 15, no. 4, p. 999, Feb. 2023, doi: 10.3390/polym15040999.
[46] T. Kajornprai, R. Jarapanyacheep, J. Saikaeo, S. Pojprapai, K. Jarukumjorn, and T. Trongsatitkul, “Double Percolation of Poly(lactic acid)/Low-Density Polyethylene/Carbon Nanotube (PLA/LDPE/CNT) Composites for Force-Sensor Application: Impact of Preferential Localization and Mixing Sequence,” *Polymers (Basel)*, vol. 16, no. 13, p. 1906, Jul. 2024, doi: 10.3390/polym16131906.
[47] A. Motaghi, A. Hrymak, and G. H. Motlagh, “Electrical conductivity and percolation threshold of hybrid carbon/polymer composites,” *J Appl Polym Sci*, vol. 132, no. 13, Apr. 2015, doi: 10.1002/app.41744.
[48] M. Spoerk *et al.*, “Anisotropic properties of oriented short carbon fibre filled polypropylene parts fabricated by extrusion-based additive manufacturing,” *Compos Part A Appl Sci Manuf*, vol. 113, pp. 95–104, Oct. 2018, doi: 10.1016/j.compositesa.2018.06.018.
[49] X. Nan *et al.*, “A Review of the Establishment of Effective Conductive Pathways of Conductive Polymer Composites and Advances in Electromagnetic Shielding,” *Polymers (Basel)*, vol. 16, no. 17, p. 2539, Sep. 2024, doi: 10.3390/polym16172539.
[50] D. A. Gök and B. D. Akay, “Fabrication and characterization of carbon and glass fiber reinforced thermoplastic composites by fused filament fabrication,” *Sci Rep*, vol. 15, no. 1, p. 30037, Aug. 2025, doi: 10.1038/s41598-025-15450-6.
[51] M. Al-Rubaiai, R. Tsuruta, U. Gandhi, C. Wang, and X. Tan, “A 3D-printed stretchable strain sensor for wind sensing,” *Smart Mater Struct*, vol. 28, no. 8, p. 084001, Aug. 2019, doi: 10.1088/1361-665X/ab1fa9.
[52] M. Arh and J. Slavič, “Single-Process 3D-Printed Triaxial Accelerometer,” *Adv Mater Technol*, vol. 7, no. 7, Jul. 2022, doi: 10.1002/admt.202101321.
[53] M. Schouten, R. Sanders, and G. Krijnen, “3D printed flexible capacitive force sensor with a simple micro-controller based readout,” in *2017 IEEE SENSORS*, IEEE, Oct. 2017, pp. 1–3. doi: 10.1109/ICSENS.2017.8233949.
[54] X. Aeby, R. van Dommelen, and D. Briand, “Fully FDM 3D Printed Flexible Capacitive and Resistive Transducers,” in *2019 20th International Conference on Solid-State Sensors, Actuators and Microsystems & Eurosensors XXXIII (TRANSDUCERS & EUROSENSORS XXXIII)*, IEEE, Jun. 2019, pp. 2440–2443. doi: 10.1109/TRANSDUCERS.2019.8808268.
[55] C. El Helou, P. R. Buskohl, C. E. Tabor, and R. L. Harne, “Digital logic gates in soft, conductive mechanical metamaterials,” *Nat Commun*, vol. 12, no. 1, p. 1633, Mar. 2021, doi: 10.1038/s41467-021-21920-y.

[56] G. Wolterink, R. Sanders, and G. Krijnen, “Thin, Flexible, Capacitive Force Sensors Based on Anisotropy in 3D-Printed Structures,” in *2018 IEEE SENSORS*, IEEE, Oct. 2018, pp. 1–4. doi: 10.1109/ICSENS.2018.8589584.
[57] M. O. F. Emon, F. Alkadi, D. G. Philip, D.-H. Kim, K.-C. Lee, and J.-W. Choi, “Multi-material 3D printing of a soft pressure sensor,” *Addit Manuf*, vol. 28, pp. 629–638, Aug. 2019, doi: 10.1016/j.addma.2019.06.001.
[58] Richard Boyd, “Dielectric relaxation,” in *Polymer Dynamics and Relaxation*, Cambridge University Press, 2007, pp. 27–43. doi: 10.1017/CBO9780511600319.004.
[59] A. Schönhals and F. Kremer, *Broadband Dielectric Spectroscopy*. Berlin, Heidelberg: Springer Berlin Heidelberg, 2003. doi: 10.1007/978-3-642-56120-7.
[60] S. Havriliak and S. Negami, “A complex plane representation of dielectric and mechanical relaxation processes in some polymers,” *Polymer (Guildf)*, vol. 8, pp. 161–210, Jan. 1967, doi: 10.1016/0032-3861(67)90021-3.
[61] I. A. Ventura, J. Zhou, and G. Lubineau, “Investigating the Inter-Tube Conduction Mechanism in Polycarbonate Nanocomposites Prepared with Conductive Polymer-Coated Carbon Nanotubes,” *Nanoscale Res Lett*, vol. 10, no. 1, p. 485, Dec. 2015, doi: 10.1186/s11671-015-1191-x.
[62] Y. Zare and K. Y. Rhee, “Simulation of Percolation Threshold, Tunneling Distance, and Conductivity for Carbon Nanotube (CNT)-Reinforced Nanocomposites Assuming Effective CNT Concentration,” *Polymers (Basel)*, vol. 12, no. 1, p. 114, Jan. 2020, doi: 10.3390/polym12010114.
[63] B. J.-P. Adohi, C. V. Bouanga, K. Fatyeyeva, and M. Tabellout, “Application of the Maxwell–Wagner–Hanai effective medium theory to the analysis of the interfacial polarization relaxations in conducting composite films,” *J Phys D Appl Phys*, vol. 42, no. 1, p. 015302, Jan. 2009, doi: 10.1088/0022-3727/42/1/015302.
[64] J.-P. Peng, H. Zhang, L.-C. Tang, Y. Jia, and Z. Zhang, “Dielectric Properties of Carbon Nanotubes/Epoxy Composites,” *J Nanosci Nanotechnol*, vol. 13, no. 2, pp. 964–969, Feb. 2013, doi: 10.1166/jnn.2013.6041.
[65] N. Yousefi *et al.*, “Highly Aligned Graphene/Polymer Nanocomposites with Excellent Dielectric Properties for High-Performance Electromagnetic Interference Shielding,” *Advanced Materials*, vol. 26, no. 31, pp. 5480–5487, Aug. 2014, doi: 10.1002/adma.201305293.
[66] R. Belhimria *et al.*, “Thermal and dielectric properties of carbon nanotubes/graphite/polyester ternary composites,” *J Compos Mater*, vol. 55, no. 25, pp. 3741–3750, Oct. 2021, doi: 10.1177/00219983211021886.
[67] J. Belattar, M. P. F. Graça, L. C. Costa, M. E. Achour, and C. Brosseau, “Electric modulus-based analysis of the dielectric relaxation in carbon black loaded polymer composites,” *J Appl Phys*, vol. 107, no. 12, Jun. 2010, doi: 10.1063/1.3452366.
[68] D. Strugova *et al.*, “Evolution of morphology and electrical properties under controlled flow in polypropylene/polystyrene co-continuous blends containing interfacially localized carbonaceous nanoparticles,” *Physics of Fluids*, vol. 36, no. 11, Nov. 2024, doi: 10.1063/5.0240789.
[69] Z. Samir, S. Boukheir, Y. El Merabet, M. P. F. Graça, M. E. Achour, and L. C. Costa, “Temperature Effect on the Dielectric Response of Carbon Nanotubes Particles Filled Polyester Polymer Composites,” in Advanced Nanotechnologies for Detection and

Defence against CBRN Agents, Springer, 2018, pp. 261–272. doi: 10.1007/978-94-024-1298-7_25.
[70] Q. Li, Q. Z. Xue, X. L. Gao, and Q. B. Zheng, “Temperature dependence of the electrical properties of the carbon nanotube/polymer composites,” *Express Polym Lett*, vol. 3, no. 12, pp. 769–777, 2009, doi: 10.3144/expresspolymlett.2009.95.
[71] J. Gong, O. Seow, C. Honnet, J. Forman, and S. Mueller, “MetaSense: Integrating Sensing Capabilities into Mechanical Metamaterial,” in *The 34th Annual ACM Symposium on User Interface Software and Technology*, New York, NY, USA: ACM, Oct. 2021, pp. 1063–1073. doi: 10.1145/3472749.3474806.